Faculteit Wetenschappen
Departement Fysica
Experimentele Fysica van de
Gecondenseerde Materie

Charge recombination in novel blend materials for organic solar cells: optical detection and kinetic modelling

Melissa Van Landeghem

Academiejaar 2014-2015

Promotor:
Prof. Dr. Etienne Goovaerts

Proefschrift ter verkrijging van de graad van Master in de Fysica.

Dankwoord

In de eerste plaats wil ik graag mijn promotor Etienne Goovaerts bedanken. Zowel voor het aanreiken van een onderwerp dat zo nauw aansluit bij mijn interesses, als voor zijn onuitputtelijke enthousiasme tijdens de begeleiding van mijn thesis. Ik wil hem ook hartelijk bedanken voor zijn hulp bij de interpretatie van de data en het schrijven van de tekst. Daarnaast wil ik ook Biniam Zerai Tedlla bedanken voor de begeleiding tijdens het maken van samples. Omdat een thesis in de experimentele fysica nu eenmaal gepaard gaat met de nodige technische problemen, ook een gemeend woord van dank voor Paul, Ivan en Ivo van de technische ploeg voor alle hulp tijdens mijn metingen. Ook de andere mensen van de ECM en SIBAC groep wil ik graag bedanken voor hun steun en aanmoedigingen. Zij hebben mij in elk geval goed geholpen om de kleine tegenslagen van het experimenteel onderzoek te relativeren. Ten slotte wil ik nog de mensen bedanken die de materialen hebben ontwikkeld waar ik mijn thesisonderzoek op kon doen: prof. dr. Wouter Maes, Julija Kudrjasova en Jurgen Kesters van de groep Design and synthesis of organic semiconductors (DSOS) van het instituut voor materiaalonderzoek (IMO) van de UHasselt.
Via deze weg wil ik ook graag mijn ouders en grootouders bedanken die mij altijd gestimuleerd hebben om fysica te gaan studeren en die mij alle kansen hebben gegeven om mijn studie af te maken. Verder wil ik hen bedanken voor hun oprechte interesse in mijn thesis ook al is die voor hen moeilijk te begrijpen. In het bijzonder wil ik mijn vriend Sigiswald bedanken voor alle hulp en steun de voorbije twee jaar en omdat hij mij altijd opnieuw goede moed heeft gegeven.

Contents

Preface

The discovery of conducting polymers in the late '70s gave rise to the development of a new type of solar cells based on organic semiconductors. Although power conversion efficiencies are still much lower than for their inorganic counterparts, organic photovoltaic (OPV) systems are considered promising low-cost alternatives for the current mainly crystalline silicon based solar cells. Moreover, as organic solar cells (OSCs) can be manufactured by low temperature processes such as coating or roll-to-roll printing, they are compatible with flexible plastic substrates leading to novel 'plastic electronics' applications. Taking into account the rapid growth of power conversion efficiencies of OSCs over the last few years, OPV certainly has the potential of becoming an economically viable sustainable energy resource in the future. A lot of research is still going on to gain a more fundamental understanding of the physical processes taking place in organic solar cells. Based on these findings, new organic materials can be designed to improve the solar cell efficiencies.

This thesis contributes to the research on novel solar cell materials with a study of recently synthesised 2,5-dithienylthiazolo[5,4-d]thiazole (DTTzTz) molecules. The molecules are designed for use in bulk-heterojunction organic solar cells which is the most successful device architecture for OSCs up to now. The active layer of such devices consists of an interpenetrating network of two different organic semiconductors, one that serves as electron donor and the other as electron acceptor. An important step in the photovoltaic process of this type of devices is the charge transfer between donor and acceptor when the device is illuminated. In this thesis, the photo-induced charge transfer in different blends with the novel DTTzTz materials is optically characterised by means of absorption, photoluminescence and photo-induced absorption (PIA) spectroscopy on spin-coated films. Of particular interest was the modelling of time-dependent PIA measurements in order to determine the physical mechanisms governing the generation and recombination kinetics of charge carriers in the blends.

The outline of this thesis is organised as follows. The first two chapters provide a theoretical introduction to the field of organic solar cells. The sample preparation methods and experimental techniques used to characterise the new OSC materials are discussed in chapter 3. Chapter 4 treats the mathematical formulation and the underlying physical mechanisms of the two models used to fit the time-dependent PIA measurements. The experimental results are presented and discussed in chapter 5 and 6. Finally, in the last chapter we briefly summarise the main results and conclusions of this thesis and provide an outlook for future research on the DTTzTz materials.

Melissa Van Landeghem, January 2015

Abbreviations

OSC Organic solar cell

OPV Organic photovoltaics

OLED Organic light-emitting diode

OFET Organic field-effect transistor

BHJ Bulk heterojunction

HOMO Highest occupied molecular orbital

LUMO Lowest unoccupied molecular orbital

D/A interface Donor acceptor interface

CT Charge transfer

PCE Power conversion efficiency

$\mathbf{V}_{oc}$ Open circuit voltage

$\mathbf{J}_{sc}$ Short circuit current

FF Fill factor

ISC Intersystem crossing

ITO Indium tin oxide

PEDOT:PSS Poly(styrenesulfonate) doped poly(3,4-ethylenedioxythiophene)

MDMO-PPV Poly[2-methoxy-5-(3,7-dimethyloctyloxy)-1,4-phenylenevinylene]

P3HT Poly(3-hexylthiophene-2,5-diyl)

DTTzTz 2,5-dithienylthiazolo[5,4-d]thiazole

TPA triphenylamine

CN benzonitrile

diCN benzodinitrile

PC70BM Phenyl-C_{71}-butyric acid methyl ester

UV Ultraviolet light

VIS Visible light

NIR Near infra-red light

PMT Photomultiplier

CCD Charge-coupled device

PL Photoluminescence

PIA Photo-induced absorption

TR-PIA Time-resolved photo-induced absorption

CW-PIA Continuous-wave photo-induced absorption

LWP Long wavelength pass

AC Alternating current

DC Direct current

Chapter 1

Introduction

The development of economically viable sustainable energy resources is one of the greatest technological challenges of this century. At present, the global energy supply is still dominated by fossil fuels such as coal, oil and natural gas. Yet, during the last decades, the awareness of the finite reserves of fossil resources has motivated the search for renewable energy sources. Also the large amount of greenhouse gasses released during the combustion of fossil fuels forms an obstacle in the worldwide ambition to reduce carbon dioxide emissions and to mitigate global warming. In this context, solar energy is without exception considered as one of the most promising alternatives for the conventional energy resources.
Solar energy can be harnessed by means of photovoltaic (PV) systems that convert sunlight into electricity. Over the past five years, the PV market has continued to expand at a rapid rate, with growth in global capacity averaging almost 55% annually [13]. Yet, the contribution of solar cell technology to the total global energy supply still remains below 0.7% mainly because the generation cost of PV electricity is not yet competitive with the prices of electricity generated from conventional sources. Hence, despite the substantial efficiency improvements and decrease in production cost of the last years, the current solar cell technology dominated by crystalline silicon modules still seems too expensive to compete with electricity from fossil fuels or nuclear power plants without governmental support. Therefore strong research efforts have been going on to reduce the solar cell production costs by developing new technologies or novel materials for photovoltaics. This paved the way for a new generation of solar cells based on organic materials. Despite their typically lower power conversion efficiencies, the possible low-cost and ease of processing of organic devices makes them promising as a cheap alternative to the current, mainly crystalline silicon based, inorganic semiconductor industry.
The emerging field of organic photovoltaics (OPV) is the subject of this thesis. In this introductory chapter, we will present a brief comparison between organic and inorganic solar cells and an overview of the current status of OPV. An outline of the thesis is given in the last section.

1.1 Organic versus inorganic photovoltaics

In spite of the significantly lower device efficiencies, organic photovoltaic systems offer some interesting advantages over their inorganic counterparts. First of all, many organic semiconductors exhibit very high absorption coefficients such that an active layer thickness of $100-200\,\mathrm{nm}$ is sufficient for most OSC devices. This is roughly three orders of magnitude less than the active layer thickness required in conventional silicon solar cells. Hence material costs are greatly reduced in OPV systems. Moreover, most technologically important organic semiconductors are processed by thermal evaporation or spin coating from solution which are low-temperature techniques that are compatible with flexible substrates such as plastics. The possibility of producing light-weight flexible solar cells could lead to a whole new range of photovoltaic

applications such as built-in devices or even wearable PV. Furthermore, in the future state-of-the-art printing tools could allow roll-to-roll processing of OSCs in large volumes resulting in significantly lower manufacturing costs as compared to crystalline silicon solar cells that usually require high-temperature processing steps exceeding 1000 °C. Apart from the reduction of production costs, OSCs would therefore also have much shorter energy payback times and a lower environmental impact during manufacturing as compared to conventional inorganic photovoltaics. Hence we conclude that the ease of processing and the high potential of OPV as a cheap and environmentally friendly technology could ultimately compensate for the lower solar cell efficiencies.

1.2 Present status of organic photovoltaics

Over the last ten years, the power conversion efficiencies (PCEs) of organic solar cells have increased substantially as shown in figure 1.1. Today, record efficiencies of about 10% are reported for the best performing OPV systems. Yet, these efficiencies are obtained for laboratory solar cell samples and efficiencies for commercial PV systems would be much lower. According to Scharber and Sariciftci [14] the first prototypes for commercially available modules exhibit power conversion efficiencies in the range of 1.5-2.5% which are very low in comparison with the 18-20% efficiencies obtained for commercial mono-crystalline silicon solar panels. Hence further efficiency improvements are indispensable before organic solar cells can enter the PV market in direct competition with conventional inorganic technologies. Due to the great flexibility of organic chemistry, a common approach to improve power conversion efficiencies is the design and synthesis of novel solar cell materials.

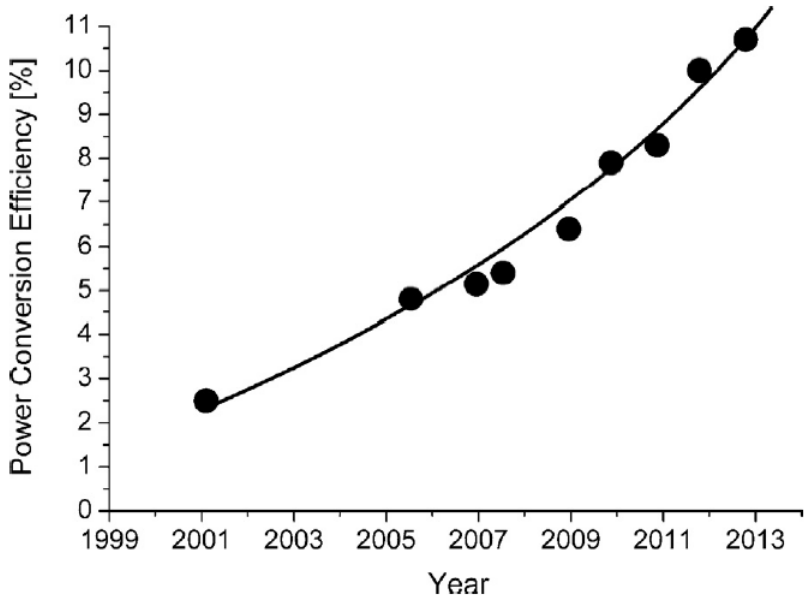

Figure 1.1: Certified record power conversion efficiencies of single junction organic solar cells published in Progress in Photovoltaics. Figure taken from [14].

Another limitation of organic solar cells at the moment is the poor long-term stability under ambient conditions. Hence, the improvement of solar cell durability either via the design of new organic semiconductors with improved photochemical stability or by rigorous encapsulation of the devices is an additional prerequisite for large scale commercialisation of OSCs. Therefore a major part of the research in organic photovoltaics involves the development of new materials to improve both solar cell efficiencies and device stability. Yet, the remarkable progress in the field of OSCs of the last years has been accompanied by a trend for more expensive materials.

Hence also the development of low-cost alternatives for some of the current solar cell materials is an important topic in OPV research.

1.3 Outline of this thesis

This thesis contributes to the research on novel solar cell materials with a study of recently synthesised 2,5-dithienylthiazolo[5,4-d]thiazole (DTTzTz) molecules. **Chapter 2** provides a theoretical background to the physics behind organic solar cells and the working principle of the devices. The focus will be on bulk heterojunction solar cells with an active layer consisting of a blend of donor and acceptor materials because the novel molecules studied in this thesis were designed for use in such devices. The relevance of the experimental work done in this thesis will be motivated in the context of a number of challenges encountered in current OPV research.
In **chapter 3** we present the sample preparation methods and experimental techniques used to characterise the novel solar cell materials. All experimental work was performed on thin films prepared by spin coating from solution. The optical characterisation of the samples was done by means of UV-VIS absorption, photoluminescence (PL) and photo-induced absorption (PIA) spectroscopy. For all techniques, the experimental set-up and the application in the context of OPV research is discussed.
Time-resolved PIA measurements are particularly suited to study the dynamics of charge generation and recombination in blends for organic solar cells. By modelling the experimental data, the nature of the recombination processes can be studied yielding essential information on the solar cell performance. In **chapter 4** two models are introduced to describe the experimental PIA data: the monomolecular and bimolecular model. The mathematical formulation and the underlying physical mechanisms are discussed and an extension to both models is derived by including the effect of ground state depletion.
In **chapter 5** the results of our study of the novel donor molecule TPA-DTTzTz-diCN in combination with the standard acceptor material PC70BM are presented. Efficient charge transfer in this system is demonstrated by the quenching of donor PL and the clear PIA signal in the blend arising from excitations of positive polarons, i.e. charge carriers on the donor material. Yet, also the pristine TPA-DTTzTz-diCN exhibited a surprisingly large PIA signal that was attributed to triplet exciton states. Of particular interest was the modelling of the TR-PIA data to determine the physical mechanism governing the recombination kinetics of polarons and triplets.
In **chapter 6** two recently synthesised acceptor molecules CN-DTTzTz-CN and diCN-DTTzTz-diCN are studied in blends with the standard donor polymers MDMO-PPV and P3HT. Successful charge transfer between donor and acceptor is examined by means of PL quenching and PIA measurements to investigate charge carriers created upon photo-excitation of the samples.
Finally, **chapter 7** briefly summarises the results and conclusions of this thesis and presents an outlook for future research on the DTTzTz materials.

Chapter 2

Organic solar cells

Ever since the discovery of conducting polymers the field of organic electronics has attracted great scientific interest. Many applications of organic semiconductors have already been developed including organic photovoltaics (OPV), organic light-emitting diodes (OLEDs) and organic field-effect transistors (OFETs). This chapter presents an introduction to the physics behind organic solar cells and the working principle of the devices. First the origin of conductivity in organic semiconductors is discussed. In the following sections we describe how the conducting properties of organic materials can be exploited in solar cells. The focus will be on the most successful device architecture, i.e. the bulk heterojunction solar cell.

2.1 Conduction in conjugated polymers

Conduction in organic molecules and polymers arises from the presence of π-conjugation in carbon chains with alternating single and double bonds. In conjugated systems, three of the four $2s^2 2p^2$ valence electrons of carbon hybridize to form coplanar sp^2 orbitals leaving one additional p_z-orbital that is directed out-of-plane. Two sp^2 orbitals are used to form covalent bonds between neighbouring carbon atoms, the third binds to a hydrogen atom or side group. This way a planar structure of strongly localized σ-bonds is formed. The remaining p_z-orbitals of adjacent carbon atoms overlap and form π-bonds leading to a delocalization of the π-electrons along the molecule. It's this π-conjugation that gives rise to the molecule's conducting properties. Examples of such conjugated materials are polyacetylene, as shown in figure 2.1, and the benzene ring.

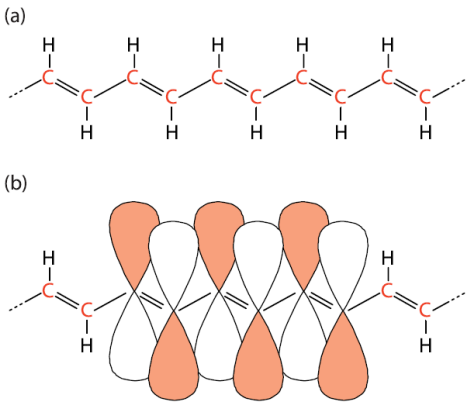

Figure 2.1: (a) Example of a conjugated polymer: part of a polyacetylene chain containing alternating single and double bonds. (b) π-bonds between overlapping p_z-orbitals. The adjacent orbitals are in an anti-bonding configuration which corresponds to the LUMO of the polymer. Figure taken from [15].

Assuming equal binding length between the contiguous carbon atoms, the delocalization of the π-electrons over the entire molecule would give rise to metallic behaviour. However, in the equilibrium configuration alternating shorter and longer C-C bonds are formed and the delocalization of the π-electrons is limited. As a result of this so-called Peierls distortion, a band gap of a few eV opens up between the highest occupied molecular orbital (HOMO) and the lowest unoccupied molecular orbital (LUMO). Hence conjugated polymers exhibit semiconductor behaviour wherein the bonding π-orbitals and the anti-bonding π^*-orbitals function respectively as analogues of the valence and conduction band in inorganic semiconductors.

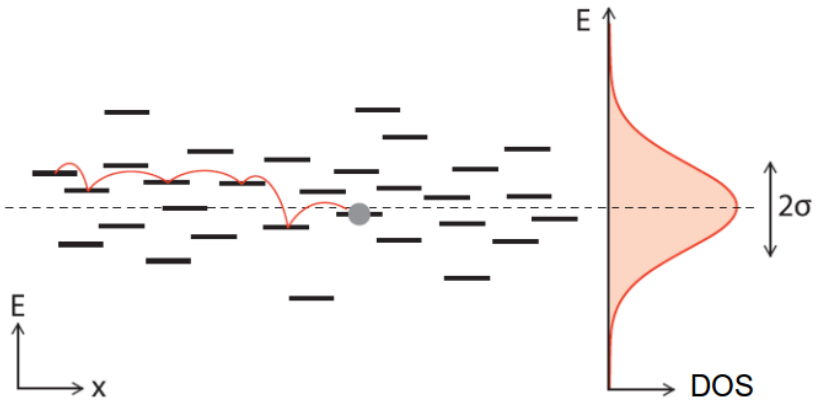

Figure 2.2: Schematic representation of translational and energetic disorder in organic semiconductors. The hopping of a charge carrier between localized sites is illustrated. The density of states (DOS) is assumed to be Gaussian. Figure adapted from [15].

Most technologically important organic semiconductors are solution-processed polymers and thermally evaporated small molecules. The resulting layers are polycrystalline or amorphous and no long-range order exists between the molecules. Therefore the charge carriers become localized on single molecules or parts of the polymer chain. Since the local energy levels are determined by the local structure, this translational disorder results in an energetic disorder which is often approximated by a Gaussian density of states. Charge transport throughout the organic layer is hence different from band conduction in inorganic semiconductors and occurs via phonon assisted tunnelling between nearby localized sites. Charges in organic semiconductors are described as polarons consisting of the bare charge carrier surrounded by a cloud of phonons representing the lattice deformation accompanying the carrier. The energy difference between neighbouring sites can then be overcome by emitting or absorbing a phonon. Figure 2.2 illustrates the hopping of a charge carrier in the disordered organic semiconductor. Because of this hopping transport mechanism mobilities in organic semiconductors are typically several orders of magnitude lower than in inorganic semiconductors.

2.2 Device design strategies for organic solar cells

Electronic applications require the injection or extraction of charges from the organic layer. This can be accomplished by sandwiching the active material(s) between metal electrodes of different work functions. The effective electric field arising from this difference in work function will then provide the driving force for charge transport throughout the organic layer when the device is illuminated. However, different types of device designs exist depending on the composition of the organic layer. In this section the historical development of organic solar cell devices is presented. Of particular interest are the problems encountered in early solar cell designs that lead to the development of today's bulk heterojunction OSCs.

2.2.1 Single-layer organic solar cells

The first attempts to make organic solar cells were based on single-layer devices containing only one active organic semiconductor. When the device is exposed to light, the organic material can absorb photons with an energy large enough to promote an electron from the HOMO to the LUMO. The excited electron and the remaining positively charged hole in the HOMO then form a Coulombically bound pair or exciton. When the binding energy of the exciton can be overcome, the charge carriers are separated and will drift towards their respective electrodes due to the built-in electric field. The charges extracted at the cathode and anode then give rise to the desired photocurrent. The power conversion efficiencies of these single-layer OSCs remained however far below 1% for the solar spectrum. The reason is that in organic semiconductors the dielectric constant is much lower as compared to their inorganic counterparts resulting in higher exciton binding energies $\sim 0.35 - 0.5\,\mathrm{eV}$ [14]. Hence, in normal operating conditions the exciton binding energy will exceed the thermal energy $k_B T$ by an order of magnitude and thermal excitations will not suffice to dissociate the excitons. As a consequence, an additional driving force will be required to break up the photogenerated excitons and to improve the power conversion efficiency of the solar cell.

2.2.2 Bilayer organic solar cells

To address the problem of the high exciton binding energy, a new type of organic solar cells was developed in the mid '80s [3]. In bilayer OSCs a second organic semiconductor layer was introduced which will act as an acceptor for the excited electrons. For most of the studied bilayer systems the absorption of photons mainly takes place in the so-called donor material. The created excitons then diffuse within the donor material towards the planar donor/acceptor (D/A) interface. There the difference in electronegativity between donor and acceptor will provide the driving force for dissociation of the excitons and the excited electron will be transferred to the acceptor LUMO. The energy level diagram of such a donor-acceptor system is shown in figure 2.3. Note that also the opposite process can occur, i.e. excitons created in the acceptor material can be separated at the D/A interface via hole transfer from the acceptor to the donor. Yet, the most widely used acceptor materials are fullerene derivatives which show poor light absorption of the solar spectrum. As such their contribution to the total number of photogenerated excitons will be very low.

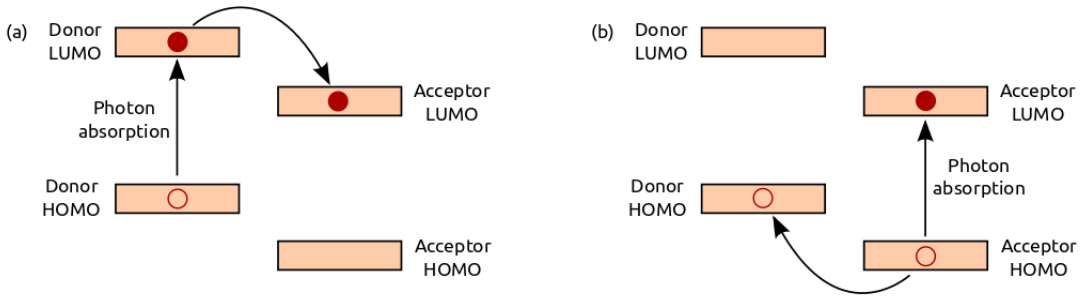

Figure 2.3: Energy level diagram of a donor-acceptor system. (a) Photon absorption in the donor followed by exciton dissociation via electron transfer from donor to acceptor at the D/A interface. (b) Photon absorption in the acceptor followed by exciton dissociation via hole transfer from acceptor to donor at the D/A interface.

The electron transfer from donor to acceptor was observed to be very fast and efficient in certain polymer-fullerene systems. Still the power conversion efficiency of bilayer OSCs did not exceed 1%. The problem with this bilayer approach is that for sufficient absorption of the incident light the thickness of the absorbing layer has to be of the order of 100 nm. This thickness largely exceeds the exciton diffusion length which is about $1 - 10\,\mathrm{nm}$ in typical donor

polymers. Hence only a small fraction of the photogenerated excitons will be able to reach the D/A interface where they can dissociate in free charge carriers that can contribute to the photocurrent. This limitation was resolved by a new concept for OSC design introduced in the early '90s: the bulk heterojunction (BHJ).

2.2.3 Bulk heterojunction organic solar cells

The active layer of a BHJ OSC consists of a blend of donor and acceptor materials. Both components form an interpenetrating network such that D/A interfaces expand throughout the entire active layer. An ideal BHJ morphology is obtained when the length scale of the phase separation is of the order of the exciton diffusion length. Hence all excitons created in the donor will be able to reach a D/A interface resulting in much larger photocurrents than could be obtained within the bilayer concept. However, due to the increased disorder and the random distribution of donor and acceptor regions, charge transport towards the electrodes can become severely hindered. For example, charge carriers can become trapped inside donor or acceptor islands where they can recombine with oppositely charged carriers thereby reducing the photocurrent. Therefore, in contrast to exciton dissociation, charge transport will be optimal in a bilayer design. Hence a trade-off exists between the phase separation length scale required for optimal exciton dissociation and the size of percolation paths for charge transport. As a result the morphology of the BHJ is of crucial importance for good device performance. Figure 2.4 (a) shows a proposal for an ideal BHJ morphology with the length scale of the phase separation equal to the exciton diffusion length L_{diff}. However, in realistic devices other considerations such as an optimal electric field distribution could lead to slightly different ideal BHJ morphologies.

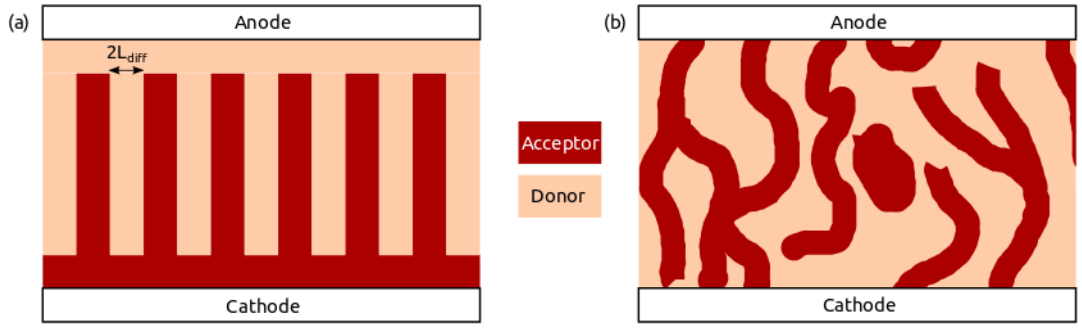

Figure 2.4: Schematic cross-sections of the nano-morphologies of BHJ solar cells. (a) Ideal BHJ morphology with the length scale of the phase separation equal to the exciton diffusion length L_{diff}. (b) Typical BHJ morphology of a solution processed device.

Up to now, the bulk heterojunction remains the most successful device architecture for organic solar cells. Due to the intrinsic tendency of polymers for phase separation in binary mixtures, the formation of a BHJ in solution processed donor-acceptor blends is a spontaneous process. Yet a lot of research is still going on to improve the BHJ nano-morphology. In figure 2.4 the suggested ideal morphology of a BHJ solar cell is compared to what is probably the more typical morphology obtained in a solution processed BHJ device. Factors influencing the BHJ morphology are for example the donor acceptor ratio of the blend, the solvent used during solution processing of the active layer and thermal treatment (annealing) of the resulting film. Very recently Liu et al. [9] reported on high efficiencies ($> 10\%$) achieved for different polymer:fullerene systems by aggregation and morphology control. They succeeded in increasing the efficiency of state-of-the-art material systems by combining a near-ideal morphology with highly crystalline polymer domains. Hence controlling the nano-scale phase separation in BHJs will be an important key factor for improving power conversion efficiencies of organic solar cells.

2.3 Device lay-out of bulk heterojunction organic solar cells

Figure 2.5 shows a simplified band diagram for a BHJ OSC device. The anode consists of a high work function material to extract holes from the organic layer. A low work function metal then serves as cathode to extract the electrons. Injection barriers for holes and electrons can arise from an energetic misalignment between the work function of the electrode and the donor HOMO respectively acceptor LUMO energy level. Therefore thin charge transport layers between the metallic contact and the organic layer are often used to lower this energy barrier thereby facilitating charge transport from the organic material to the electrodes. In any case, careful consideration of the choice of cathode and anode material and the use of electron and hole transport layers is of crucial importance for a successful device lay-out.

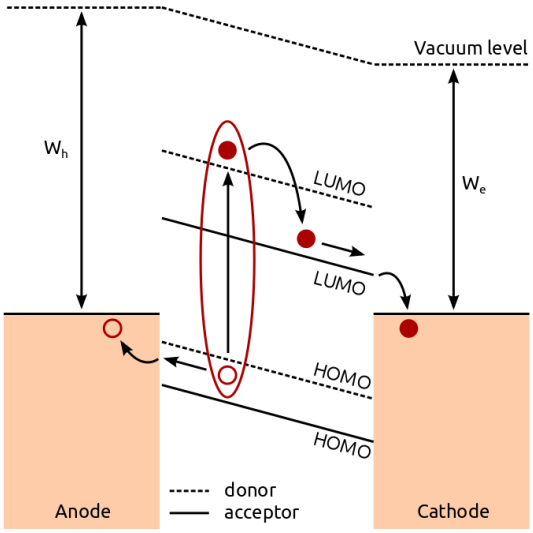

Figure 2.5: Simplified band diagram of an BHJ organic solar cell with electrode work functions $W_e < W_h$ at zero bias. In equilibrium the Fermi levels of the anode and cathode are equal.

A typical device configuration of a BHJ OSC is shown in figure 2.6. Due to its high optical transparency, indium tin oxide (ITO) is the most commonly used transparent conductor in OPV. A layer of poly(styrenesulfonate) doped poly(3,4-ethylenedioxythiophene) or PEDOT:PSS is often coated on top of the ITO electrode to improve hole transport to the anode and to smoothen the ITO surface. The active layer consisting of the bulk heterojunction of donor and acceptor material is either applied by spin coating from solution or by coevaporation. As a last step the metallic top electrodes are thermally evaporated in a high vacuum set-up. Low work function metals such as Ca that match well with the LUMO of the acceptor are highly reactive and lead to a fast degradation of the device in ambient conditions. Often more stable Al electrodes are used instead despite the higher electron injection barrier. The use of an additional electron transport layer such as LiF is then necessary.

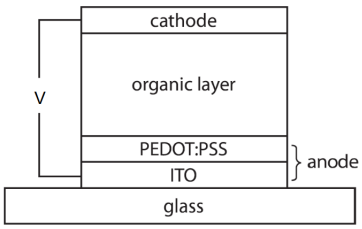

Figure 2.6: General device lay-out of an organic solar cell. Figure adapted from [15].

The use of ITO electrodes in organic solar cells greatly increases the energy and material cost of the devices. Not only because indium is a scarce and expensive material, the production of ITO electrodes via vacuum-based sputtering is also a highly energy-intensive process. Hence the use of ITO is not compatible with the objective of low-cost organic photovoltaics with low environmental impact. Moreover, ITO is not suitable for flexible optoelectronic applications as it is brittle and difficult to combine with flexible substrates. Research towards a possible replacement for ITO is therefore indispensable in the further development of plastic electronics and commercially viable organic solar cells. Alternatives for ITO include transparent conducting polymers, metal and polymer composites, metal nanowires, ultra-thin metal films, carbon nanotubes and graphene [2].

2.4 Solar cell parameters

The most important figure of merit describing the device performance of a solar cell is the power conversion efficiency η. This parameter is calculated from the maximum generated power P_{max} obtained from the current-voltage characteristic of the solar cell under illumination. Figure 2.7 shows a typical current-voltage characteristic of a BHJ solar cell where P_{max} is indicated by the orange rectangle.

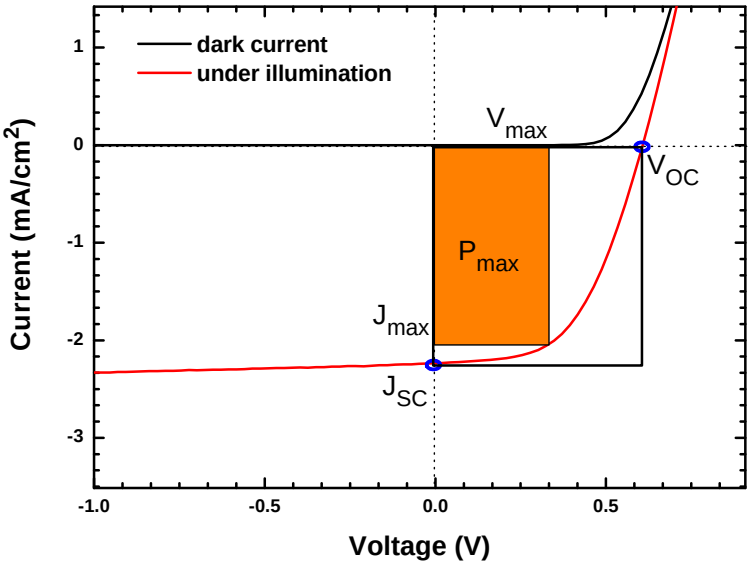

Figure 2.7: Schematic diagram of the current-voltage characteristic of an organic solar cell in the dark and under illumination. The relevant parameters discussed in the text, i.e. V_{oc}, J_{sc} and the maximal power P_{max}, are indicated on the graph. Figure taken from [10].

The power conversion efficiency is then given by the ratio of the maximum power to the incident solar power P_L:

$$\eta = \frac{P_{max}}{P_L}$$

Often one introduces a fill factor FF to relate the power conversion efficiency to the open circuit voltage V_{oc} and the short circuit current J_{sc} that can be easily obtained from the current-voltage characteristic of the solar cell (figure 2.7). The fill factor is defined as the ratio of the maximum generated power P_{max} to the product of V_{oc} and J_{sc}:

$$\mathrm{FF} = \frac{P_{max}}{J_{sc}V_{oc}}.$$

Hence we obtain the following expression for the power conversion efficiency η:

$$\eta = \frac{J_{sc}V_{oc}\mathrm{FF}}{P_L}.$$

In order to improve the device performance of an organic solar cell η, V_{oc}, J_{sc} and FF should be increased simultaneously. A rough guide for the V_{oc} of an OSC is given by the energy difference between the LUMO of the acceptor and the HOMO of the donor. Therefore a common approach to enhance V_{oc} is to choose combinations of donor and acceptor materials with an energetic alignment that maximizes the size of this so-called 'effective' bandgap. Meanwhile, it should be kept in mind that increasing the donor and acceptor bandgap limits the overall absorption of sunlight by the device. Hence, despite the lower open circuit voltages, there is a trend for using low bandgap polymers such as P3HT to optimise light absorption by the solar cell. Moreover, increasing the size of the effective bandgap will also reduce the driving force for charge separation at the D/A interface given by the energy offset between the donor and acceptor LUMOs. The result will be a reduction of the photocurrent. Hence, in order to ensure a sufficient driving force for charge transfer a minimum LUMO offset of 0.3 eV is often advised [14]. Nevertheless, solar cell operation under low driving force conditions is the subject of current OPV research as a possible pathway to higher power conversion efficiencies [11]. Other factors influencing the photocurrent besides the LUMO levels are the blend morphology, the presence of injection barriers at the metal contacts and several loss mechanisms that reduce the number of charge carriers via trapping or recombination.

2.5 Loss mechanisms

Not all photogenerated excitons will eventually contribute to the photocurrent. Different loss mechanisms can occur during all steps of the photovoltaic process. A fundamental understanding of the dominant loss mechanisms in organic solar cells is hence essential for further improvement of power conversion efficiencies. In this section the most important processes will be discussed.

The first step of the photovoltaic process consists of the dissociation of photogenerated excitons into free charge carriers. All exciton decay processes that compete with exciton quenching at a D/A interface will then result in a first loss of possible charge carriers. Figure 2.8(a) summarises the dominant exciton decay channels. An important concept here is the total spin state of the exciton. Excitons created upon illumination will always be in a singlet state, i.e. total spin equal to zero. These singlet excitons have a large probability of decaying either non-radiatively or in the form of photoluminescence (PL). Yet, in conjugated polymers a triplet state with total spin equal to one usually lies lower in energy than the singlet. Therefore also a transition from singlet to triplet via intersystem crossing (ISC) can take place. The transition from the triplet state to the groundstate is spin-forbidden. Hence the triplet excitons are relatively long-living states and they will ultimately decay non-radiatively or in the form of phosphorescence.

Yet, for suitable material combinations the quenching of excitons due to charge transfer at the D/A interface will be much faster than any competing loss processes such as photoluminescence or ISC. Therefore the critical factor for eliminating preliminary exciton losses will be the length scale of the BHJ phase separation. Indeed, when the exciton diffusion length determined by the exciton lifetime and mobility exceeds this length scale, an exciton quenching of near 100% can be achieved.

Low-lying triplet states can however participate in another detrimental recombination process as shown in figure 2.8(b). After charge transfer (CT) the electron and hole reside on different

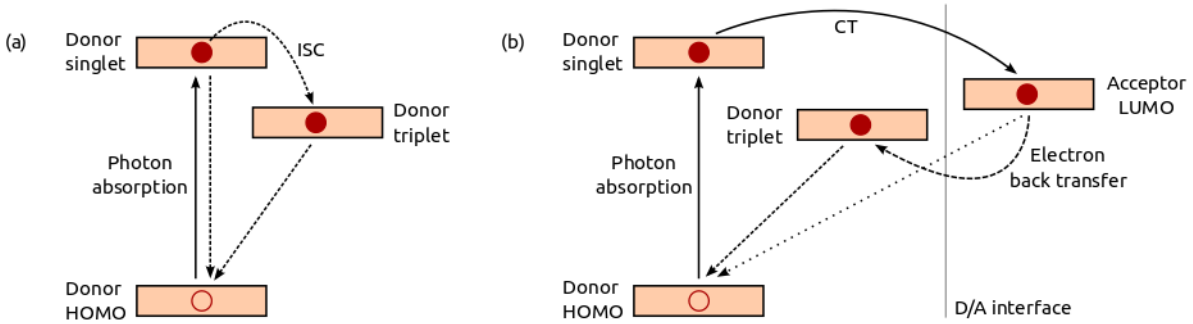

Figure 2.8: Loss mechanisms before (a) and after charge transfer at the D/A interface (b). Solid lines are used for necessary processes in the exciton dissociation process; dashed and dotted lines denote detrimental recombination channels.

molecules but they are still Coulomb bound. Such an electron-hole pair is often called a polaron pair or charge transfer complex. In order to generate free charge carriers, the binding energy of this polaron pair still needs to be overcome. Hence a polaron pair represents an intermediate state between the photogenerated exciton and the free charge carriers. After CT, an interfacial polaron pair can either dissociate into free charges or recombine via some kind of loss mechanism. Direct radiative decay of the polaron pair gives rise to CT photoluminescence which is characterised by significantly lower photon energies than the donor PL. Hence the presence of a CT band in the PL spectrum of a donor-acceptor blend is a good indication for successful charge transfer at the D/A interface. Another possible recombination pathway of the polaron pair involves the donor triplet state. When the energetic alignment between donor and acceptor is such that the donor triplet lies below the acceptor LUMO level, an electron back transfer across the D/A interface can occur. The resulting triplet exciton can then decay non-radiatively or via phosphorescence.

Even when the exciton is successfully dissociated into free charge carriers, various loss mechanisms can still occur during charge transport and charge extraction at the electrodes. For example, charges can become trapped in low-energy states in the tail of the density of states (figure 2.2) or they can recombine when they encounter oppositely charged polarons. Remark that the nature of these recombination processes is different from the ones displayed in figure 2.8 as they involve charge carriers that do not originate from the same photon excitation. This type of recombination will be referred to as non-geminate recombination. Recombination between polarons created by the same photon-event is called geminate recombination. In chapter 4 the difference between these two types of recombination will be discussed in more detail.

2.6 Background and motivation for this thesis

Although many conjugated polymers exhibit very high absorption coefficients, their absorption width is in general rather narrow as compared to inorganic semiconductors. Hence only a part of the solar spectrum is exploited in most organic solar cells where light is mainly absorbed by the donor polymer. In section 2.2.2 of this chapter we already mentioned the limited light absorption by commonly used fullerene acceptors. Hence an approach for potential PCE improvement would be to find alternative acceptors that exhibit good absorption properties in an absorption range complementary to that of the donor. Such devices would benefit from a broader range of the solar spectrum which could drastically increase the solar cell performance. Other disadvantages of fullerene acceptors are the limited chemical versatility and the high production cost which is considered a significant obstacle in the further development of low-cost OPV. Hence the search for alternative acceptors is very relevant in current OPV research.

In this thesis newly synthesized DTTzTz acceptor materials are studied in combination with standard donor polymers. As such we contribute to the research on alternative acceptor materials. Furthermore we also investigated a novel DTTzTz donor molecule in combination with PC70BM, a fullerene acceptor. This donor-acceptor combination was known to yield relatively successful solar cell devices with PCEs of about 3%. Another objective of this thesis was to gain a more fundamental understanding of the recombination processes that limit the solar cell efficiencies in these systems. To that end we performed photo-induced absorption (PIA) measurements that directly detect excitations of the photogenerated polarons in the blends. Via theoretical models for the polaron generation and recombination kinetics it is possible to fit the experimentally observed time-dependence of the PIA and to study the nature of the recombination processes.

Chapter 3

Experimental Methods

A major part of the research in organic photovoltaics involves the development of new materials to improve solar cell efficiencies and device stability or to find low-cost alternatives for current OPV materials. Also in this thesis a series of novel small molecules for use in bulk heterojunction organic solar cells is studied. This chapter provides an overview of the sample preparation and the spectroscopic techniques used to characterize these new materials.

3.1 Materials

The materials studied in this thesis are chosen from a series of novel small molecules recently synthesized by the group of prof. dr. Wouter Maes at the Institute for Material Research (IMO) of UHasselt [8]. The molecules consist of a dithienylthiazolo[5,4-d]thiazole (DTTzTz) base unit along which additional substituents are introduced to tune the energy levels (HOMO and LUMO) of the molecule. Solubility of the molecules was improved by additional alkyl chains in order to enable solution processing. Because of the tailor-made energy levels the materials are suitable for use as either donor or acceptor material in BHJ organic solar cells depending on the side groups. The acceptor molecules are of particular interest as they could prove to be promising alternatives for the expensive fullerene derivatives that dominate the current OPV research.

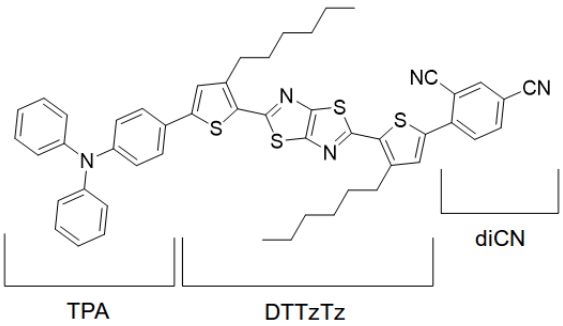

Figure 3.1: Molecular structure of TPA-DTTzTz-diCN. Figure taken from [8].

Figures 3.1 and 3.2 show the molecular structure of the three molecules that were selected for study during this thesis. TPA-DTTzTz-diCN will be studied as a donor material in blends with the fullerene derivative PC70BM. The symmetric molecules diCN-DTTzTz-diCN and CN-DTTzTz-CN were chosen for use as acceptor in combination with the standard donor polymers MDMO-PPV and P3HT. The DTTzTz base unit and the triphenylamine (TPA), benzonitrile (CN) and benzodinitrile (diCN) side groups are explicitly indicated in figures 3.1 and 3.2. The molecular structures of PC70BM, MDMO-PPV and P3HT are depicted in figures 3.3 and 3.4.

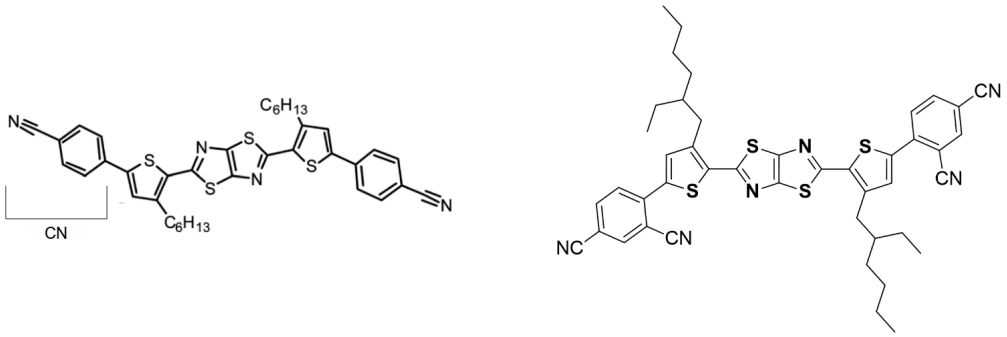

Figure 3.2: Molecular structure of CN-DTTzTz-CN and diCN-DTTzTz-diCN. The branched alkyl chains in diCN-DTTzTz-diCN ensure high solubility. Figures provided by the group of prof. dr. Wouter Maes.

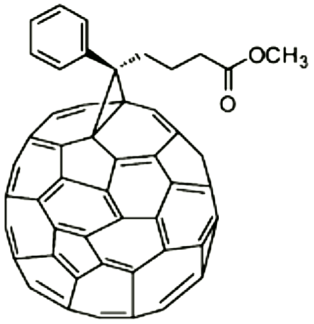

Figure 3.3: Molecular structure of the fullerene acceptor PC70BM. Figure taken from [4].

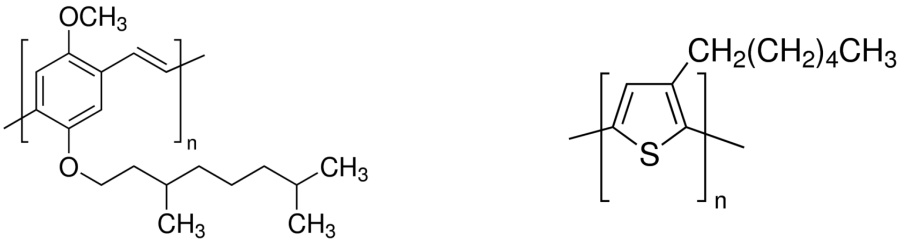

Figure 3.4: Molecular structure of the donor polymers MDMO-PPV and P3HT. Figures taken from [16]

The HOMO and LUMO levels of the donor and acceptor materials under study are shown in figure 3.5. The energy levels were obtained experimentally by solution cyclic voltammetry [11]. The combination of CN-DTTzTz-CN with MDMO-PPV was already intensively studied by Nevil [10] as a promising route to high V_{oc} devices due to the large effective bandgap in this donor-acceptor system. Yet, the small energy difference between the LUMOs of MDMO-PPV and CN-DTTzTz-CN results in a low driving force for charge separation at the D/A interface. As a result solar cells based on these materials showed poor photocurrent generation and maximum PCEs of only 0.1% were obtained. Therefore we selected the diCN-DTTzTz-diCN molecule for study as it exhibits lower LUMO and HOMO levels corresponding to an increased electron-acceptor strength. As such we expect to find an improvement of the CT efficiency in blends of diCN-DTTzTz-diCN with MDMO-PPV. Also the trend in CT efficiency when replacing MDMO-PPV by the low-bandgap polymer P3HT was studied. In the TPA-DTTzTz-diCN:PC70BM system, a high CT efficiency can be expected based on the large energy offset between donor and acceptor HOMOs and LUMOs in figure 3.5 resulting in a strong driving force for charge transfer at the D/A interface.

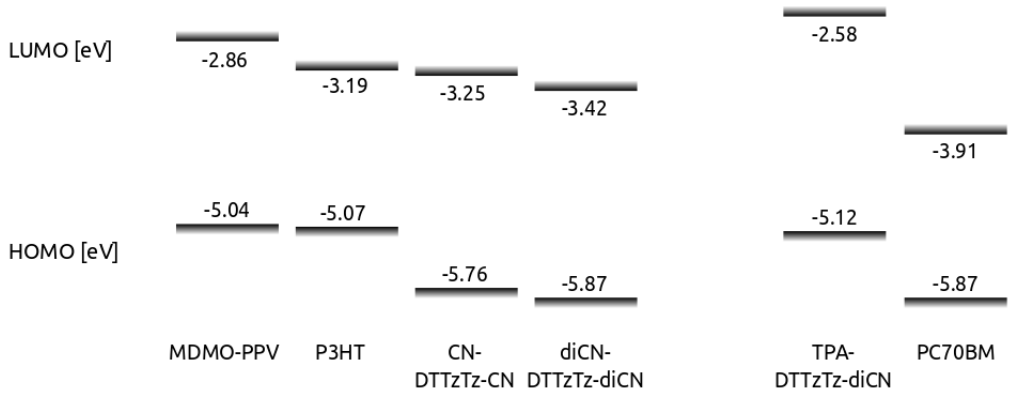

Figure 3.5: HOMO and LUMO levels of the novel DTTzTz molecules according to cyclic voltammetry data [8], [11]. Energy levels of PC70BM from [1].

3.2 Sample preparation

All experimental work in this thesis was performed on thin films of the pristine materials and donor:acceptor blends similar to the active layer in organic solar cells. The films were applied on glass substrates by spin coating from solution. The first part of this section describes the solution preparation details. The spin coating process is treated in the second part.

3.2.1 Solutions

The materials were first weighed on an analytical balance of 10 µg precision. The required amount of solvent was then pipetted into the vial containing the weighed material. The pure films were prepared from 10 mg/ml solutions. The solutions for the blends all contained 10 mg/ml of the DTTzTz compound and were then completed with the required amount of PC70BM or donor polymer to yield the correct donor:acceptor weight ratio. As such the 1:3 TPA-DTTzTz-diCN:PC70BM blend was prepared from a 40 mg/ml solution and the 1:1 blends of the DTTzTz acceptor molecules with MDMO-PPV or P3HT from 20 mg/ml solutions. Chlorobenzene was used as solvent in all solutions, except for the solution for the pure CN-DTTzTz-CN film which was prepared with chloroform. To ensure that the small molecules were properly dissolved the solutions were stirred overnight at a temperature of 60 °C.

3.2.2 Spin coating

The glass substrates consisted of manually cut microscope slides. The substrates were first cleaned with detergent to remove organic contamination. Afterwards they were rinsed with water followed by ultrasonic cleaning in acetone to remove any remaining detergent traces. The spin coating itself took place inside a nitrogen glove box. All films were spin coated at 700 rpm during 60 s. Afterwards they were left to dry inside the glove box for at least one day. After drying, all finished samples were kept in the dark in a nitrogen atmosphere to prevent photodegradation of the films.

3.3 Optical characterisation methods

3.3.1 UV-VIS absorption spectroscopy

For any new material designed for application in organic solar cells, the first property to investigate is its ability to absorb sunlight. Therefore UV-VIS absorption spectroscopy is a widely applied technique in OPV reseach. Apart from determining the absorption bands of the materials under study, the technique can also provide useful information on the vibrational structure of the molecules, the interaction between different molecules in blends or even the film morphology.

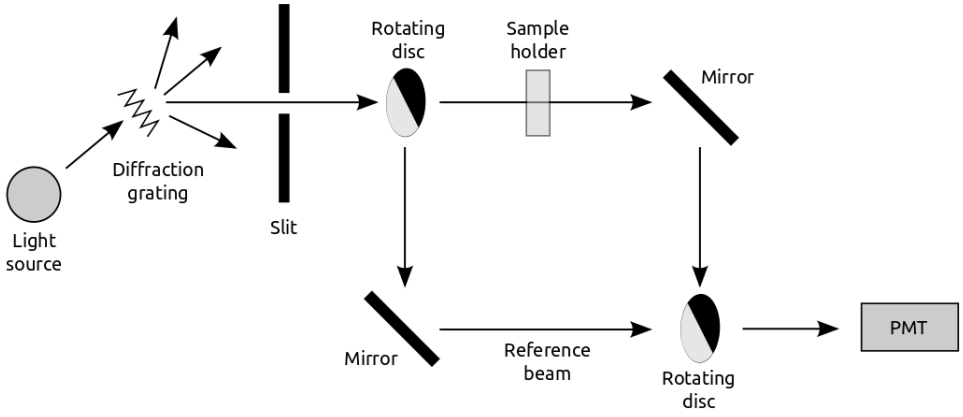

Figure 3.6: Schematic diagram of the UV-VIS absorption set-up.

The UV-VIS absorption spectroscopy measurements were performed on a Varian Cary 5E spectrophotometer in double beam mode. A schematic representation of the experimental set-up is shown in figure 3.6. In order to cover a broad wavelength range, the spectrophotometer contains two light sources: a halogen lamp for the VIS and NIR part of the spectrum and a deuterium lamp for UV light. The light source is followed by a rotating diffraction grating monochromator such that only monochromatic light of the desired wavelength can pass through the slit towards the sample. By rotation of the diffraction grating, the wavelength of the incident light is varied and a spectrum can be obtained. Before the light beam reaches the sample, it is modulated by means of a system of rotating discs with alternating transparent and reflective sections. As a result the incident light beam is distributed periodically over two different paths of equal length. Only one of the paths passes through the sample such that both the transmitted intensity $I(\lambda)$ and the intensity $I_0(\lambda)$ of the incident light will be detected by the photomultiplier (PMT). From the periodic signal containing both $I(\lambda)$ and $I_0(\lambda)$ the transmission spectrum $T(\lambda)$ can be calculated as follows:

$$T(\lambda) = \frac{I(\lambda)}{I_0(\lambda)}.$$

In homogeneous materials every layer dl absorbs an equal amount of light. Therefore we have that

$$dI = -aIdl, \tag{3.1}$$

with a the linear absorption coefficient. Integrating equation (3.1) yields Lambert-Beer's law which states that the transmitted intensity decreases exponentially with the sample thickness L:

$$I = I_0 e^{-aL} = I_0 10^{-\alpha L},$$

where both a and $\alpha = a\log(e)$ are referred to as absorption coefficients but α is the standard definition used in UV-VIS spectroscopy. A common measure for the absorption of a film is the absorbance $A(\lambda)$ or optical density defined as

$$A = \alpha L = \log\left(\frac{I_0}{I}\right).$$

The absorbance of the sample can be directly calculated by the spectrophotometer software. Note that the absorbance depends on the film thickness. Hence a quantitative comparison of absorbance spectra of different samples with unknown film thickness is somewhat arbitrary. Yet, the film thickness of the samples can be obtained from additional experiments such that the absorbance intensities can be corrected for the sample thickness. Otherwise, if the absorption coefficient is known from earlier measurements, the absolute intensity of the absorbance can be used to determine the film thickness of a sample. In this thesis the film thickness of the different samples is unknown. Yet, qualitative information can still be obtained from the shape of the absorbance spectra.
In order to correct for absorption by the glass substrate, the absorption spectrum of a cleaned glass substrate was subtracted from every measurement. Nevertheless, glass is highly transparent to the wavelength range of our interest and will not contribute significantly to the total absorption spectrum.

3.3.2 Photoluminescence spectroscopy

Photoluminescence (PL) originates from the radiative decay of photoexcited molecules. In OPV research, the comparison of PL spectra of donor:acceptor blends with the PL of the pristine materials provides a tool for characterising the CT process. Indeed, excitons with a certain probability of recombining radiatively in the pristine materials can become quenched at a D/A interface in blends. Hence the charge transfer process will compete with radiative decay of the excitons. As a result the PL intensity of the blend decreases and may even reveal a CT band at longer wavelengths arising from radiative decay of the formed charge transfer complexes. PL quenching is considered an important indicator for the efficiency of the CT-process and the fraction of photo-generated excitons reaching the D/A interface. However, PL quenching can also be attributed to non-radiative mechanisms which cannot be easily distinguished from the CT process [11]. In such cases complementary techniques for investigating charge generation and recombination such as photo-induced absorption (PIA) spectroscopy allow to differentiate CT from other processes.
Figure 3.7 shows a schematic representation of the PL set-up. The samples were mounted in a cryostat under vacuum to minimize photo-oxidation of the films and all measurements in this work were performed at liquid nitrogen temperature. A 447 nm diode laser was used for photoexcitation of the molecules. The parallel laser beam was focused on the sample with a lens. Backscattered PL was collected by the same lens and directed by a second lens onto the narrow entrance slit of the diffraction grating monochromator. The diffracted PL is then detected by a linear CCD detector consisting of an array of photodiodes. By careful calibration

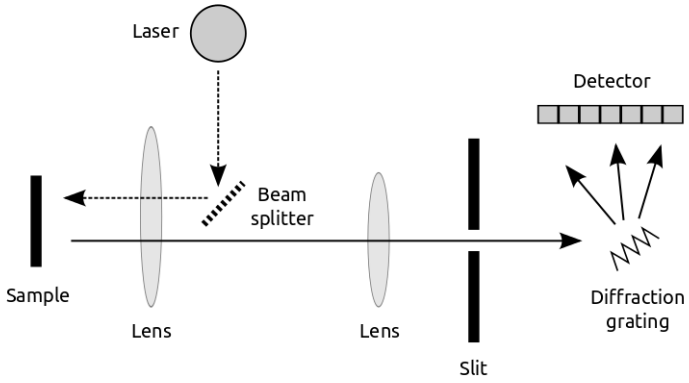

Figure 3.7: Schematic diagram of the PL set-up.

a relation between the position of each photodiode and the wavelength of the incident light can be obtained such that the recorded intensities can be expressed in function of wavelength. In order to prevent elastically scattered laser light from entering the monochromator, a 532 nm cut-off filter and a 495 nm cut-off filter are placed respectively after the lens and in front of the entrance slit. The resulting PL spectra still need to be corrected for the wavelength dependent sensitivity of the set-up including the effect of the lenses, the monochromator, the detector and the cut-off filters. This correction factor is obtained by comparing the measured spectrum of a halogen lamp with the theoretical spectrum for black body radiation at 3200 K, the estimated temperature of the lamp, according to Planck's law:

$$I(\lambda) = \frac{2\pi hc^2}{\lambda^5} \frac{1}{\exp\left(\frac{hc}{\lambda kT}\right) - 1}.$$

The correction factor is then defined as the ratio of the measured spectrum and the theoretical spectrum which are both shown in figure 3.8. The measured spectrum of the halogen lamp clearly demonstrates that the cut-off filters prevent most of the light with a wavelength below 532 nm from entering the monochromator.

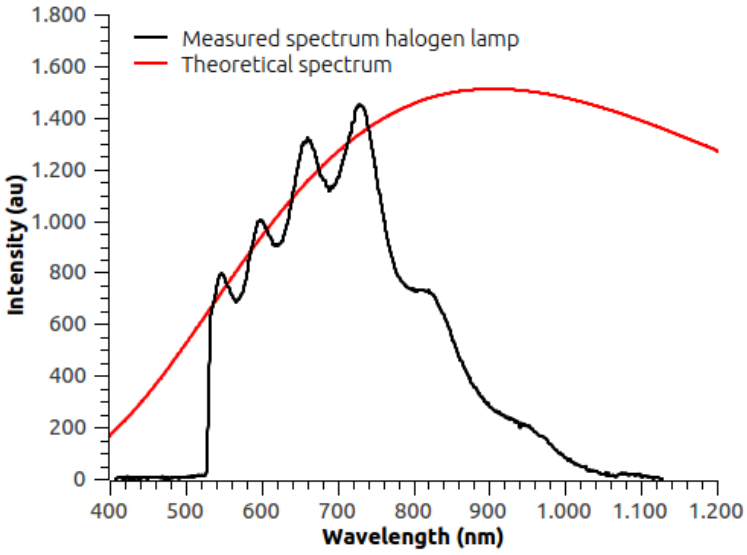

Figure 3.8: Comparison of the measured spectrum of a halogen lamp and the theoretical spectrum for black body radiation at 3200 K from Planck's law.

3.3.3 Photo-induced absorption

Photo-induced absorption (PIA) probes the absorption of white light by transient species created by laser excitation. Usually one distinguishes between pulsed laser PIA and continuous wave (CW) PIA where the laser beam is modulated by means of a mechanical chopper or an opto-acoustic modulator. CW-PIA is particularly suited to study excited species in OSC materials because it requires only moderate excitation intensities similar to solar illumination levels. In pulsed laser PIA experiments, on the contrary, much higher laser powers are required. Moreover, depending on the period of the laser modulation, either short or long-living excitations can be investigated. Hence PIA is a powerful tool that allows to study a system on different time scales. In general, PIA is mainly used to study the absorption spectrum of the excited species by analysing the photo-induced changes in absorption for variable wavelengths. This technique is referred to as wavelength-dependent PIA. Yet, in this thesis we also investigate the time-dependence of the PIA to study the generation and recombination dynamics of the excited species. The latter is denoted by time-resolved PIA (TR-PIA).
In this thesis CW-PIA is used for the detection of relatively long-lived positive polarons in donor-acceptor blends. These polarons are created by charge separation of photogenerated excitons at the D/A interface. The positive polaron which resides on the donor material can in turn jump to an excited state by absorbing a photon from the probe light. In the orbital picture an excitation of a positive polaron corresponds to a transition of an electron from a lower energy state to the singly occupied HOMO level as shown in figure 3.9(a). The resulting PIA signal is then a measure for the positive polaron concentration in the blend. Note that also negative polarons can absorb probe light corresponding to excitations of the single electron in the acceptor LUMO as shown in figure 3.9(b). Yet, for common acceptors such as PC70BM these transitions correspond to IR photon energies far beyond the spectral sensitivity of our experimental set-up. Hence in those systems we will not be able to detect absorption by negative polarons. Unlike the ambiguity between CT and non-radiative decay as underlying mechanism for PL quenching, PIA can distinguish between both processes and directly demonstrate successful charge transfer in blends. Nevertheless, it should be noted that also other excitations such as triplet excitons can contribute to the PIA such that the observed signal may not be solely ascribed to polarons. One way to distinguish between different types of excited species is by comparing the wavelength dependent PIA spectra with known polaron bands from the literature. Also the time-dependence of the PIA signal provides useful information on the nature of the transient species as it allows to estimate the lifetime of the excitations and to evaluate the dominant recombination mechanisms.

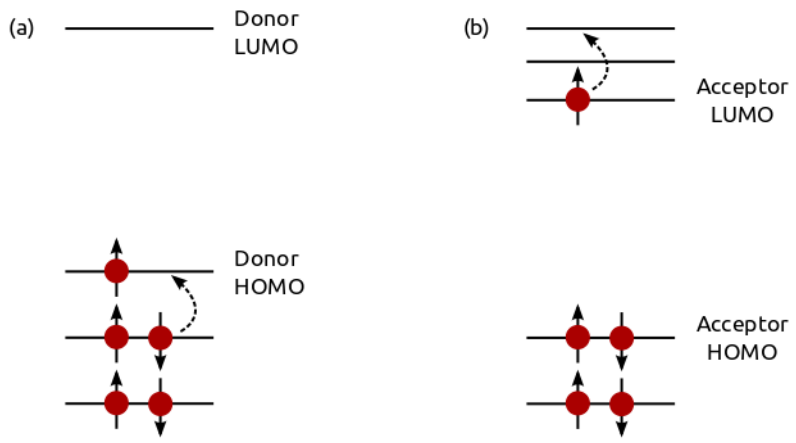

Figure 3.9: Schematic representation of an excitation of (a) a positive polaron on the donor and (b) a negative polaron on the acceptor.

As mentioned before, PIA measurements can be performed in either time-resolved (TR) or wavelength-dependent mode. In TR-PIA the kinetics of the excited species is studied by directly probing the response of the system on the on/off modulation of the laser excitation. Hence this technique is particularly suited to investigate charge generation and recombination dynamics in OSC materials. A typical result of a TR-PIA measurement is shown in figure 3.10. This signal is obtained by filtering out the AC component of the probe light transmitted through the sample. The red dashed lines indicate the on- and off-period of the laser excitation. Hence figure 3.10 clearly demonstrates that the PIA is in phase with the square-wave modulation of the laser. Several physical models exist to describe polaron recombination in blends. With these models it is possible to fit experimental TR-PIA data to study the nature of the recombination mechanisms and to extract useful information such as the polaron lifetime from the fitting parameters. In this thesis modelling played a major role in the interpretation of the experimental data. An overview of these models and their underlying physical mechanisms will be the subject of the following chapter.

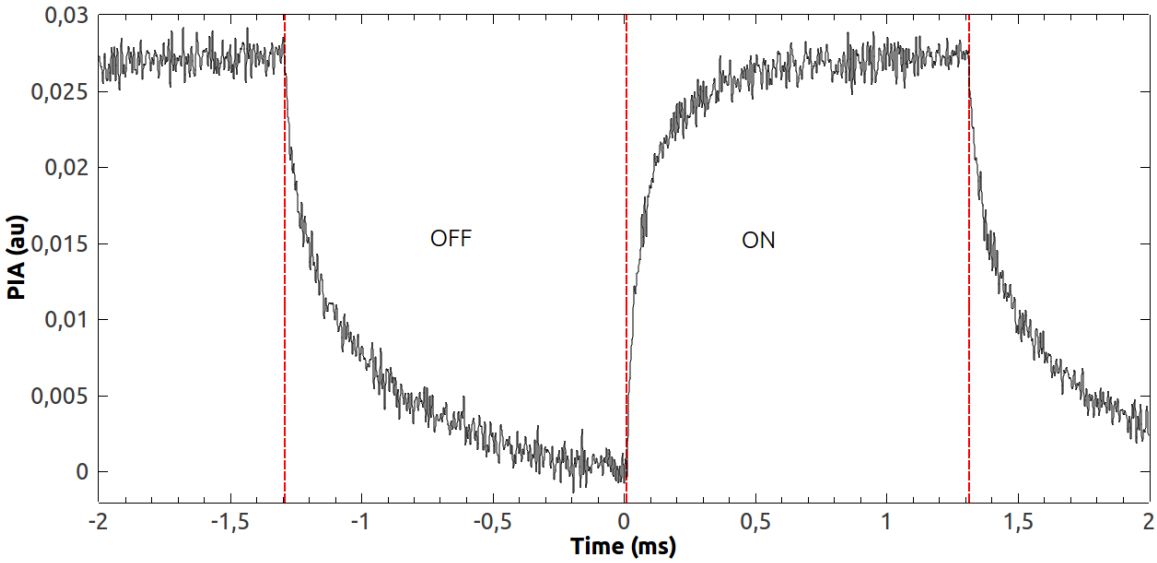

Figure 3.10: Example of a TR-PIA measurement on a TPA-DTTzTz-diCN:PC70BM blend with $\lambda_{probe} = 870\,\text{nm}$ and modulation frequency of the laser equal to 384 Hz. The curve is shifted vertically such that the PIA equals zero at the end of the off-period.

In wavelength-dependent PIA the absorption spectrum of the photoexcited species is measured by varying the wavelength of probe light that is registered by the detector. If the resulting excitation spectrum arises from polarons in an OSC blend the PIA spectrum is also referred to as the polaron band. A PIA spectrum is obtained by integrating the in-phase Fourier component corresponding to the modulation frequency, i.e. the amplitude of the AC signal component that oscillates in phase with the on/off modulation of the laser, over longer timescales and repeating this procedure for different wavelengths. Hence a CW-PIA spectrum is obtained through a series of integrated TR-PIA measurements.
The PIA measurements were performed with an Edinburgh Instruments LP920 spectrometer which was originally intended for laser flash photolysis. The experimental set-up was modified by Nevil [10] to enable PIA measurements on thin films and is schematically depicted in figure 3.11. The samples are again mounted in a cryostat under vacuum to avoid degradation of the films and the experiments were performed at liquid nitrogen temperature. In PIA measurements one is interested in the photoinduced change in the absorption of probe light by the sample. To that end the samples are excited by a 532 nm frequency-doubled Nd:YAG laser which is on/off modulated by an opto-acoustic modulator. The laser beam is guided by mirrors

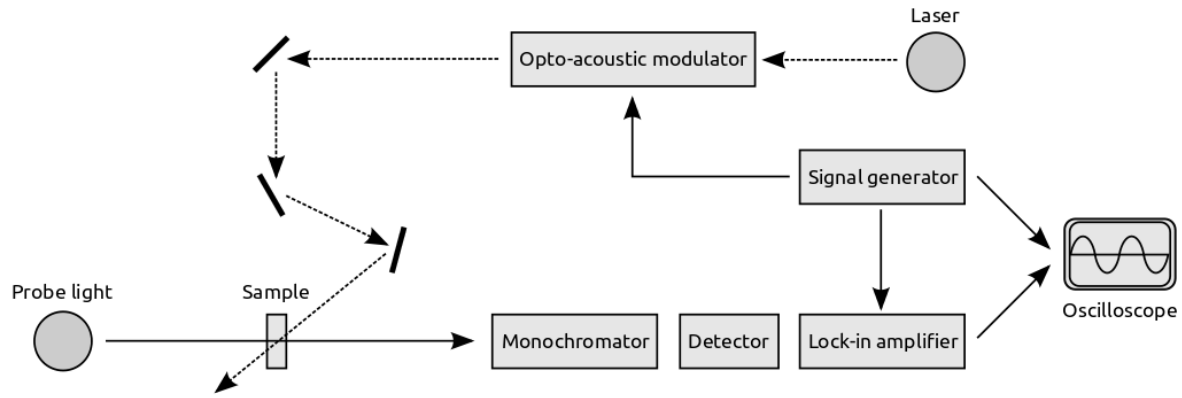

Figure 3.11: Schematic diagram of the PIA set-up.

such that probe beam and laser beam almost collinearly overlap on the sample. The maximal laser power used during experiments was 12 mW on average, i.e. 24 mW during the on-period and 0 mW during the off-period of the modulation. Together with an estimated excitation area of 10 mm^2, this yields illumination levels similar to the intensity of sunlight $\sim 100\,mW/cm^2$. White light from a halogen lamp was used as probe beam. In order to minimize photodegradation of the films, a 560 nm long-wavelength pass (LWP) filter was placed before the sample to eliminate UV light from the probe beam. Scattered laser light was prevented from entering the monochromator by a 580 nm LWP filter before the entrance slit. The diffraction grating monochromator then selects a single wavelength from the probe light transmitted through the sample for detection. Two different detectors were employed depending on the wavelength range of the PIA spectrum. Figure 3.12 shows the spectral sensitivity of the set-up with the Si and InGaAs photodiode detectors. The spectral sensitivity is obtained by measuring the transmission of halogen light through the sample without laser excitation. In general, the Si detector was preferred as it yields better signal-to-noise ratios. However, for PIA spectra that extend beyond 1100 nm in the near infra-red the InGaAs detector is clearly the better choice.

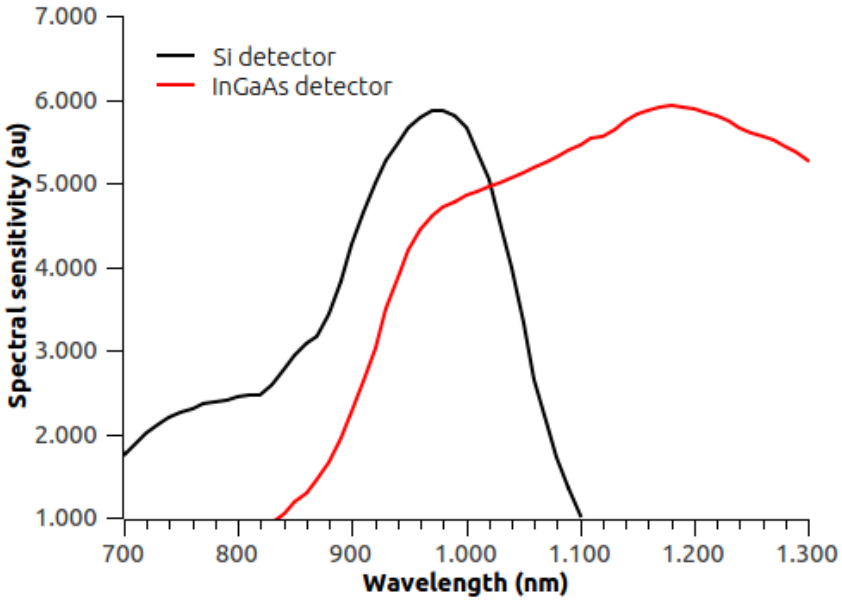

Figure 3.12: Comparison of the sensitivity range of the set-up for the Si and the InGaAs detector.

The changes in absorption of probe light induced by the on/off modulated laser excitation are typically very small: of the order of several mV on a total signal of about 3 V corresponding to photo-induced changes of only 0.1%. Therefore the signal recorded by the Si or InGaAs detector will consist of a large DC background and only a small periodic contribution corresponding to the PIA. In order to extract the periodic component from the total signal with sufficient signal-to-noise ratio a lock-in amplifier is used. In general, the lock-in detector determines both in-phase (cosine) and out-of-phase (sine) Fourier components corresponding to the modulation frequency. Yet, in our measurements the modulation was always slow as compared to the response time of the system such that the PIA signal is completely in phase with the modulation (see figure 3.10). Hence the lock-in detector was used to filter out and amplify only the signal component that is in phase with the square wave modulation from the signal generator. The result is a DC signal corresponding to the intensity of the PIA. In wavelength-dependent PIA this signal can be registered by the digital storage oscilloscope during several seconds. Repeating this procedure for multiple wavelengths and integrating the time-averaged signals then yields the PIA spectrum of the sample. In TR-PIA however, we are interested in the dynamic response of the PIA on the on/off modulation of the laser. Therefore we will use the lock-in detector merely as a low-noise preamplifier for the PIA signal that is subsequently transferred as a periodic signal to the digital storage oscilloscope. This signal can then be averaged over a large number of modulation periods by the oscilloscope to improve the signal-to-noise ratio.

The recorded PIA signals could still contain contributions from photoluminescence of the samples. PL corresponds to an increase of probe light intensity and contributions from PL therefore appear as negative PIA signals. The effective PIA signal is then obtained by subtracting a background measurement without probe light. In the case of wavelength-dependent PIA, the spectra also need to be corrected for the sensitivity of the experimental set-up including the effect of the detector, the monochromator and the used filters as shown in figure 3.12.

In the course of this work, we developed an alternative, more intuitive measuring technique for the wavelength-dependence of the PIA. Instead of using the lock-in detector to filter out the in-phase Fourier component of the signal, we directly registered the oscillating PIA signal on the digital storage oscilloscope by means of an AC Si detector. The PIA spectrum can then be obtained by taking the Fourier transform of the time-dependent PIA signals measured for different wavelengths. The signal-to-noise ratios achieved with this alternative technique were appreciably lower than in the measurements via the lock-in detector for comparable integration times. Therefore we eventually decided to perform all wavelength-dependent PIA measurements via the lock-in amplifier.

Chapter 4

Modelling of charge generation and recombination in organic solar cells

In the previous chapter we concluded that TR-PIA is particularly suited to investigate the dynamics of charge generation and recombination in organic materials. By modelling the data it is possible to extract relevant information on the nature of the recombination processes from the experimental results. In this chapter two different models describing the rise and decay period of the TR-PIA are proposed: the monomolecular and bimolecular model corresponding respectively to geminate and non-geminate recombination of charge carriers. The difference between these two types of recombination and their impact on the photovoltaic device performance is discussed in the first part of this chapter. The rest of the chapter treats the mathematical formulation of the models and the fitting procedure. In addition to the monomolecular and bimolecular models used by Nevil [10] to fit PIA data we will present an extension to both models by including the effect of ground state depletion. In the results chapters the models introduced here will be used to fit the experimental data and to conclude which physical mechanism governs the charge recombination.

4.1 Geminate and non-geminate recombination

In order for an organic solar cell to work, two distinct processes need to occur: (1) photogeneration of free charge carriers and (2) transport of the photogenerated charge carriers towards the electrodes where the charges can be extracted. During both processes, detrimental recombination of electrons and holes can take place although the nature of the recombination process is different. During the first step, the exciton created by an incident photon can dissociate into free charge carriers by forming a charge transfer complex at a D/A interface. Recombination of excitons can occur either before they reach the D/A interface or by recombination of the CT complex. In both situations, the electron and hole involved in the recombination process originated from the same photon. This type of recombination is called geminate recombination and is independent of the population of other charge carriers. Therefore it is described as a monomolecular process. Once the charge carriers are successfully separated, the free electron and hole drift towards their respective electrodes. During this step, recombination can still occur when the dissociated carriers encounter another oppositely charged free carrier. This recombination process clearly comprises charge carriers that are not created by the same photon which is referred to as non-geminate recombination. This type of recombination is strongly dependent on the population of other charge carriers and follows bimolecular kinetics.
Geminate recombination losses can be an indication of poor blend morphology with domain sizes larger than the exciton diffusion length. Another reason could be that the energetic offsets between donor and acceptor HOMO and LUMO levels at the D/A interface are too small such that the dissociation of the CT complex into free charge carriers is not energetically favourable.

Yet there have been reports on organic solar cells that convert absorbed photons into free electrons with almost 100% efficiency [12]. This means that geminate recombination can be completely overcome by careful choice of materials and processing conditions. Non-geminate recombination however will occur in every OPV system and can greatly limit the photocurrent and the solar cell efficiency. Insight in these recombination processes can therefore provide a guideline for further optimization of OSC materials and processing techniques to increase the solar cell efficiency.
In this thesis no actual OPV devices are studied, only thin films of OSC materials. Therefore all generated charges eventually recombine. By modelling the TR-PIA data, it is possible to estimate the polaron lifetime and to assess the (dominant) recombination mechanism. Recombination in actual OSC's can however be more complicated than the simple monomolecular and bimolecular models discussed here. Other mechanisms such as trap-assisted recombination may occur or it could be necessary to consider combinations of different models [12].

4.2 Monomolecular model

In the monomolecular model, the recombination rate only depends on the properties of the geminate polaron pair and is independent of the population of other charge carriers. Assuming infinite availability of states for polaron creation, i.e. no depletion, the rate equation is given by

$$\frac{dn}{dt} = AI(t) - Wn \tag{4.1}$$

where W is the monomolecular recombination constant and $AI(t)$ is the charge carrier density generated at a certain time consisting of the generation efficiency factor A and the time-dependent laser intensity $I(t)$.
In TR-PIA the laser intensity is on/off modulated at a fixed frequency. In the on-period $I(t) = I$ and the rise in PIA signal corresponds to the generation of positive polarons. When the laser is switched off, $I(t) = 0$ and the PIA signal decays again due to recombination of the polarons. Not all polarons may have recombined at the end of the off-period. As such the system will evolve to a steady-state situation where the PIA signal oscillates with a fixed amplitude determined by the number of polarons n_{min} remaining at the end of the off-period and the maximum number of photogenerated polarons n_{max} at the end of the on-period. Note that we cannot detect the background arising from the remaining polarons at the end of the off-period because only the AC component of the TR-PIA signal is registered. When ground state depletion is neglected, the on- and off-period of the PIA signal are described by exponential functions with rise respectively decay constant equal to W:

$$\begin{aligned} \text{ON} \Rightarrow n(t) &= \frac{AI}{W}\left(1 - e^{Wt}\right) + n_{min}e^{-Wt} \\ \text{OFF} \Rightarrow n(t) &= n_{max}e^{-Wt} \end{aligned} \tag{4.2}$$

where n_{max} and n_{min} depend on the half period of modulation T according to:

$$\begin{aligned} n_{max} &= \frac{AI}{W}\frac{1}{1 + e^{-WT}} \\ n_{min} &= n_{max}e^{-WT}. \end{aligned}$$

It is clear that the amplitude of the signal, $n_{max} - n_{min}$, will grow linearly with the laser power. A least-squares fit corresponding to this simple monomolecular model is fully characterised by three parameters: the recombination constant W, the generation term AI and an adjustable

background parameter to compensate for small baseline deviations. The lifetime of the polarons is then given by $\tau = 1/W$. Figure 4.1 shows an example of a simulated PIA signal obtained within the monomolecular model with $W = 15\,\mathrm{ms}^{-1}$, $AI = 150$, zero background and a modulation frequency of 384 Hz. An important feature of the monomolecular model is the symmetrical shape of the rise and decay period, i.e. when the signal is inverted and translated over the half period of modulation the same result is obtained. This property is easily verified for an experimentally observed PIA signal to establish whether it can be described with the monomolecular model.

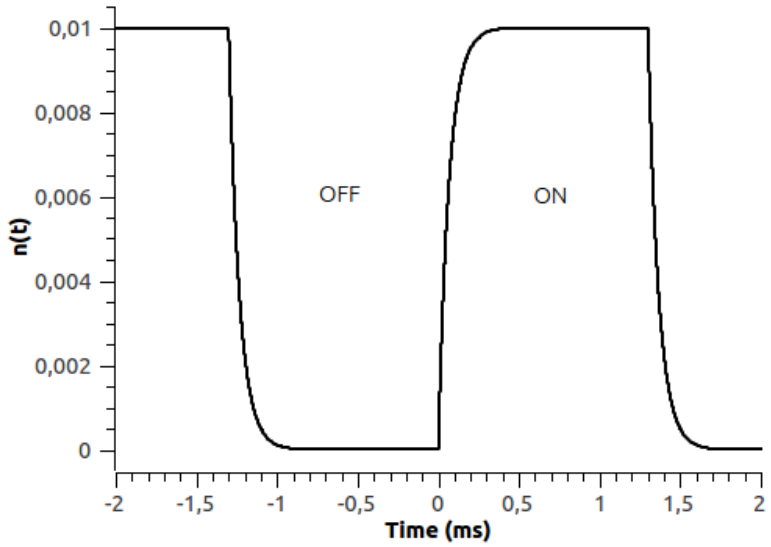

Figure 4.1: Example of a simulated PIA signal obtained within the monomolecular model without depletion with $W = 15\,\mathrm{ms}^{-1}$, $AI = 150$, zero background and a modulation frequency of 384 Hz.

Incorporating the effect of ground state depletion, the rate equation is modified to

$$\frac{dn}{dt} = AI(t)[n_{tot} - n] - Wn \tag{4.3}$$

where n_{tot} denotes the total number of available polarons. Note that the dimension and meaning of A has changed with respect to the rate equation (4.1). Yet, both models can be easily compared by replacing AI with AIn_{tot} in the equations for the monomolecular model. The exponential decay of the PIA signal in the off-period is still described by equation (4.2) but the rise of the polaron concentration in the on-period is now given by

$$n(t) = \frac{AIn_{tot}}{AI + W}\left[1 - e^{-(W+AI)t}\right] + n_{min}e^{-(W+AI)t}.$$

It is clear that the time constant of the exponential rise in the on-period now has become a function of the laser power I. Hence on- and off-signal will no longer be symmetric as before. The effect of saturation due to ground state depletion is clearly demonstrated in the new expression for n_{max}:

$$n_{max} = \frac{AIn_{tot}}{AI + W}\left[\frac{1 - e^{-(W+AI)T}}{1 - e^{-(2W+AI)T}}\right].$$

When the laser power is raised such that $AI \gg W$, n_{max} approximates the total number of available polarons n_{tot}. Hence the amplitude of the PIA signal does no longer depend linearly on the laser power as before. Instead it will saturate for high laser power. To fit

this monomolecular model including ground state depletion, one additional parameter (n_{tot}) is required.
Whether ground state depletion plays an important role or not can be established by measuring the PIA signal for variable laser power. From the power dependence of the signal amplitude and the time constant of the exponential rise during the on-period one can easily distinguish between these two versions of the monomolecular model. Figure 4.2 compares the power dependence of the signal amplitude $n_{max} - n_{min}$ obtained within the two monomolecular models for $W = 15\,\mathrm{ms}^{-1}$ and a modulation frequency of 384 Hz. We chose $n_{tot} = 1$ in the model with depletion such that the generation parameter AI is the same in both models. For small values of the generation parameter we have $n_{max} \ll n_{tot}$ such that depletion effects are negligible and both monomolecular models predict essentially the same behaviour. Yet, for higher laser powers clear differences between the two models start to appear.

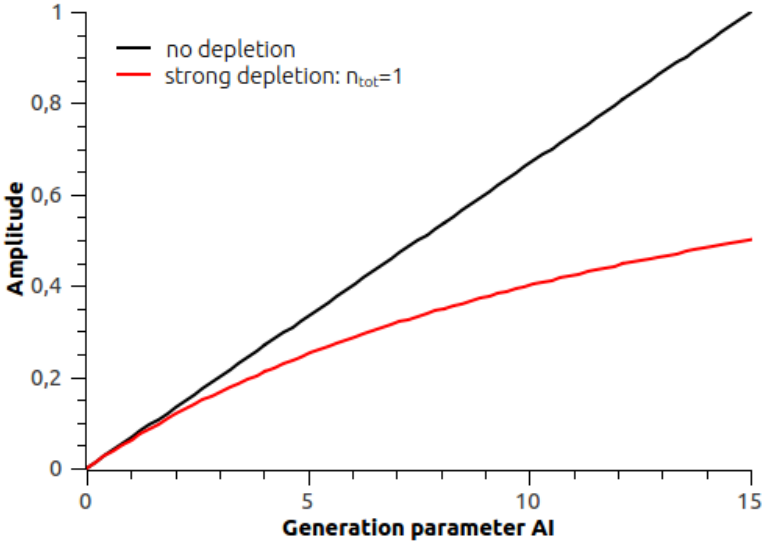

Figure 4.2: Comparison of the power dependence of the signal amplitude obtained within the monomolecular model with and without depletion for $W = 15\,\mathrm{ms}^{-1}$ and a modulation frequency of 384 Hz. In the monomolecular model with depletion we chose $n_{tot} = 1$.

4.3 Bimolecular model

The bimolecular model describes non-geminate recombination, i.e. recombination of charge carriers that originate from different photogenerated excitons. Therefore the recombination rate will depend on the concentration of oppositely charged carriers. As charges are created in pairs, the electron and hole concentrations are equal and the recombination rate will be given by Wn. Assuming infinite availability of states for polaron creation, the resulting rate equation is equal to

$$\frac{dn}{dt} = AI(t) - Wn^2. \tag{4.4}$$

It is important to note that the shape of the signal will only depend on the product of W and AI. Let's take $W' = \alpha W$ and $AI' = AI/\alpha$ such that $WAI = W'AI'$ then we have:

$$\frac{dn}{dt} = \frac{AI}{\alpha} - \alpha W n^2 \Rightarrow \frac{d(\alpha n)}{dt} = AI(t) - W(\alpha n)^2,$$

which corresponds to a rescaling of n with a factor α that doesn't change the shape of the signal. However, when modelling an experimental TR-PIA signal, W and AI will be independent

parameters because both shape and amplitude of the PIA need to be fit. Equation 4.4 is a non-linear equation but it can be solved analytically. The resulting time dependence of the polaron concentration during the on- and off-period of the laser is given by:

$$\text{ON} \Rightarrow n(t) = n_{sat}\frac{\tanh(\sqrt{AIW}t) + (n_{min}/n_{sat})}{1 + (n_{min}/n_{sat})\tanh(\sqrt{AIW}t)} \tag{4.5}$$

$$\text{OFF} \Rightarrow n(t) = \frac{n_{max}}{1 + n_{max}Wt} \tag{4.6}$$

with $n_{sat} = \sqrt{AI/W}$ the saturation polaron concentration obtained from equation (4.4) with $dn/dt = 0$ and $I(t) = I$. Note that this saturation concentration increases as $\sqrt{I}$ with laser power in contrast to the linear laser power dependence of the signal amplitude obtained for the simple monomolecular model. For the bimolecular model, no closed expression exists for the steady-state value of n_{max} and n_{min}. Hence n_{max} and n_{min} need to be determined iteratively from equations (4.5) and (4.6). Clearly, the bimolecular model exhibits a distinct asymmetry between the functional form of the on- and off-period: the decay in the off-period is now governed by a kind of power-law dependence whereas the rise of the PIA signal in the on-period is still built up from exponential functions via the hyperbolic tangents. There are again three fitting parameters required: the bimolecular recombination constant W, the generation term AI and an adjustable background parameter. Figure 4.3 shows an example of a simulated PIA signal obtained within the bimolecular model with $W = 25\,\text{ms}^{-1}$, $AI = 250$, zero background and a modulation frequency of 384 Hz. Note that $n_{min} \neq 0$ in this case.

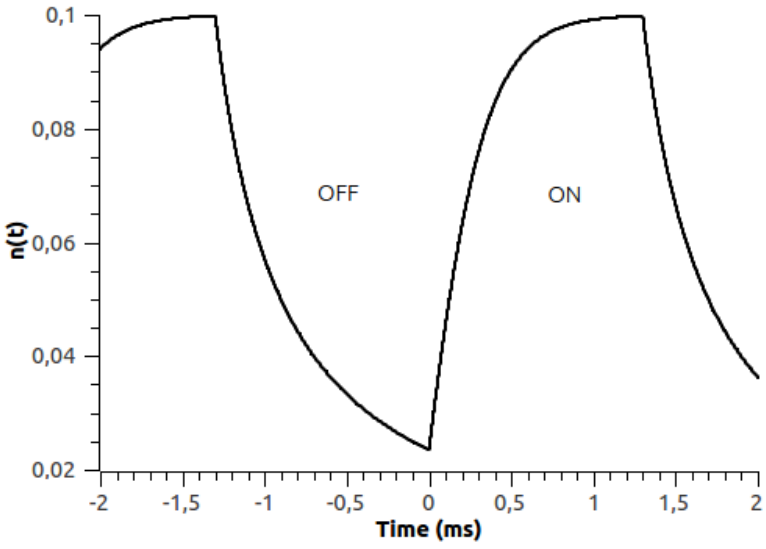

Figure 4.3: Example of a simulated PIA signal obtained within the bimolecular model without depletion with $W = 25\,\text{ms}^{-1}$, $AI = 250$, zero background and a modulation frequency of 384 Hz.

The polaron lifetime is given by the inverse of the recombination rate. In the bimolecular model this yields $\tau = 1/Wn$. Yet, the proportionality factor between the PIA intensity and the actual polaron concentration n is not known such that we cannot derive n from the experimentally observed signal amplitude. However, in our experiments the laser modulation was typically much slower than the response time of the PIA signal. As such we can assume that $n_{max} \approx n_{sat}$ at the end of the on-period. Therefore a reasonable approximation for the polaron lifetime is given by $\tau = 1/Wn_{sat} = 1/\sqrt{AIW}$.

Because the solution of equation 4.4 was already implemented in a fitting procedure by Nevil [10] we will omit the full derivation of the above expressions. Instead, we will explicitly derive an extension to the model from [10] by including the effect of ground state depletion which is calculated in a similar fashion. When ground state depletion is added to the bimolecular model, the rate equation for the on-period becomes

$$\frac{dn}{dt} = AI\,(n_{tot} - n) - Wn^2. \tag{4.7}$$

This non-linear differential equation is similar to the Riccati equation

$$\frac{dy}{dt} + y^2 + f(y)y = -g(x),$$

which can be solved by rewriting the equation in terms of the variable $z = \exp(\int dxy)$:

$$\Rightarrow \begin{cases} y = \frac{1}{z}\frac{dz}{dx} \\ \frac{dy}{dz} = \frac{1}{z}\frac{d^2z}{dx^2} - y^2 \end{cases}$$

The result is a linear differential equation in the variable z:

$$\frac{1}{z}\frac{d^2z}{dx^2} + f(x)\frac{1}{z}\frac{dz}{dx} = -g(x).$$

By applying this technique on equation 4.7 with $y = Wn$ we find

$$\begin{aligned} \frac{dy}{dt} + y^2 + AIy &= AIWn_{tot} \\ \Rightarrow \frac{d^2z}{dx^2} + AI\frac{dz}{dx} - AIWn_{tot}z &= 0. \end{aligned}$$

The solutions of the linear equation in z are of the form $z(t) = C_1\exp(\lambda_+ t) + C_2\exp(\lambda_- t)$. Hence we have:

$$y(t) = \frac{C_1\lambda_+ e^{\lambda_+ t} + C_2\lambda_- e^{\lambda_- t}}{C_1 e^{\lambda_+ t} + C_2 e^{\lambda_- t}} \quad \text{with} \quad \lambda_\pm = -\frac{AI}{2}\left(1 \mp \sqrt{1 + \frac{4W}{AI}n_{tot}}\right). \tag{4.8}$$

In order to simplify the notations we define $\kappa = \sqrt{1 + \frac{4W}{AI}n_{tot}}$. The solution $y(t)$ needs to satisfy the initial condition $y(0) = Wn_{min}$ which leads to a restraint on the integration constants C_1 and C_2:

$$\begin{aligned} y(0) = Wn_{min} \Rightarrow \frac{2n_{min}W}{AI} &= \frac{C_1(-1+\kappa) + C_2(-1-\kappa)}{C_1 + C_2} \\ \Rightarrow \frac{C_2}{C_1} &= \frac{\kappa - 1 - 2n_{min}W/AI}{\kappa + 1 + 2n_{min}W/AI}. \end{aligned}$$

Substituting this result in 4.8 we arrive at:

$$\begin{aligned} y(t) &= \frac{AI}{2}\frac{(\kappa + 1 + \frac{2n_{min}W}{AI})(-1+\kappa)e^{\lambda_+ t} + (\kappa - 1 - \frac{2n_{min}W}{AI})(-1-\kappa)e^{\lambda_- t}}{(\kappa + 1 + \frac{2n_{min}W}{AI})e^{\lambda_+ t} + (\kappa - 1 - \frac{2n_{min}W}{AI})e^{\lambda_- t}} \\ &= \frac{AI}{2}\frac{(\kappa^2 - 1 - \frac{2n_{min}W}{AI})(e^{\lambda_+ t} - e^{\lambda_- t}) + \frac{2n_{min}W}{AI}\kappa(e^{\lambda_+ t} + e^{\lambda_- t})}{\kappa(e^{\lambda_+ t} + e^{\lambda_- t}) + (1 + \frac{2n_{min}W}{AI})(e^{\lambda_+ t} - e^{\lambda_- t})}. \end{aligned}$$

Making use of $\kappa^2 - 1 = 4Wn_{tot}/AI$, we finally get the following expression for the time dependence of the polaron concentration n(t):

$$n(t) = \frac{y(t)}{W} = \frac{(2n_{tot} - n_{min}) \tanh\left(\frac{AI}{2}\kappa t\right) + n_{min}\kappa}{\kappa + (1 + \frac{2n_{min}}{AI}) \tanh\left(\frac{AI}{2}\kappa t\right)}. \tag{4.9}$$

The off-period will still be described by equation 4.6. The fitting parameters in this case are W, AI, n_{tot} and a background parameter. The polaron lifetime can again be approximated by $\tau = 1/Wn_{sat}$ where the saturation concentration is now given by $n_{sat} = AI(\kappa - 1)/2W$.
We remark that in the limit $n_{tot} \to \infty$ the argument of the hyperbolic tangents in equation (4.9) indeed reduces to what we found earlier for the bimolecular model without depletion:

$$\tanh\left(\frac{AI}{2}\kappa t\right) \approx \tanh\left(\frac{AI}{2}\sqrt{\frac{4W}{AI}n_{tot}}t\right) = \tanh\left(\sqrt{AIn_{tot}W}t\right).$$

Note that for correct comparison of the bimolecular models with and without depletion the generation term AI in equation (4.4) needs to be replaced by AIn_{tot}. Also for the saturation concentration the correct asymptotic behaviour is obtained when $n_{tot} \to \infty$:

$$n_{sat} = \frac{AI}{2W}(\kappa - 1) \approx \frac{AI}{2W}\sqrt{\frac{4W}{AI}n_{tot}} = \sqrt{\frac{AIn_{tot}}{W}}.$$

Due to the higher complexity of the formulas, a comparison between the bimolecular model with and without ground state depletion is not as straightforward as in the monomolecular case. Again the difference between the two models will be most apparent when the PIA of a system is measured for variable laser power. Fitting the experimental data by keeping all parameters fixed except AI can then provide a good indication of the applicability of the model to the system under study.

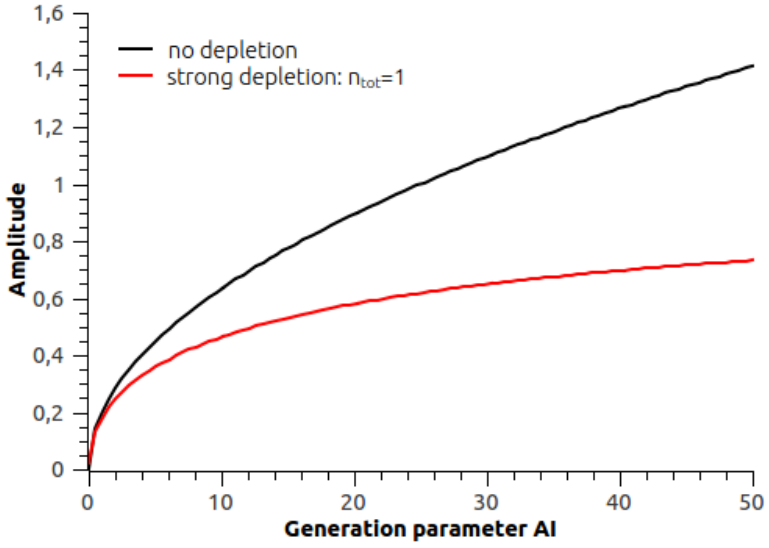

Figure 4.4: Comparison of the power dependence of the signal amplitude obtained within the bimolecular model with and without depletion for $W = 25\,\mathrm{ms}^{-1}$ and a modulation frequency of 384 Hz. In the bimolecular model with depletion we chose $n_{tot} = 1$.

Because no analytical expression exists for n_{max} and n_{min} in the bimolecular model, we cannot easily plot the signal amplitude in function of the generation parameter AI. Yet, when the modulation is slow as compared to the response of the PIA signal we can approximate n_{max} by n_{sat} such that the amplitude of the signal is given by $n_{sat} - n_{min} = n_{sat}[1 - \exp(-WT)]$. In

figure 4.4 the power dependence of this expression for the signal amplitude is compared for the two bimolecular models with $W = 25\,\mathrm{ms}^{-1}$ and a modulation frequency of 384 Hz. Again we chose $n_{tot} = 1$ in the model with depletion such that the generation parameter AI is the same in both models. As long as $n_{max} \ll n_{tot}$ for small values of the generation parameter both models yield the same signal amplitude. For higher laser powers the $\sim \sqrt{I}$ dependence of the amplitude predicted by the bimolecular model without depletion becomes apparent. Yet, in the model with depletion saturation effects start to limit the increase of the signal amplitude.

4.4 Conclusion

In this chapter we introduced two models to describe experimental TR-PIA data: the mono- and bimolecular model corresponding respectively to geminate and non-geminate recombination of charge carriers. Both models were also extended by including the effect of ground state depletion. We conclude by summarising the main differences between the models. A first characteristic that allows to distinguish between the different models was the asymmetry of the shape of the rise and decay period. The monomolecular model without depletion predicts a perfectly symmetric exponential rise and decay of the polaron concentration, i.e. when the signal is inverted and translated over half the modulation period exactly the same result is obtained. When depletion is included in the monomolecular model, the on- and off-period are still described by exponential functions yet with different time-constants. Hence a small asymmetry arises between rise and decay but the functional form remains the same. In the bimolecular model this is no longer true and a distinct asymmetry in shape and functional behaviour of the rise and decay kinetics can be observed. Another important distinction between the different models involves the predicted laser power dependence of the signal amplitude. In the monomolecular model without depletion the amplitude increases linearly with laser power whereas the bimolecular model without depletion predicts a $\sqrt{I}$ dependence. When depletion is taken into account, saturation effects start to play a role and a significantly slower increase of the signal amplitude is observed for both models. As such measuring the TR-PIA for variable laser power and examining whether the models reproduce the observed power dependence of the signal amplitude is a viable approach to determine which model is most suited to describe the polaron generation and recombination dynamics of the system.

Chapter 5

PIA modelling of pure TPA-DTTzTz-diCN and blends with PC70BM

In this chapter the results of our study of the novel donor material TPA-DTTzTz-diCN in combination with the standard acceptor PC70BM are presented. The first two parts treat the general optical characterisation of the pristine donor material and a 1:3 TPA-DTTzTz-diCN:PC70BM blend by means of UV-VIS absorption and PL spectroscopy on spin coated films. A first indication for successful charge transfer was obtained from the observed quenching of donor PL in the blend thereby revealing a CT-band in the blend PL. PIA measurements were performed to confirm the CT and to further investigate the photogenerated charge carriers in the blend. Yet, also in the pure TPA-DTTzTz-diCN sample a surprisingly large PIA signal was obtained. This was ascribed to long-living triplet states in the donor material. Both wavelength-dependent PIA and TR-PIA were performed to characterise the excited species spectrally and kinetically. Of particular interest was the modelling of the TR-PIA data to determine the physical mechanism governing the recombination kinetics. To that end the validity of the models was tested by measuring the TR-PIA for variable laser power and fitting the experimental data by keeping all parameters fixed except the generation rate AI which is proportional to the laser power. The results of the wavelength-dependent PIA are presented in the third part of this chapter, the following sections treat the modelling of TR-PIA data of both pure and blend films.

5.1 Optical absorption

Figure 5.1 shows the UV-VIS absorption spectra of the pristine TPA-DTTzTz-diCN film and the 1:3 TPA-DTTzTz-diCN:PC70BM blend. The spectra were corrected for absorption by the glass substrate. Note that the absorbance depends on the film thickness which was not measured for these samples. As such our main interest will be the difference in shape of the absorption spectra rather than the relative intensities.
The optical bandgap of TPA-DTTzTz-diCN can be determined from the low-energy onset of the absorption band. The edge of the absorption band at 580 nm yields a bandgap of 2.14 eV which is much smaller than the bandgap of 2.54 eV ($\sim$ 488 nm) determined earlier by cyclic voltametry [8] (figure 3.5). Hence the HOMO and LUMO levels in the solid state appear to be markedly different from those obtained from solutions. The spectrum of the pure TPA-DTTzTz-diCN film exhibits an absorption peak at 480 nm. In the blend spectrum this maximum is slightly blue shifted to 475 nm due to the presence of PC70BM. An additional peak is observed in the blend spectrum at 378 nm which was not present in the spectrum of the pristine donor film. This peak and the accompanying short-wavelength shoulder are attributed to absorption

by the PC70BM. Hence all features in the blend absorption spectrum can be described by a superposition of the spectra of the constituent materials and no direct CT absorption is observed.

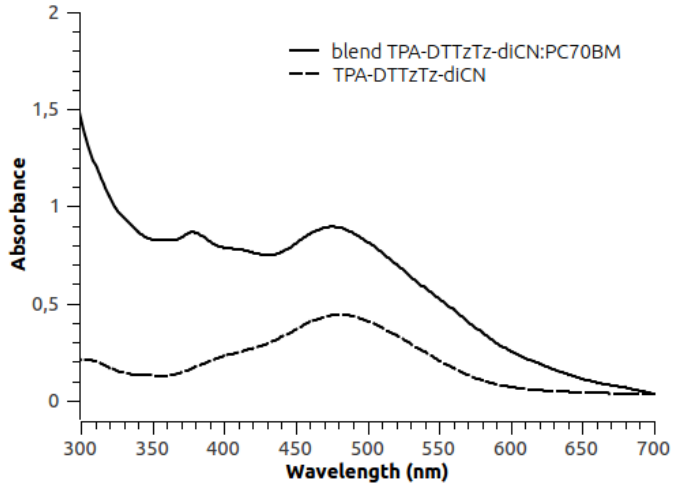

Figure 5.1: UV-VIS absorption spectra of the pure TPA-DTTzTz-diCN film and the 1:3 TPA-DTTzTz-diCN:PC70BM blend.

5.2 PL quenching

The normalised PL spectra of the pure TPA-DTTzTz-diCN film and the 1:3 TPA-DTTzTz-diCN:PC70BM blend are shown in figure 5.2. The samples were excited by a diode laser at 447 nm which lies within the absorption band of both pure and blend films. The spectra are corrected for dark current measured by the detector by subtracting a background spectrum. Also the wavelength dependent sensitivity of the set-up including the effect of the detector and the used filters is taken into account by dividing the spectra by the correction factor defined in section 3.3.2. Before normalisation, the PL intensity of the pure film was a factor 25 larger than the PL of the blend. Hence very strong PL quenching was observed in this donor-acceptor combination.

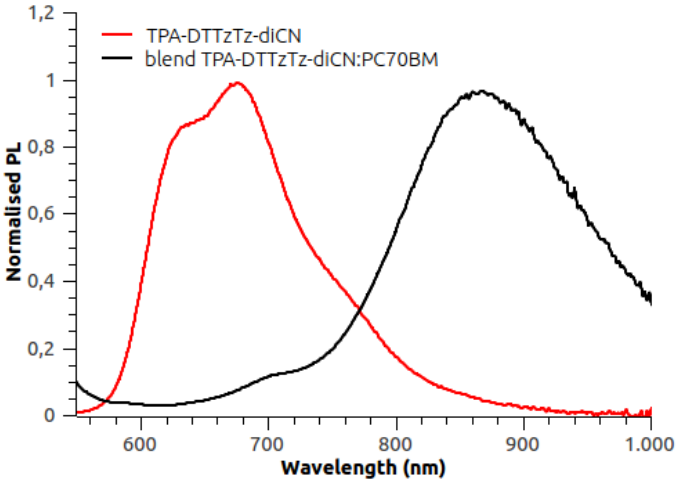

Figure 5.2: Normalised PL spectra of the pure TPA-DTTzTz-diCN film and the 1:3 TPA-DTTzTz-diCN:PC70BM blend.

Two peaks are observed at 635 nm and 677 nm in the PL spectrum of the pure TPA-DTTzTz-diCN film revealing the vibrational structure of the molecule. In the blend the donor PL is almost completely suppressed which suggests a very efficient charge transfer in this donor-acceptor system. Moreover the blend spectrum exhibits a PL band that is clearly distinct from the donor PL. As fullerene emission is known to be very weak, the observed PL in the blend can be ascribed to CT emission. This CT-band occurs at significantly longer wavelengths than the donor PL with a maximum at 870 nm. This is consistent with the fact that the transition from the CT state to the groundstate will be lower in energy than the transition from donor LUMO to donor HOMO in the case of direct radiative decay of photogenerated excitons in the donor (see figure 3.5). The small peak around 715 nm probably originates from emission by PC70BM. The increase in the PL of the blend at short wavelengths is an artefact caused by scattered laser light that is not completely eliminated by the cut-off filters. In the pure material the PL intensity is a factor 25 larger such that this effect is barely visible in the donor PL spectrum.
The observed PL quenching and the presence of a CT-band in the blend PL spectrum are a first indication of successful charge transfer in the TPA-DTTzTz-diCN:PC70BM system. In order to further investigate the charge carriers created after charge transfer both wavelength-dependent PIA and TR-PIA measurements were performed.

5.3 Triplet and polaron detection by PIA

As discussed before in chapter 3, PIA can be used to detect photogenerated polarons in donor:acceptor blends. Yet, also other excited species such as triplet excitons can be studied with PIA. One way to distinguish between different types of excited species is by comparing the PIA spectra with known polaron bands from the literature. For PC70BM for example, it is known that the small energetic spacing between the excited states of the negative polarons corresponds to IR photon energies far beyond the spectral sensitivity of our experimental set-up. As such the PIA signals can contain no contribution from negative polarons on PC70BM. Yet, for novel OSC materials such as TPA-DTTzTz-diCN no comparison with the literature can be made. Therefore we will rely on a comparison of the PIA in the pristine TPA-DTTzTz-diCN film and the blend with PC70BM to distinguish between excited species that could occur in both samples, such as donor triplets, and polaronic excitations that are restricted to the blend.

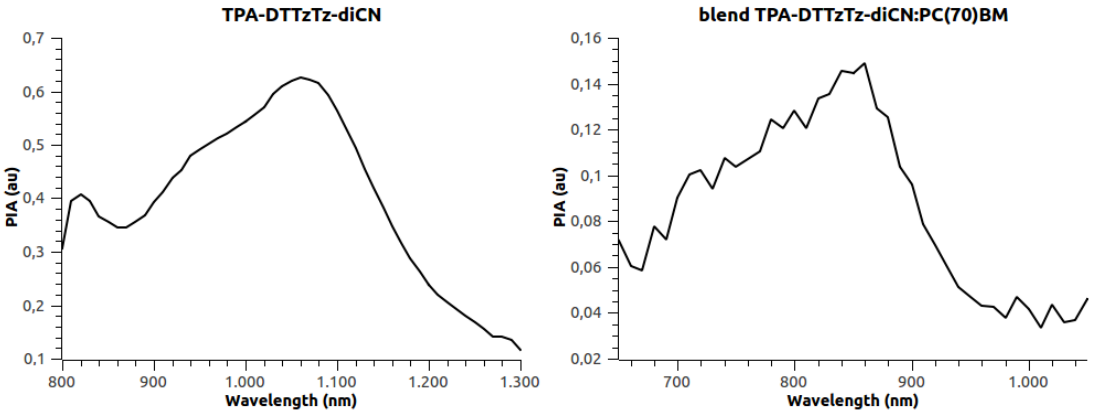

Figure 5.3: PIA spectrum of the pure TPA-DTTzTz-diCN film and the 1:3 TPA-DTTzTz-diCN:PC70BM blend for a modulation frequency of 384 Hz.

The PIA measurements were performed with a Edinburgh Instruments LP920 spectrometer which was originally intended for laser flash photolysis. The sample was excited by means of an on/off modulated 532 nm frequency-doubled Nd:YAG laser. The PIA signal is then obtained

by measuring the changes in absorption of probe light from a halogen lamp by the sample due to the laser excitation. The PIA spectra of the pure TPA-DTTzTz-diCN film and the 1:3 TPA-DTTzTz-diCN:PC70BM blend obtained from wavelength-dependent measurements are shown in figure 5.3. PL contributions are eliminated from the spectra by subtracting a reference measurement without probe. The spectra are also corrected for the wavelength-dependent sensitivity of the set-up including the effect of the detector and the filters. The spectrum of the pure TPA-DTTzTz-diCN film was measured via the lock-in amplifier and with the InGaAs detector to ensure sufficient sensitivity in the NIR. Due to time limitation, the spectrum of the blend was only obtained with the alternative measuring technique described at the end of section 3.3.3. For every wavelength scanned by the monochromator, the time-dependent PIA signal was directly registered on a digital storage oscilloscope by means of an AC Si detector. The spectrum was then obtained by taking the Fourier transform of the time-dependent signals. Indeed, the Fourier component corresponding to the modulation frequency of the laser will yield a PIA intensity equivalent to what we obtain with the lock-in detector. Note that the relative PIA scales obtained with these different measuring techniques do not agree. Yet the ratio of the PIA intensities of the pristine film and the blend could be derived from the time-dependent PIA measurements which were performed under the same circumstances. As such we could multiply the PIA intensity of the blend with the correct scale factor to make the relative PIA scales mutually consistent. As mentioned before, the signal-to-noise ratios achieved with this alternative technique were appreciably lower than in the measurements via the lock-in detector for comparable integration times. This can be easily noticed by comparing the PIA spectra in figure 5.3. However, it should be kept in mind that the signal-to-noise ratio is also reduced by a factor 4.5 because of the lower PIA signal in the blend. The TR-PIA measurements are shown in figure 5.4. These are also corrected for PL by subtracting a reference measurement and the resulting graphs were shifted vertically such that they coincide in zero at the end of the off-period.

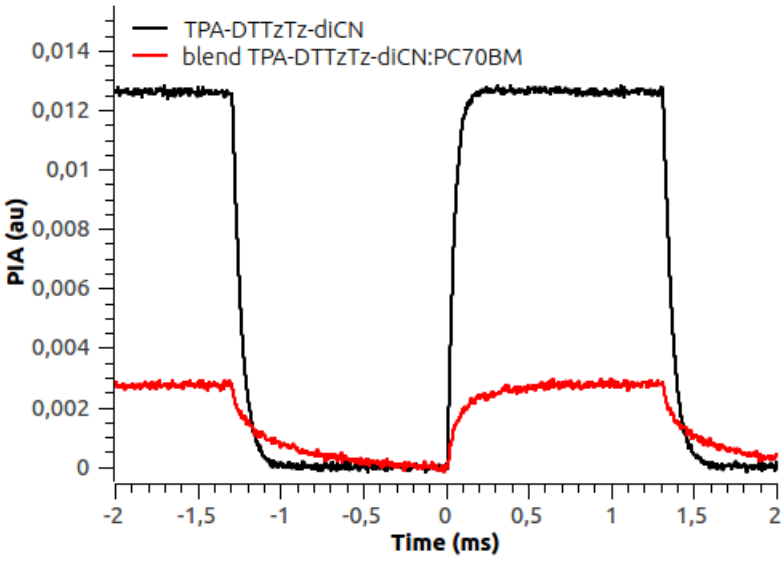

Figure 5.4: TR-PIA of the pure TPA-DTTzTz-diCN film and the 1:3 TPA-DTTzTz-diCN:PC70BM blend for a modulation frequency of 384 Hz and λ_{probe} = 1000 nm respectively λ_{probe} = 870 nm. The probe wavelengths correspond to the maximal PIA signal attainable with the DC Si detector in both samples.

The PIA spectra shown in figure 5.3 are clearly different. The polaron band in the blend extends from roughly 700 nm to 950 nm with a maximum at 860 nm. The PIA band in the pure TPA-DTTzTz-diCN film is found for significantly longer wavelengths with a maximum

at 1060 nm. Also the TR-PIA measurements reveal important differences between the excited species in the pure film and the blend with PC70BM. The decrease in intensity already indicates that the excited species responsible for the large PIA signal in the pure material is severely suppressed in the blend. There is also a significant difference in shape of both rise and decay periods of the TR-PIA of pure film and blend. Especially in the off-period it is clearly seen that the recombination in the blend is governed by a much slower decay rate than in the pure film. A more quantitative analysis of the TR-PIA data will be given in the following sections. There, the models described in chapter 4 will be applied to fit the experimental data in order to determine the underlying recombination mechanisms and the corresponding recombination rates. Yet, from the qualitative observations made above we can already conclude that the PIA signal in the blend and the pure film originate from a different kind of excited species. In the blend the PIA signal can be ascribed to positive polarons on the TPA-DTTzTz-diCN in accordance with the efficient CT in this donor:acceptor combination demonstrated by the PL spectra in the previous section. The large PIA signal in the pure film is attributed to long-lived triplet states in the donor material.

5.4 Modelling of TR-PIA in pure TPA-DTTzTz-diCN films

In chapter 4 two different models describing the rise and decay kinetics of the TR-PIA data were presented: the monomolecular and bimolecular model corresponding respectively to geminate and non-geminate recombination. In addition, an extension to both models was developed by including the effect of ground state depletion. In order to test the applicability of the models to the system under study we decided to measure the TR-PIA for variable laser power and model the experimental data by keeping all parameters fixed except the generation term AI. The TR-PIA measurements on the pure TPA-DTTzTz-diCN sample were performed at a modulation frequency of 1184 Hz to resolve the rise and decay behaviour in more detail than in figure 5.4. The monochromator was tuned to a wavelength $\lambda_{probe} = 1000$ nm corresponding to the maximal PIA signal measured by the DC Si detector. The laser power was varied by means of three different neutral density filters yielding four laser intensities I_0, 0.52 I_0, 0.18 I_0 and 0.09 I_0. The maximum laser power I_0 was fixed at 10 mW on average, i.e. 20 mW in the on-period and 0 mW in the off-period.

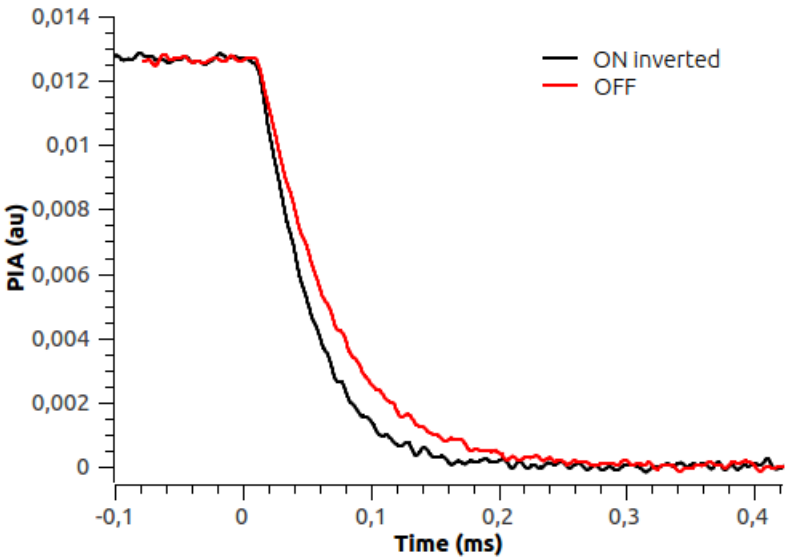

Figure 5.5: Asymmetry in the on- and off-period of the TR-PIA signal of pure TPA-DTTzTz-diCN. The red curve corresponds to the PIA signal translated over half the modulation period.

Figure 5.5 shows the asymmetry between on- and off-period of the TR-PIA signal corresponding to the highest laser power. As the simple monomolecular model without ground state depletion predicts a symmetrical exponential rise and decay of the PIA signal, it will not be suitable to describe the TR-PIA data of the TPA-DTTzTz-diCN film. The models that are able to explain an asymmetry between on- and off-period are the monomolecular model with ground state depletion, for which the exponential rise and decay are now governed by different time-constants, and the two bimolecular models. Yet, the asymmetry between on- and off-period is rather small and the rise and decay curves seem to have a similar shape. Therefore it can be expected that the monomolecular model including depletion will yield a better fit of the experimental results than the bimolecular model which exhibits a significant asymmetry and a clear distinction between the shape of the rise and decay period.
As a first step only the TR-PIA corresponding to the highest laser power was modelled with the monomolecular model with depletion and the bimolecular model without depletion. The best fit of the experimental data was obtained via a standard least-squares fitting procedure in Matlab. The monomolecular model with depletion requires four fitting parameters: the monomolecular recombination rate W, the laser power dependent generation term AI, the total number of available excited states n_{tot} and an adjustable background term to correct for small baseline deviations. For the bimolecular model only three parameters are needed: the bimolecular recombination rate W, AI and a background parameter. The results of the best fits of the TR-PIA data of pure TPA-DTTzTz-diCN with the monomolecular and bimolecular model are shown in figure 5.6. The bimolecular model including ground state depletion was not considered for this system as depletion doesn't severly alter the shape of the bimolecular rise and decay. This will be discussed in more detail in the following section on the modelling of the TR-PIA of the TPA-DTTzTz-diCN:PC70BM blend. As such including depletion wouldn't significantly improve the best fit obtained within the bimolecular model.

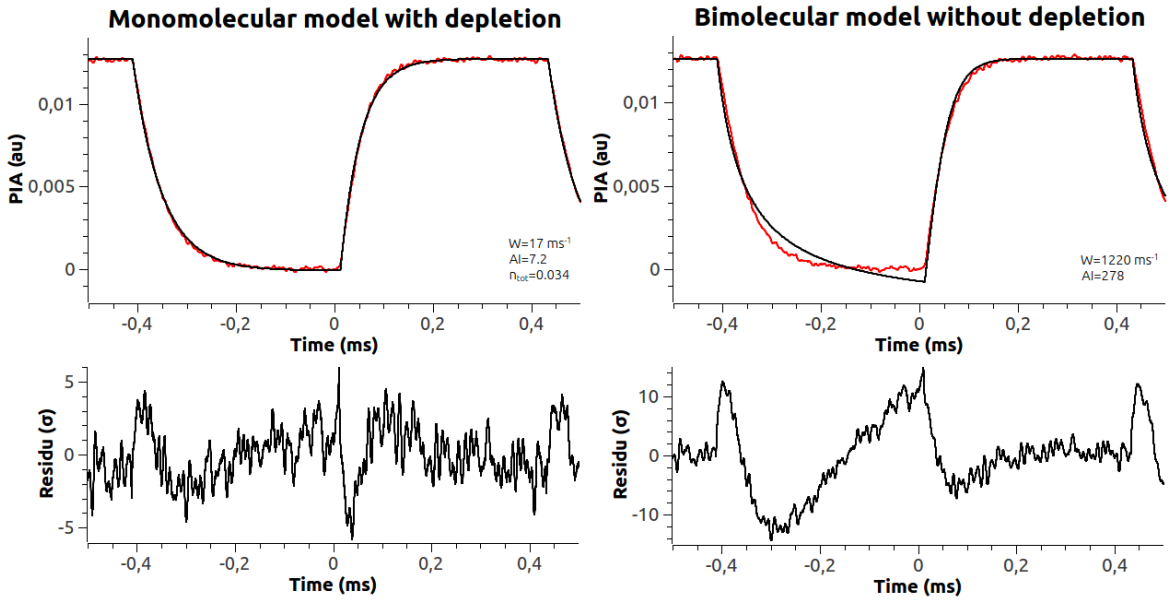

Figure 5.6: Monomolecular model with ground state depletion versus bimolecular model without ground state depletion. Best fits of the experimental TR-PIA data for pure TPA-DTTzTz-diCN corresponding to the highest laser power. Also the residuals are shown to indicate the main deviations between experimental data and model.

From figure 5.6 it is clear that the monomolecular model with ground state depletion describes the TR-PIA data very accurately. In the best fit with the bimolecular model significant deviations from the experimental data can be observed in the off-period. Also in the on-period the bimolecular model yields a faster rise than observed in the PIA signal. In order to further

quantify the agreement between model and experimental data we defined the following figure of merit:

$$\chi^2 = \frac{1}{N}\sum_t \frac{[\text{model}(t) - \text{expdata}(t)]^2}{\sigma^2}, \tag{5.1}$$

with $N = 10000$ the total number of data points. In the case of good agreement between model and experimental data χ^2 should approach one. The standard deviation σ was estimated from the reference signal without probe:

$$\sigma = \sqrt{\frac{1}{N}\sum_t [\text{ref}(t) - \langle \text{ref}(t) \rangle]^2}.$$

This is reasonable as the sample exhibited no significant PL such that the reference signal was constant and the noise level was similar to the noise in the actual PIA measurement. For the bimolecular fit we obtained $\chi^2 = 35.8$. The fit with the monomolecular model with ground state depletion achieved $\chi^2 = 3.4$ which is an improvement by a factor 10. Hence we can conclude that the monomolecular model with ground state depletion succeeds best in capturing the physical mechanism governing triplet generation and recombination in the pristine TPA-DTTzTz-diCN sample. Therefore only this model was used to fit the laser power dependence of the TR-PIA data.

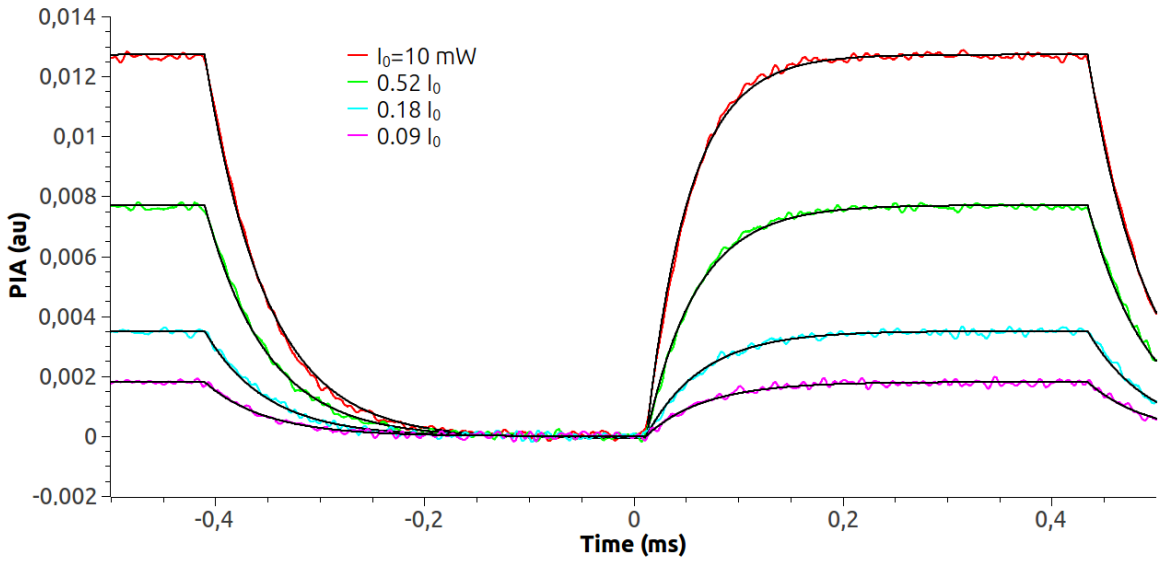

Figure 5.7: Laser power dependence of the TR-PIA of pure TPA-DTTzTz-diCN at $\lambda = 1000\,\text{nm}$ and with a modulation frequency of 1184 Hz. All spectra are modelled with the monomolecular model including ground state depletion with fixed W and n_{tot}. For presentation, the spectra are shifted vertically such that they coincide in zero at the end of the off-period.

Figure 5.7 shows the best fits of the TR-PIA data for variable laser power with the monomolecular model including depletion. The parameters $W = 17\,\text{ms}^{-1}$ and $n_{tot} = 0.034$ were determined from the best fit of the TR-PIA for maximal laser power and were kept fixed for all other laser intensities. Only AI and the background parameter were optimised with the least squares fitting procedure. Clearly the agreement between model and experimental data remains excellent for all laser intensities. Moreover, a linear dependence of the fitting parameter AI on the laser power was found in perfect agreement with our expectations. This is shown in the left panel of figure 5.8.

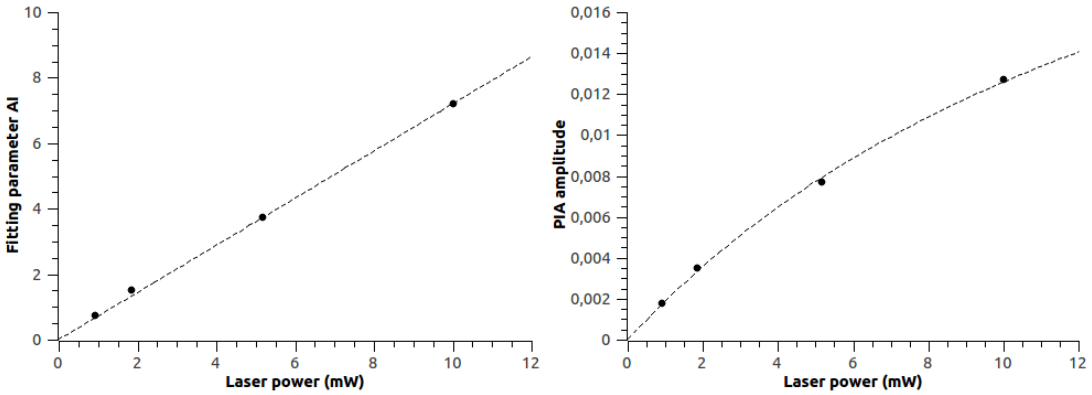

Figure 5.8: Left: Fitting parameter AI in function of the laser power. The dotted line is added to accentuate the linear dependence of AI on the laser power.
Right: Experimental values of the PIA signal amplitude (symbols) versus the amplitude calculated from the model (dotted line).

In order to asses the importance of depletion in the TPA-DTTzTz-diCN sample, we show a plot of the PIA signal amplitude in function of the laser power in the right panel of figure 5.8. A comparison is made between the experimental PIA amplitude calculated from the difference in signal at the end of the on- and the off-period and the theoretical amplitude derived from the model. The analytical expression for the amplitude $n_{max} - n_{min}$ is given in section 4.2. Again good agreement between theory and experiment is established and the importance of depletion in the material for these excitation intensities is demonstrated by the non-linear behaviour of the signal amplitude versus laser power. Indeed, at the highest laser power $n_{max} = 0.013 \approx 0.4 n_{tot}$ indicating that already 40% of the available triplet states are occupied resulting in large depletion effects. Note also that the observed power dependence of the TR-PIA signal amplitude clearly differs from the $\sqrt{I}$ behaviour predicted by the bimolecular model.
We conclude that the generation and recombination kinetics of triplets in the pure TPA-DTTzTz-diCN sample are very well described by the monomolecular model including ground state depletion. Hence geminate recombination is shown to be the dominant recombination mechanism in this system. Finally, the monomolecular recombination rate W obtained from the fitting of the experimental TR-PIA data yields a triplet lifetime of 59 µs.

5.5 Modelling of TR-PIA in blends of TPA-DTTzTz-diCN with PC70BM

The laser power dependent TR-PIA measurements on the TPA-DTTzTz-diCN:PC70BM blend were performed in an analogous fashion as described in the previous section. As the PIA signal in the blend is significantly lower than in the pure TPA-DTTzTz-diCN the signal-to-noise ratios in the measurements on the blend will be greatly reduced. Due to the slower response of the TR-PIA in the blend a lower laser modulation frequency of 137 Hz was used. As such we also obtained higher PIA signals and hence better signal-to-noise ratios than in figure 5.4. The probe wavelength $\lambda = 870$ nm was chosen in accordance with the maximal PIA signal measured by the DC Si detector.
Figure 5.9 shows the asymmetry between on- and off-period of the TR-PIA signal corresponding to the measurement with the highest laser power. Again the symmetric monomolecular model without depletion will fail to describe the experimental data. The asymmetry between rise and decay period is now more prominent than in the pure TPA-DTTzTz-diCN sample.

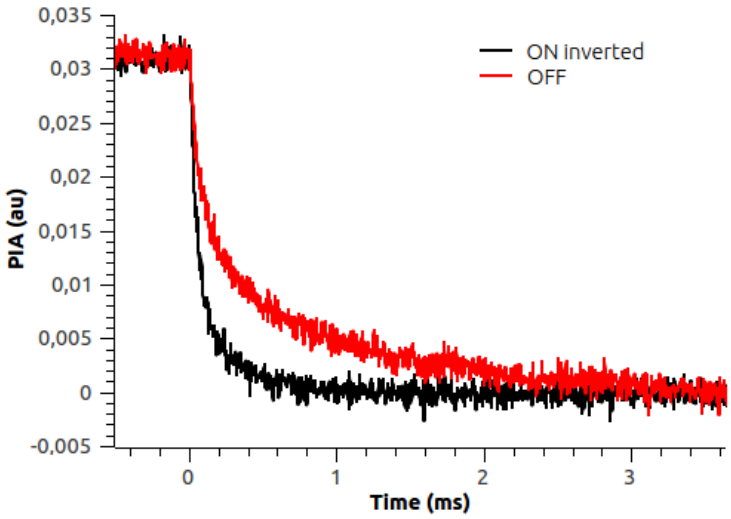

Figure 5.9: Asymmetry of the on- versus the off-period of the TR-PIA signal of a 1:3 blend of TPA-DTTzTz-diCN:PC70BM. The red curve corresponds to the PIA signal translated over half the modulation period.

Initially we only considered the monomolecular model with depletion and the bimolecular model without depletion to fit the TR-PIA data of the blend corresponding to the highest laser power. The sets of fitting parameters are the same as described in the previous section. Figure 5.10 shows the best fit of the experimental data achieved with each of these two models.

Whereas both models seem equally accurate in describing the on-period of the TR-PIA signal, the monomolecular model clearly fails to describe the off-period. For the monomolecular fit with ground state depletion we obtained $\chi^2 = 9.1$. The best fit with the bimolecular model achieved $\chi^2 = 4.5$ which is an improvement by a factor 2. Although the agreement between the bimolecular model and the experimental data is better, there are still significant deviations as seen in figure 5.10.

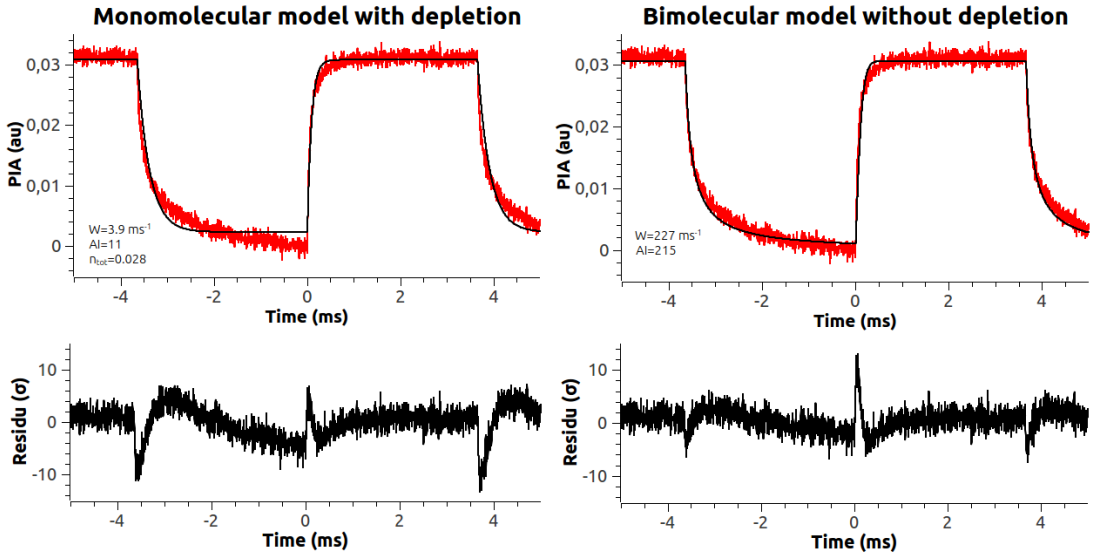

Figure 5.10: Monomolecular model with ground state depletion versus bimolecular model without ground state depletion. Best fits of the experimental TR-PIA data for the TPA-DTTzTz-diCN:PC70BM blend corresponding to the highest laser power. Also the residuals are shown to indicate the main deviations between experimental data and model.

In the bimolecular fit the rise and decay of the modelled PIA signal are still faster than what is observed experimentally. Therefore we hoped to improve the fit by including the effect of ground state depletion in the bimolecular model. Yet, due to the higher complexity of the mathematical form of the extended model, each of the fitting parameters simultaneously affects both shape and amplitude of the PIA signal in a non-trivial way. Hence it is not straightforward to find a minimum from a least squares fitting procedure as the parameters tend to be strongly correlated especially when depletion effects are small. Indeed, in that case n_{tot} will act as a redundant parameter and the overall minimum of the least squares fit will be very hard to find. Therefore we followed a different approach by keeping n_{tot} fixed and performing a least squares fit by optimising all the other parameters. As such we could compare the bimolecular model without depletion with the situation of strong depletion, i.e. n_{tot} of the same order of n_{max}. From the best fits of the experimental data we could then conclude whether the effect of strong depletion improved the agreement with the experimental result or not. A comparison between the best fit obtained with both models for the TR-PIA measurement corresponding to $I_0 = 10\,\mathrm{mW}$ is given in figure 5.11.

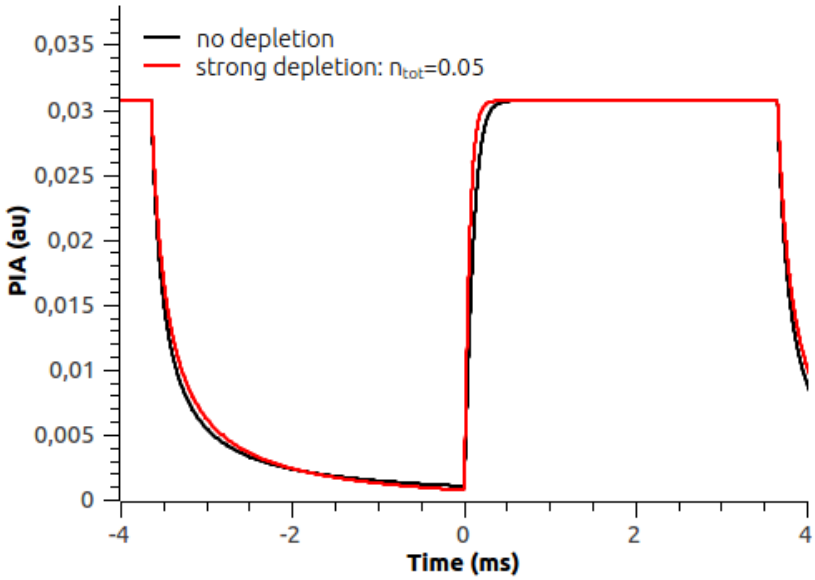

Figure 5.11: Comparison of the best fit of the bimolecular model without depletion and with strong depletion corresponding to the TR-PIA measurement for maximal laser power.

Surprisingly, the shape of the bimolecular model was not significantly altered by including the effect of strong ground state depletion and hence no significant improvement of the agreement between model and experimental data was found. This is confirmed by the $\chi^2 = 4.7$ calculated for the best fit with the depletion model which is comparable to the χ^2 obtained with the simple bimolecular model. Yet, the difference between both models will be most apparent when we compare the fits of the laser power dependent TR-PIA measurements of the blend. Similar to the approach described in the previous section, the bimolecular recombination rate W and the generation term AI were first determined from the best fit of the TR-PIA data corresponding to $I_0 = 10\,\mathrm{mW}$. The fits of the measurements for lower laser power were then obtained by changing the fitting parameter AI proportional to the laser intensity and keeping all parameters fixed except for the background parameter. The results are shown in figure 5.12 and 5.13. We note that also for the monomolecular model with depletion the power dependence of the model and the experimental TR-PIA data was compared. Yet the PIA amplitudes predicted by the model were much larger than what was observed experimentally. Hence the monomolecular model with depletion is not further considered.

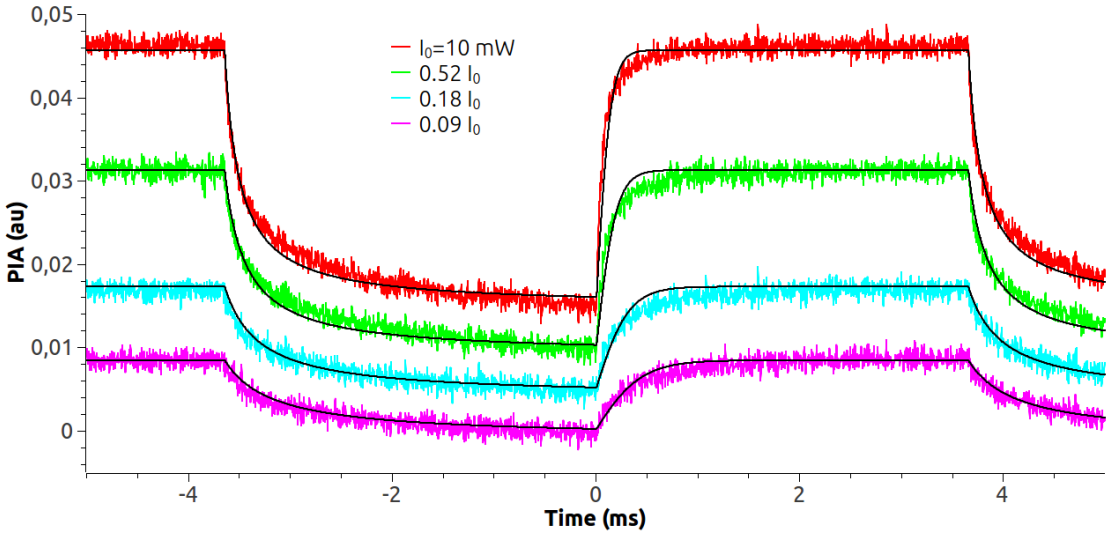

Figure 5.12: Laser power dependence of the TR-PIA of a 1:3 blend of TPA-DTTzTz-diCN:PC70BM at $\lambda = 870\,\text{nm}$ and with a modulation frequency of 137 Hz. All spectra are modelled with the bimolecular model without ground state depletion. The spectra are shifted vertically for clear presentation.

Although the bimolecular model with strong depletion adequately described the TR-PIA data for $I_0 = 10\,\text{mW}$, it does not yield the correct laser power dependence of the experimental data. It is clearly seen in figure 5.13 that both the signal amplitudes and the rise and decay rates predicted by the model differ from the experimental observations. On the other hand the bimolecular model without ground state depletion seems to accurately reproduce the laser power dependence of the TR-PIA measurements. Therefore we conclude that ground state depletion doesn't play an important role in the generation and recombination dynamics of positive polarons in the TPA-DTTzTz-diCN:PC70BM blend at these excitation levels.
Since the bimolecular model without ground state depletion succeeds so well in reproducing the correct laser power dependence found in the experimental data, we conclude that non-geminate recombination governs the recombination kinetics in the blend. The effective polaron lifetime can then be estimated from the fitting parameters according to $\tau = 1/\sqrt{WAI}$. This yields an effective polaron lifetime of 143 µs for the highest excitation intensity. Note that the measurements were performed at liquid nitrogen temperature such that this polaron lifetime is only valid at $T = 77\,\text{K}$.
We end this section with a brief discussion of some alternative explanations for the remaining deviations between the bimolecular model and the experimental data. The bimolecular model as described in chapter 4 relies on a homogeneous illumination of the sample. Yet, the real experimental situation could be different. The effect of inhomogeneous illumination could be implemented in the model by assuming for example a Gaussian laser beam profile and calculating the corresponding distribution of the laser intensity I on the sample. The width of the Gauss can then serve as an additional fitting parameter. However, a more effective approach would probably be to modify the experimental set-up itself thereby ensuring a constant laser intensity throughout the entire area of overlap between laser beam and probe beam. Another effect that is possibly overlooked in the current bimolecular model is a spatial distribution of the bimolecular recombination constant W or the generation efficiency A. Indeed, different donor or acceptor domains in bulk heterojunction blends typically exhibit a variable degree of disorder. Factors like the polaron mobility or the density of traps could be influenced by this local degree of disorder. Hence it is reasonable to assume that also the recombination rate is determined by the local environment of the polaron in the blend. An extension of the current bimolecular

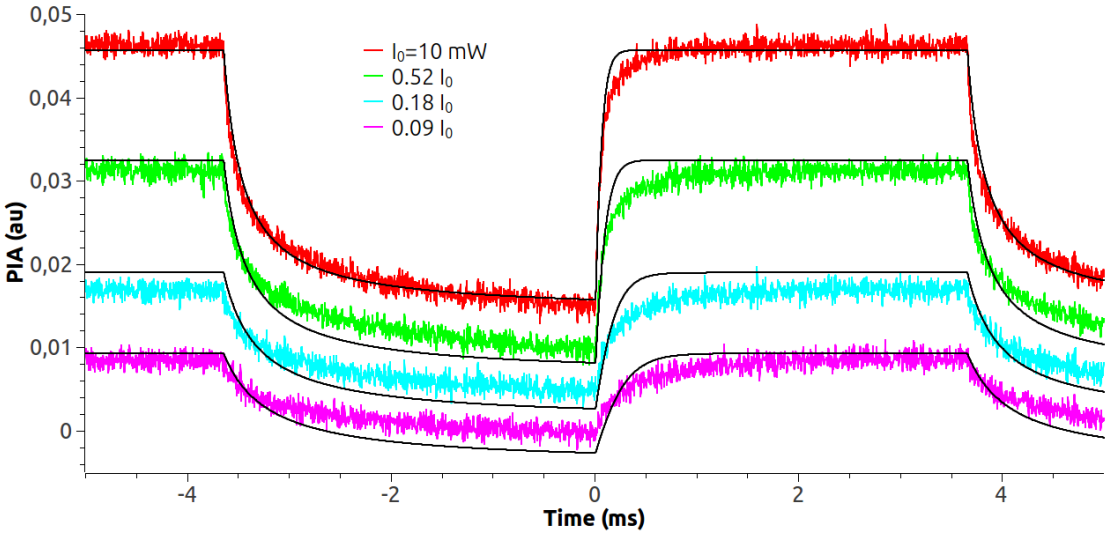

Figure 5.13: Laser power dependence of the TR-PIA of a 1:3 blend of TPA-DTTzTz-diCN:PC70BM at $\lambda = 870\,\text{nm}$ and with a modulation frequency of 137 Hz. All spectra are modelled with the bimolecular model including ground state depletion with fixed $n_{tot} = 0.05$ corresponding to strong depletion. The spectra are shifted vertically for clear presentation.

model to include the effect of a spatial distribution of the parameter W is certainly interesting to gain further insights in the underlying recombination mechanisms in these systems. The effect of inhomogeneous generation or recombination could be incorporated in the model by assuming for example a Gaussian distribution for W or AI and treating the width of the Gauss as an extra fitting parameter. Finally, it is also possible that both geminate and non-geminate recombination of polarons occur in the given donor:acceptor blend. In that case the TR-PIA data should be more accurately described by a combination of the monomolecular and bimolecular model. In any case the above considerations reveal the great complexity associated with charge generation and recombination processes in BHJ active layers. A more fundamental understanding of these processes will require the development of more elaborate models than the simple monomolecular and bimolecular model presented in this thesis.

5.6 Conclusion

In this chapter the results of our study of the novel donor molecule TPA-DTTzTz-diCN in combination with PC70BM were presented. A first indication for successful charge transfer in the TPA-DTTzTz-diCN:PC70BM system was obtained from the quenching of donor PL and the presence of a CT-band in the blend PL spectrum. An additional confirmation of the efficient charge transfer in the blend was obtained from the clear PIA signal which was ascribed to excitations of positive polarons on TPA-DTTzTz-diCN. Modelling of the TR-PIA data revealed that the bimolecular model without ground state depletion was the most suitable to describe the generation and recombination kinetics of the polarons in the blend. Although systematic deviations between the model and the experimental data were found, the bimolecular model adequately reproduced the laser power dependence observed in the experimental TR-PIA data. Therefore we concluded that non-geminate recombination is the dominant recombination mechanism in this system which is essential for good solar cell performance. We also found that the polaron generation was not yet limited by ground state depletion. An estimate of the effective polaron lifetime of 143 µs at $T = 77\,\text{K}$ was obtained from the fitting parameters for the highest laser excitation.

Also for the pristine TPA-DTTzTz-diCN film a surprisingly large PIA signal was obtained. The PIA spectrum and the time-dependent PIA signals were clearly distinct from those observed in the blend and were ascribed to long-lived triplet states in the donor. Excellent agreement between the monomolecular model with depletion and the TR-PIA data was found. Also the laser power dependence of the experimental data was exactly reproduced by the model. From the fitting parameters we derived a triplet lifetime of 59 µs at $T = 77\,\mathrm{K}$.

Chapter 6

Charge transfer in blends of novel DTTzTz acceptors with MDMO-PPV/P3HT

The development of alternative acceptor materials is an important topic in current OPV research motivated by the high cost, poor absorption properties and limited chemical versatility of the widely used fullerene acceptors. In this chapter the results of our study of two recently synthesised small molecule acceptors, CN-DTTzTz-CN and diCN-DTTzTz-diCN, are presented. Efficient charge transfer in MDMO-PPV:CN-DTTzTz-CN blends was already demonstrated by Nevil et al. [11]. In solar cells based on this donor:acceptor combination an open circuit voltage of $V_{oc} = 1.39\,\mathrm{V}$ was obtained which is much higher than in traditional polymer:fullerene devices. Yet the overall photovoltaic performance was poor resulting in a maximum power conversion efficiency of only 0.1% [11]. The diCN-DTTzTz-diCN molecule was selected for study in this thesis as it exhibits slightly lower LUMO and HOMO levels than CN-DTTzTz-CN corresponding to an increased acceptor strength, i.e. a higher driving force for charge transfer at the D/A interface, which could result in improved device performance. At the same time the effective bandgap in blends with MDMO-PPV will remain large enough to yield high V_{oc} solar cells. Apart from the comparison of the DTTzTz acceptors in blends with MDMO-PPV, we also investigated the trend in CT efficiency when replacing MDMO-PPV by the low-bandgap polymer P3HT.
The efficiency of CT in blends of the DTTzTz acceptors with the standard donor polymers MDMO-PPV and P3HT was studied by means of UV-VIS absorption and PL spectroscopy on spin coated films. Also wavelength-dependent PIA and TR-PIA measurements were performed to study polarons formed in the blend after successful CT. Yet, similar to the case of the TPA-DTTzTz-diCN donor material discussed in the previous chapter, a large PIA signal was obtained for the pure films of the DTTzTz acceptors. This is again ascribed to long-living triplet states.

6.1 Optical absorption

All UV-VIS absorption spectra discussed in this section were measured with a Varian Cary E5 spectrophotometer in double beam mode and were corrected for absorption by the glass substrate. Again we note that the absorbance depends on the thickness of the spin coated films which was not measured in our experiments. Therefore the main interest of our analysis of the absorption spectra will be the shape and position of the absorption peaks rather than the relative intensities of the spectra corresponding to different samples.

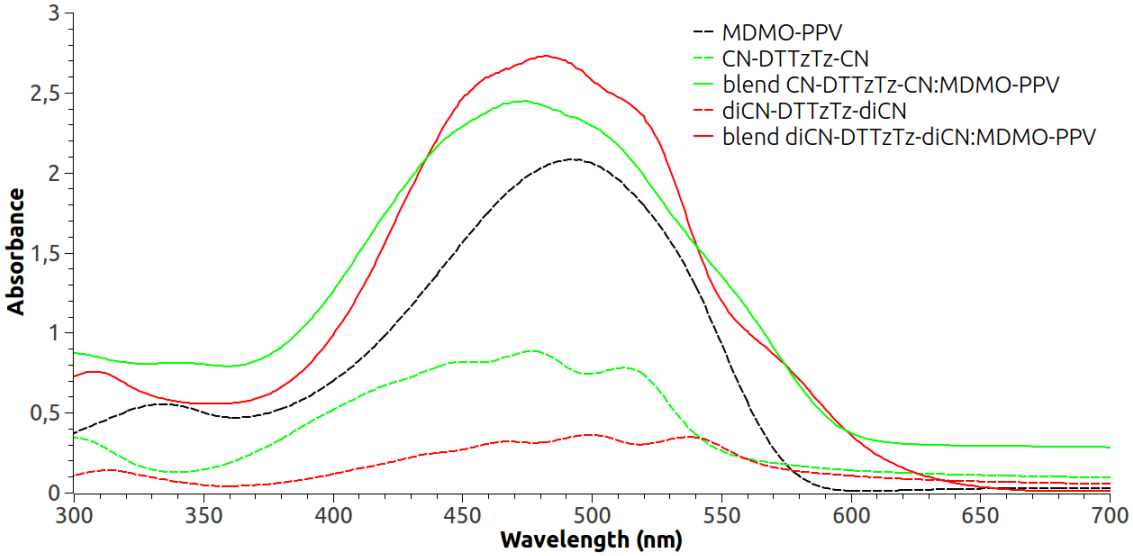

Figure 6.1: UV-VIS absorption spectra of MDMO-PPV, CN-DTTzTz-CN, diCN-DTTzTz-diCN and the 1:1 blends of MDMO-PPV with the DTTzTz acceptors. Dotted lines represent the pristine materials, solid lines the blends.

Figure 6.1 shows the UV-VIS absorption spectra of the pristine MDMO-PPV, CN-DTTzTz-CN, diCN-DTTzTz-diCN film and the 1:1 blends of MDMO-PPV with the DTTzTz acceptors. The absorption bands of the DTTzTz acceptors are somewhat blue shifted with respect to the absorption band of MDMO-PPV in accordance with the slightly larger bandgap of the TzTz materials (figure 3.5). Still there is a large overlap between the absorption bands of donor and acceptor materials.

The vibrational structure of the DTTzTz molecules is clearly resolved in the absorption spectrum of the pure films. Both the position of the vibrational peaks and the intensity distribution is found to be different for the two acceptor molecules (see also figure 6.2). The optical bandgap of the DTTzTz acceptors can be determined from the low-energy onset of the absorption bands. For CN-DTTzTz-CN the edge of the absorption band at 550 nm yields a bandgap of 2.25 eV. For diCN-DTTzTz-diCN the absorption onset at 572 nm corresponds to a bandgap of 2.17 eV. These optical bandgaps are smaller than the bandgaps of 2.51 eV and 2.45 eV for CN-DTTzTz-CN respectively diCN-DTTzTz-diCN obtained from cyclic voltametry data (figure 3.5). Hence the HOMO and LUMO levels in the solid state slightly differ from those obtained from solutions. Yet, the difference in bandgap between the two DTTzTz acceptors remains roughly the same.

The blend spectra exhibit an absorption maximum at 470 nm and 480 nm for CN-DTTzTz-CN:MDMO-PPV respectively diCN-DTTzTz-diCN:MDMO-PPV. The small shift in position of the absorption bands of the blends can be ascribed to the difference in bandgap of the acceptor molecules. Yet, a feature that cannot be explained from the spectra of the constituent materials is the presence of long-wavelength shoulders in the tail region of both blend absorption bands. This could arise from direct CT absorption or strong intermolecular electronic interaction between donor and acceptor compounds in the blends. The long-wavelength tails in the absorption spectra of the pure DTTzTz samples and the CN-DTTzTz-CN:MDMO-PPV blend are caused by diffuse scattering off the film surface.

Figure 6.2 shows the UV-VIS absorption spectra of the pristine P3HT, CN-DTTzTz-CN, diCN-DTTzTz-diCN film and the 1:1 blends of P3HT with the DTTzTz acceptors. The low-bandgap polymer P3HT exhibits an absorption band that is significantly red shifted with respect to the absorption band of MDMO-PPV. Indeed, the absorption spectrum of P3HT exhibits a low-energy onset at 656 nm against an absorption onset of 574 nm for MDMO-PPV. These results

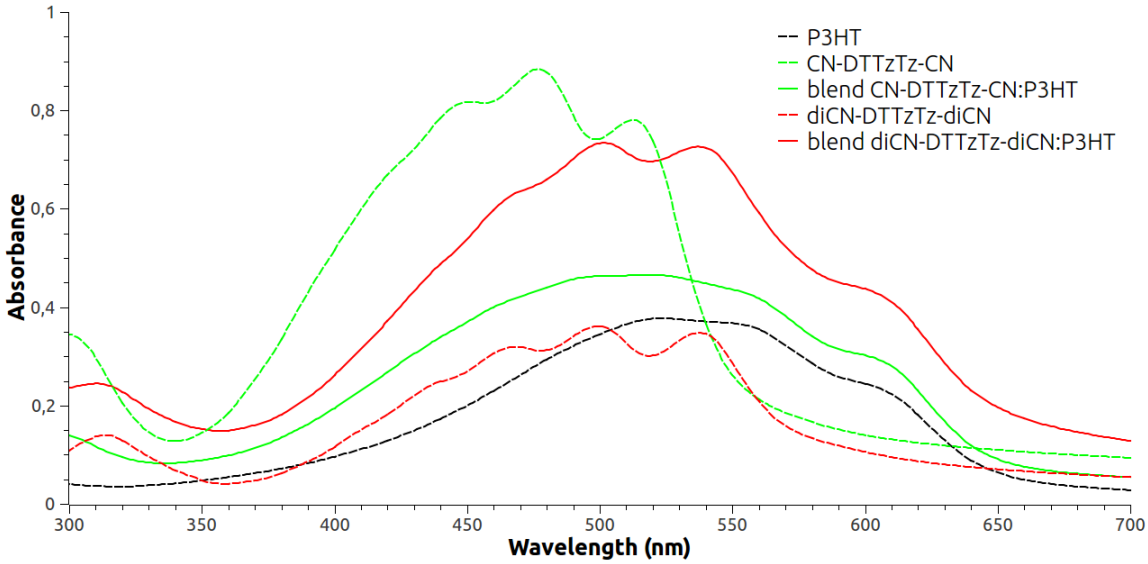

Figure 6.2: UV-VIS absorption spectra of P3HT, CN-DTTzTz-CN, diCN-DTTzTz-diCN and the 1:1 blends of P3HT with the DTTzTz acceptors. Dotted lines represent the pristine films, solid lines the blends.

are in good agreement with the cyclic voltametry data presented in figure 3.5 according to which P3HT has a bandgap of 1.88 eV ($\sim$ 659 nm) whereas MDMO-PPV exhibits a bandgap of 2.18 eV ($\sim$ 569 nm). As a result, the combination of the absorption bands of the DTTzTz acceptors and P3HT will cover a broader wavelength range than the combination with MDMO-PPV where donor and acceptor bands strongly overlapped. Indeed, in figure 6.1 the blend absorption bands roughly extend from 400 nm to 600 nm. Yet for the blends with P3HT in figure 6.2 a larger absorption range from 400 nm to 650 nm is observed. Due to the good absorption properties of the DTTzTz molecules, solar cell devices based on a combination of P3HT with one of the DTTzTz acceptors could therefore exploit a larger part of the solar spectrum than traditional devices with fullerene acceptors that barely contribute to the optical absorption of the OSC.
In the absorption spectrum of the diCN-DTTzTz-diCN:P3HT blend the vibrational structure of diCN-DTTzTz-diCN is still clearly resolved. Also the other characteristics of the blend absorption band seem to be reproducable by a linear combination of the spectra of the pure P3HT and the DTTzTz film. Also for the blend with CN-DTTzTz-CN this is the case. Hence no indications for strong intermolecular interactions between donor and acceptor compounds are found in the blends with P3HT in contrast with the blends with MDMO-PPV.
Finally we remark that the UV-VIS absorption spectra of CN-DTTzTz-CN and the 1:1 CN-DTTzTz-CN:MDMO-PPV blend agree well with the experimental results presented in [10] and [11] which were performed under the same circumstances. However, the concentrations of the solutions used for spin coating were different during our sample preparation. As such the intensities of the absorption spectra cannot be compared.

6.2 PL quenching

PL quenching in donor:acceptor blends is considered a good indicator for the efficiency of charge transfer with respect to radiative decay processes of the photogenerated excitons. In typical polymer:fullerene blends, the PL emission of the fullerene is usually very weak such that CT is investigated by comparing the PL intensity of the donor polymer with the PL of the blend. Yet, in the donor:acceptor systems studied here, both the donor polymers and the novel DTTzTz acceptors exhibit strong PL emission. Hence also the emission spectrum of a pristine

acceptor film should be examined and successful CT should result in quenching of both donor and acceptor PL in the blend.
The samples were excited by a diode laser at 447 nm which lies within the absorption band of both donor polymers and of the DTTzTz acceptors. The spectra were corrected for dark current measured by the detector by subtracting a background spectrum. Also the wavelength dependent sensitivity of the set-up was taken into account by dividing the spectra by the correction factor defined in section 3.3.2. Finally the PL spectra were normalised to the number of photons absorbed at 447 nm. To that end the fraction of the incident laser light that is absorbed by the sample was calculated from $1 - 10^{-A}$ where the absorbance A at 447 nm could be obtained from the absorption spectra presented in the previous section. Note that this normalisation also corrects for the different film thickness of the samples.

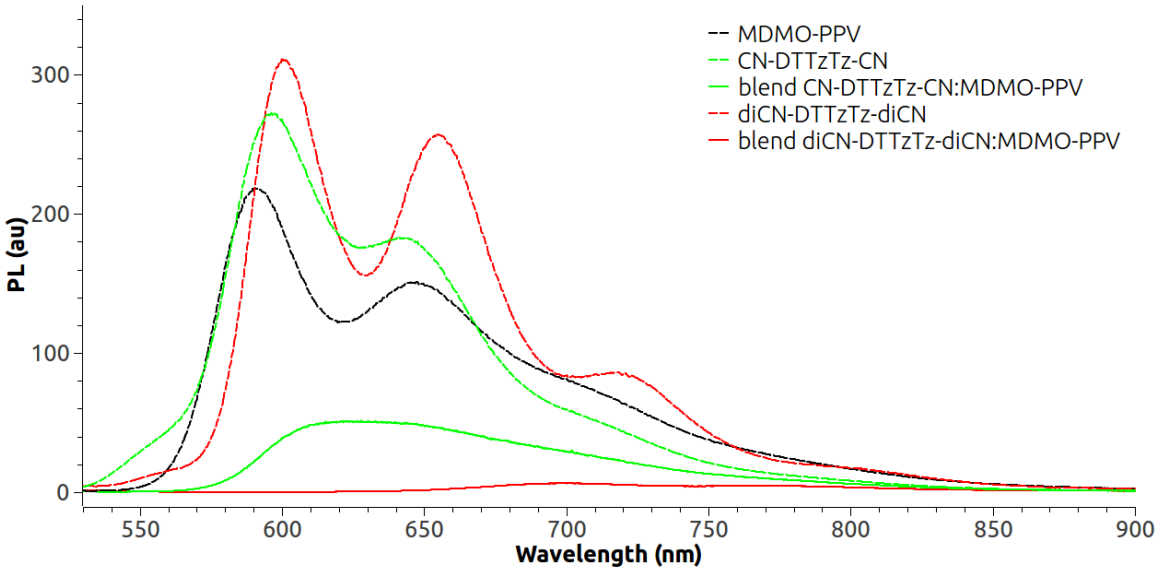

Figure 6.3: PL quenching in MDMO-PPV:CN-DTTzTz-CN (green) and MDMO-PPV:diCN-DTTzTz-diCN (red). Dashed curves represent the pristine materials, solid curves the 1:1 blends. The PL spectra are corrected for the number of photons absorbed at 447 nm.

Figure 6.3 shows the PL spectra of the pure films of MDMO-PPV and the DTTzTz compounds (dashed curves) together with the PL spectra of the corresponding blends (solid curves). In the MDMO-PPV:CN-DTTzTz-CN blend, the PL intensity is reduced to $< 20\%$ compared to the PL of either the pristine polymer or the pure DTTzTz material. For diCN-DTTzTz-diCN an even stronger PL quenching is observed (intensity reduction to $< 3\%$). Hence charge transfer in the blend with diCN-DTTzTz-diCN appears to be more efficient than in the MDMO-PPV:CN-DTTzTz-CN blend. This agrees well with our expectations based on the energetic alignment of donor and acceptor LUMOs shown in figure 3.5. Indeed, the slightly lower LUMO and HOMO of diCN-DTTzTz-diCN with respect to CN-DTTzTz-CN will result in a larger driving force for CT at the D/A interface with MDMO-PPV.
Finally we note that the MDMO-PPV:CN-DTTzTz-CN spectrum is significantly red shifted as compared to the emission spectra of the pure films. According to Nevil et al. [11] this can be ascribed to exciton recombination via states of lower energy induced by heteromolecular interactions between donor and acceptor compounds. Hence it could be interpreted as a first indication of charge transfer in the blend.
In order to examine the shape of the blend spectra in more detail, the normalised PL spectra of the MDMO-PPV - CN-DTTzTz-CN system and the MDMO-PPV - diCN-DTTzTz-diCN system are shown in figure 6.4. Apart from the red shift of the MDMO-PPV:CN-DTTzTz-CN spectrum, the emission range of the blend is comparable to that of the pure MDMO-PPV and

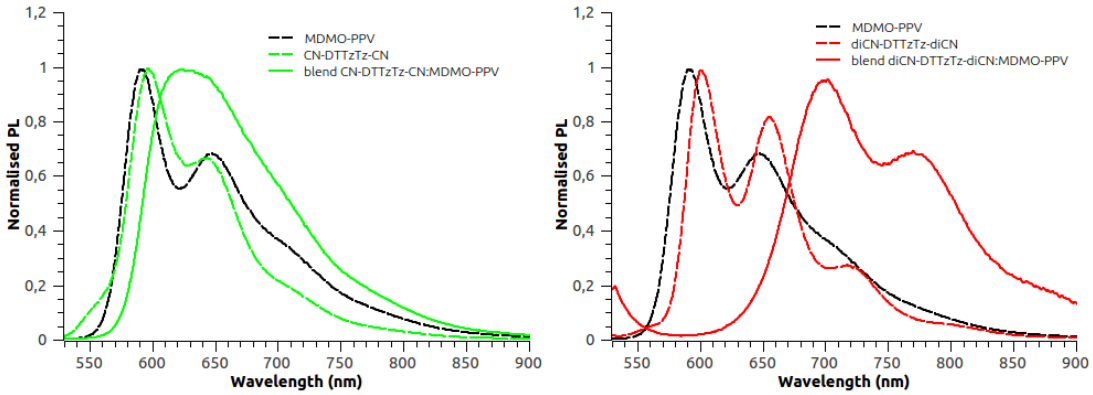

Figure 6.4: Normalised PL spectra of the MDMO-PPV - CN-DTTzTz-CN system (left) and the MDMO-PPV - diCN-DTTzTz-diCN system (right). Dashed curves represent the pristine materials, solid curves the 1:1 blends.

CN-DTTzTz-CN spectra. Nevertheless, the vibrational structure of the pure materials is not resolved in the blend spectrum indicating some kind of interaction between donor and acceptor compounds. As such the PL spectrum of the blend originates mainly from a combination of MDMO-PPV and CN-DTTzTz-CN PL although first indications of the CT transition can be observed. The situation is different for the MDMO-PPV:diCN-DTTzTz-diCN blend. Here the blend emission occurs at significantly longer wavelengths than the largest PL contributions in the pure MDMO-PPV and diCN-DTTzTz-diCN spectra. Note also that the vibrational peaks in the blend spectrum do not coincide with the peaks observed in the PL spectrum of the pure diCN-DTTzTz-diCN film. Hence the PL spectrum of the blend does not originate from emission by the constituent materials and can be attributed to direct CT emission. The increase in PL of the blend at short wavelengths is an artefact caused by scattered laser light that is not completely eliminated by the used cut-off filters. In the other emission spectra, the PL intensity is so large that this weak effect is not noticeable.

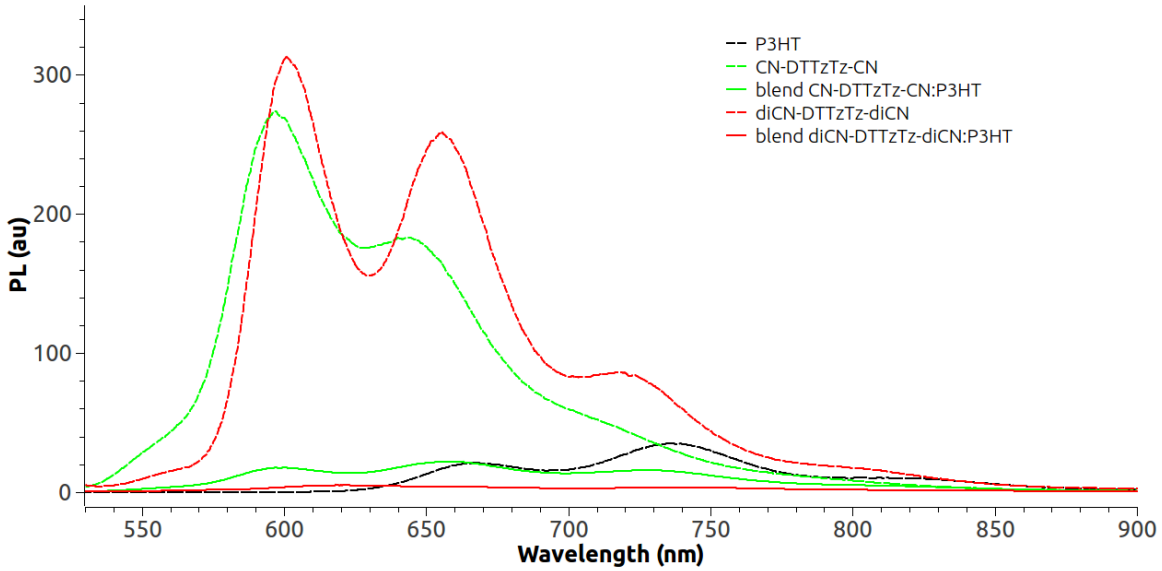

Figure 6.5: PL quenching in P3HT:CN-DTTzTz-CN (green) and P3HT:diCN-DTTzTz-diCN (red). Dashed curves represent the pristine materials, solid curves the 1:1 blends. The PL spectra are corrected for the number of photons absorbed at 447 nm.

Figure 6.5 shows the PL spectra of the pure films of P3HT and the DTTzTz compounds (dashed curves) together with the PL spectra of the corresponding blends (solid curves). Clearly the pure DTTzTz acceptors exhibit more efficient PL than the pristine P3HT. Again a strong PL quenching is observed in both blends. In the P3HT:CN-DTTzTz-CN blend, the PL intensity is reduced to 8% compared to the PL of the pure DTTzTz material. For diCN-DTTzTz-diCN, the acceptor PL intensity is reduced to 1.6% in the blend with P3HT. Hence again the CT appears to be more efficient in the donor:acceptor combination with diCN-DTTzTz-diCN due to its larger acceptor strength as compared to CN-DTTzTz-CN.
We remark that the P3HT emission spectrum does not agree well with earlier experimental results presented in [10]. A possible explanation could be that different kinds of P3HT were used. Our samples were prepared with regioregular P3HT, i.e. P3HT polymers built up from monomers with equal orientation of the side group. Hence differences in the PL spectra could arise from the possibly different emissive properties of normal and regioregular P3HT.

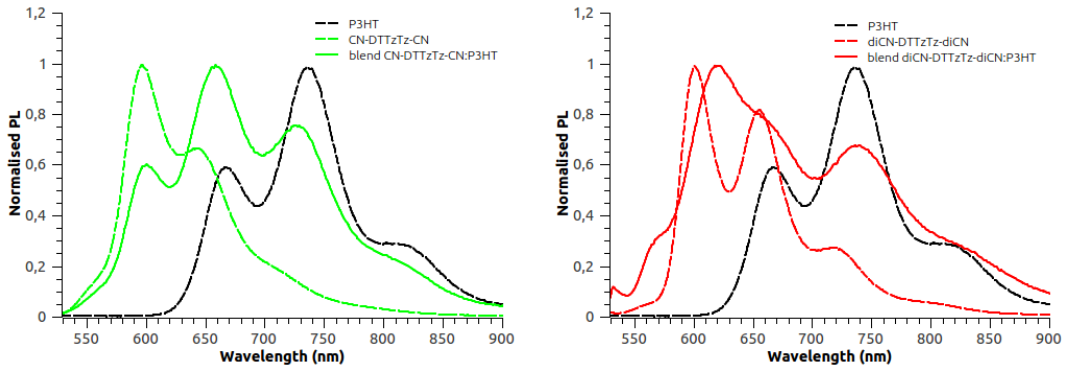

Figure 6.6: Normalised PL spectra of the P3HT - CN-DTTzTz-CN system (left) and the P3HT - diCN-DTTzTz-diCN system (right). Dashed curves represent the pristine materials, solid curves the 1:1 blends.

In order to analyse the shape of the blend spectra in more detail, we again turn to the normalised PL spectra of the P3HT - CN-DTTzTz-CN system and the P3HT - diCN-DTTzTz-diCN system as shown in figure 6.6. The PL spectrum of P3HT:CN-DTTzTz-CN is clearly reproducible by a combination of the spectra of the pure polymer and the DTTzTz acceptor. Indeed, the three peaks observed in the blend PL almost exactly coincide with peaks in the spectra of the constituent materials and no additional CT emission is observed in this system. Also the PL spectrum of the P3HT:diCN-DTTzTz-diCN originates to a large extent from a combination of donor and acceptor PL. For example, the peak at 740 nm in the blend spectrum clearly stems from emission by the donor polymer. As mentioned before, the red shift of the peak at 600 nm corresponding to PL of the pure diCN-DTTzTz-diCN can be ascribed to intermolecular interactions. Yet, the blend spectrum also features a high-energy shoulder between 550 nm and 580 nm that cannot be derived from the spectra of the pure donor and acceptor samples. This effect cannot be ascribed to CT emission because CT emission should occur at lower energy than the PL in the pure materials. An explanation could be that this high-energy shoulder is caused by PL from the glass substrate or by PL from the cut-off filters used in the set-up.
Finally we conclude that the PL quenching observed in all blends of the DTTzTz acceptors with both MDMO-PPV and P3HT provides a first indication for successful CT in these systems. For either of the donor polymers, the PL quenching was stronger in the blend with diCN-DTTzTz-diCN suggesting a more efficient CT than in combinations with CN-DTTzTz-CN. This is in good agreement with our expectations based on the cyclic voltametry data presented in figure 3.5. Indeed, the slightly lower LUMO and HOMO levels of diCN-DTTzTz-diCN with respect to CN-DTTzTz-CN will result in a larger driving force for CT at the D/A interface. In order to further characterise the CT and to investigate the charge carriers created after CT

both wavelength-dependent PIA and TR-PIA measurements were performed. The results are discussed in the following section.

6.3 Triplet and polaron detection by PIA

A major difference in interpretation of the wavelength-dependent PIA spectra in this chapter with respect to the previously studied TPA-DTTzTz-diCN - PC70BM system is that the polaron bands of the positive polarons in MDMO-PPV and P3HT are now known from the literature and lie within the spectral sensitivity of our experimental set-up. Hence it is more straightforward to identify the excited species responsible for the PIA signal in the blend. Still, for the polaron band of the negative polarons on the DTTzTz acceptors no comparison with the literature can be made. Similar to the case of the TPA-DTTzTz-diCN donor material in the previous chapter, also the DTTzTz acceptors were found to exhibit a large PIA signal which was again ascribed to long-lived triplet states. Therefore a comparison was made of the PIA in the pure films of the DTTzTz acceptors and the blends with either MDMO-PPV or P3HT to distinguish between acceptor triplets and polarons in the blend. Also TR-PIA measurements were performed and modelled with the monomolecular and bimolecular models introduced in chapter 4 to examine the nature of the recombination mechanisms in these systems.
The samples were excited at 532 nm by a Nd:YAG laser which was on/off modulated at a frequency of 384 Hz. All PIA spectra presented in this chapter were registered via the lock-in amplifier and with the Si DC detector. For the pure diCN-DTTzTz-diCN sample, an additional wavelength-dependent measurement was performed with the InGaAs detector to ensure sufficient sensitivity in the NIR. PL contributions were eliminated from the spectra by subtracting a reference measurement without probe light from the halogen lamp. The spectra were also corrected for the wavelength-dependent sensitivity of the set-up including the effect of the detector and the filters. Finally the full scale sensitivity of the lock-in detector during the wavelength-dependent measurements was taken into account in order to make the relative PIA scales of all spectra mutually consistent.

6.3.1 Pristine CN-DTTzTz-CN and diCN-DTTzTz-diCN samples

The PIA spectra of the pure CN-DTTzTz-CN and diCN-DTTzTz-diCN film are shown in figure 6.7. Both DTTzTz acceptors exhibit a clear PIA signal with a maximum at 950 nm for CN-DTTzTz-CN and at 1030 nm for diCN-DTTzTz-diCN. Note that the PIA intensity of the latter is a factor 3 smaller than in the CN-DTTzTz-CN sample. Since the PIA signal was attributed to long-lived triplet states, this difference in intensity suggests that the intersystem crossing (ISC) associated with the transition from photogenerated singlet excitons to triplet states is more efficient in the CN-DTTzTz-CN sample.

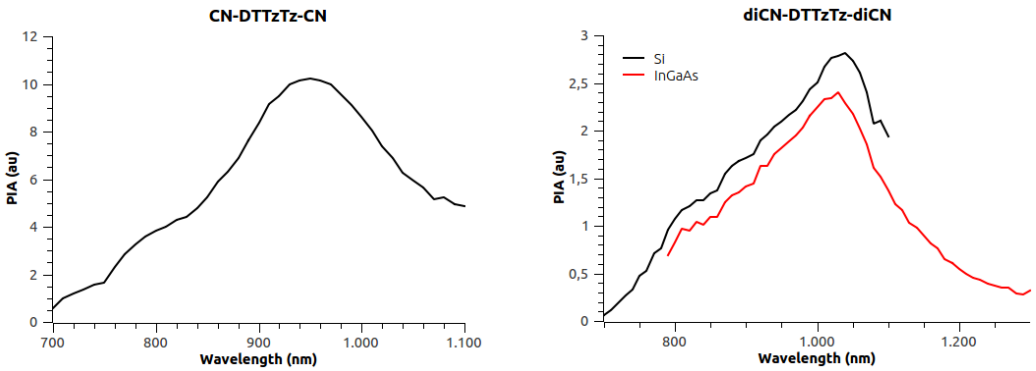

Figure 6.7: PIA spectrum of CN-DTTzTz-CN (left) and diCN-DTTzTz-diCN (right) for a modulation frequency of 384 Hz.

In the previous chapter, we found that the time-dependent PIA signals of the triplets in the pure TPA-DTTzTz-diCN sample were very accurately described by the monomolecular model including ground state depletion. Hence we concluded that geminate recombination was the dominant recombination mechanism in TPA-DTTzTz-diCN. Also for the pure CN-DTTzTz-CN and diCN-DTTzTz-diCN samples TR-PIA measurements were performed to study the triplet recombination kinetics. Three different models were used to fit the experimental data: the two monomolecular models and the bimolecular model without depletion. In order to quantify the agreement between the models and the experimental data, the χ^2 introduced in equation (5.1) was calculated from the best fit with every model and served as a figure of merit to compare the ability of the different models to describe the TR-PIA data. The results are summarised in table 6.1 and clearly demonstrate that the triplet generation and recombination in both DTTzTz acceptors is most adequately described by the monomolecular model including ground state depletion.

Table 6.1: Values of χ^2 obtained for the best fits of the TR-PIA data of both DTTzTz acceptors.

χ^2	CN-DTTzTz-CN	diCN-DTTzTz-diCN
monomolecular model without depletion	96	9.3
monomolecular model with depletion	5.4	2.1
bimolecular model without depletion	126	13.7

The experimental TR-PIA data for the pure CN-DTTzTz-CN and diCN-DTTzTz-diCN sample and the corresponding best fits with the monomolecular model with depletion are shown in figure 6.8. The TR-PIA of the pure CN-DTTzTz-CN sample was measured with the DC Si detector. For the diCN-DTTzTz-diCN film the InGaAs detector was used resulting in a lower signal-to-noise ratio as compared with the measurement on CN-DTTzTz-CN. From the very good agreement between model and experimental data we conclude that geminate recombination governs the recombination kinetics of triplets in CN-DTTzTz-CN and diCN-DTTzTz-diCN.

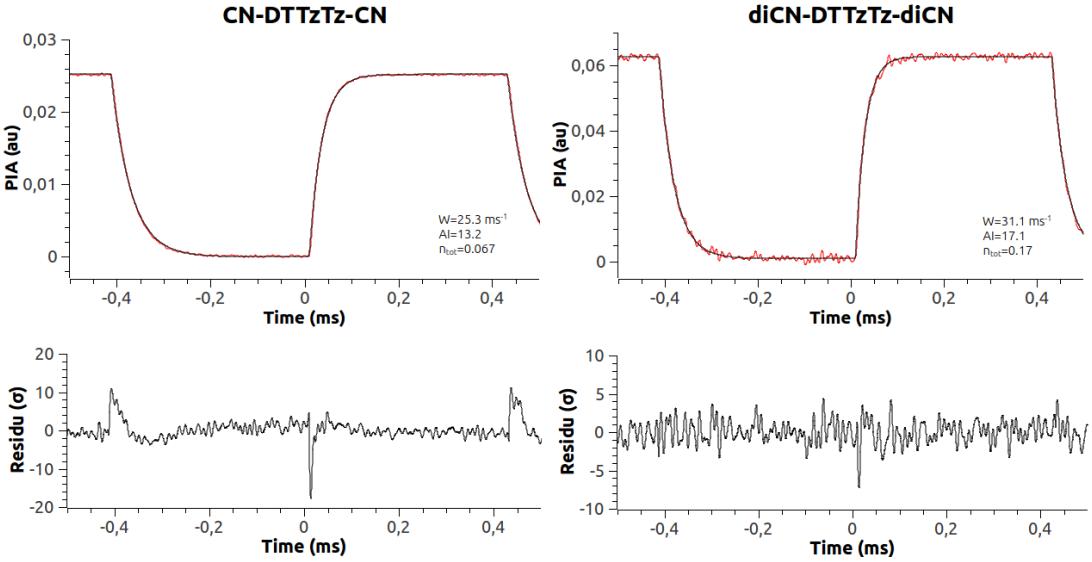

Figure 6.8: Best fits of the experimental TR-PIA data of pure CN-DTTzTz-CN (left) and diCN-DTTzTz-diCN (right) with the monomolecular model including ground state depletion. The TR-PIA was measured at a probe wavelength of $\lambda = 960\,\text{nm}$ respectively $\lambda = 1000\,\text{nm}$ corresponding to the maximal PIA signal measured by the DC Si and the InGaAs detector. Also the residuals are shown to indicate the main deviations between experimental data and model.

The importance of depletion in the model can be estimated by comparing the parameters n_{max} and n_{tot} obtained from the best fit of the TR-PIA data. For CN-DTTzTz-CN we found $n_{max} = 0.025$ and $n_{tot} = 0.067$ hence the amount of triplet excitons already exceeds one third of the total number of available triplet states. Therefore ground state depletion will indeed start to play an important role in the generation and recombination dynamics of the triplet excitons. For diCN-DTTzTz-diCN a similar result was obtained with $n_{max} = 0.067$ and $n_{tot} = 0.17$. Finally, the triplet lifetimes can be calculated from the monomolecular recombination rate W obtained from the best fit of the experimental TR-PIA data. For CN-DTTzTz-CN a recombination rate of $W = 25.3\,\mathrm{ms}^{-1}$ was obtained corresponding to a triplet lifetime of 40 µs. For diCN-DTTzTz-diCN a slightly larger recombination rate of $W = 31.1\,\mathrm{ms}^{-1}$ was found yielding a triplet lifetime of 32 µs. Note that the PIA measurements were performed at liquid nitrogen temperature such that this triplet lifetimes are only valid at $T = 77\,\mathrm{K}$. The larger triplet recombination rate obtained for diCN-DTTzTz-diCN provides an additional explanation for the difference in intensity observed in the PIA spectra of the two DTTzTz acceptors shown in figure 6.7.

6.3.2 Blends of the DTTzTz acceptors with MDMO-PPV

Figure 6.9 shows the PIA spectra of the 1:1 blends of CN-DTTzTz-CN and diCN-DTTzTz-diCN with the standard donor polymer MDMO-PPV. Very similar PIA spectra are obtained in both blends with a maximum at 930 nm. From earlier reports on PIA in MDMO-PPV:PCBM blends we know that this band can be ascribed to positive polarons in the MDMO-PPV [10]. The PIA intensity in the MDMO-PPV:diCN-DTTzTz-diCN is a factor three larger than in the blend with CN-DTTzTz-CN. This is in good agreement with the previous results on PL quenching in blends with MDMO-PPV where we found that the increased acceptor strength of diCN-DTTzTz-diCN resulted in a more efficient charge transfer than in blends with CN-DTTzTz-CN. Note also that the PIA intensities of the blends with MDMO-PPV are much larger than the intensities obtained for triplets in the pure DTTzTz acceptors (figure 6.7).

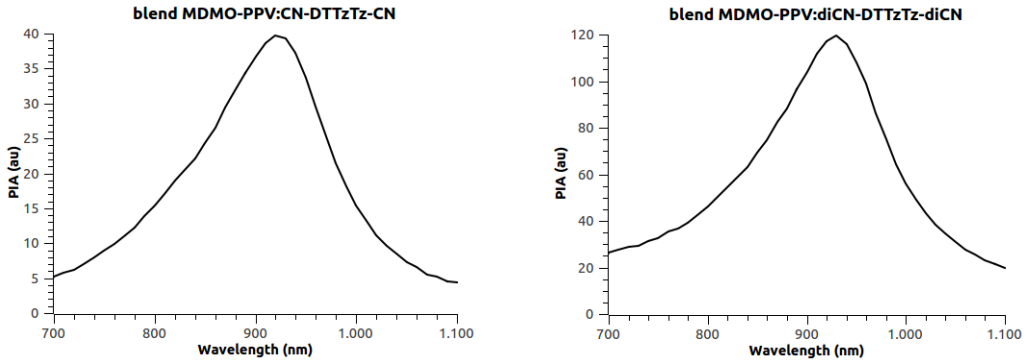

Figure 6.9: PIA spectrum of a 1:1 blend of MDMO-PPV with CN-DTTzTz-CN (left) and diCN-DTTzTz-diCN (right) for a modulation frequency of 384 Hz.

In order to distinguish between geminate and non-geminate recombination of the positive polarons in the blends, also TR-PIA measurements were performed and modelled with the monomolecular and bimolecular model. In figures 6.10 and 6.11 the best fits of the experimental data obtained with the monomolecular model with depletion and the bimolecular model without depletion are compared for both blends. Note the markedly slower response of the PIA in the blends as compared to the TR-PIA of the triplets in the pure DTTzTz acceptors (figure 6.8). Again the χ^2 defined in equation (5.1) was used to quantify the agreement between model and experimental data. The values of χ^2 obtained for the best fits of the TR-PIA data of both blends with the two monomolecular models and the bimolecular model without depletion are presented in table 6.2.

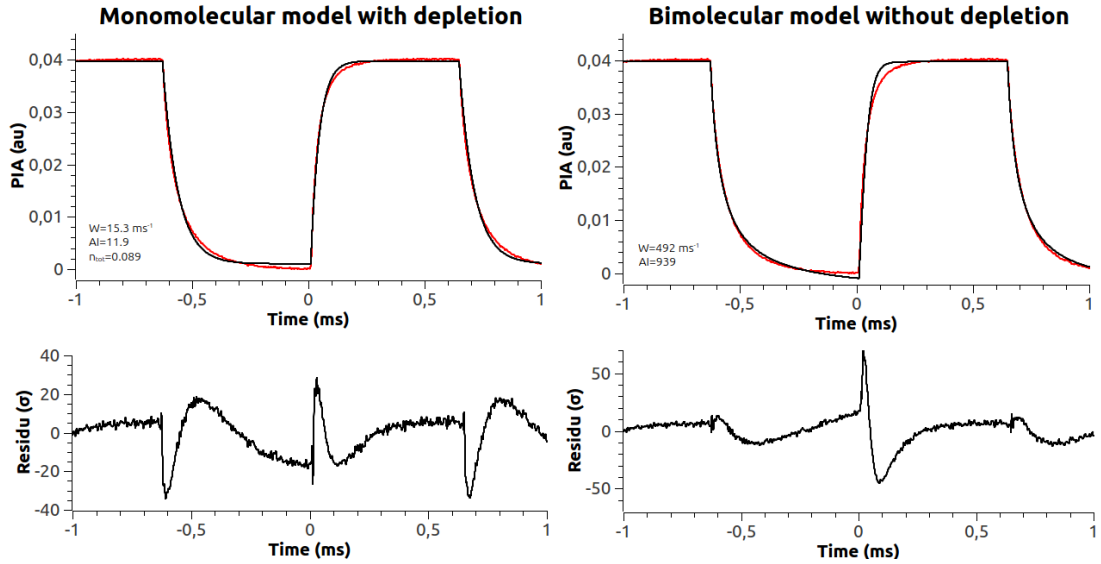

Figure 6.10: Best fits (black) of the experimental TR-PIA data of MDMO-PPV:CN-DTTzTz-CN (red) with the monomolecular model including ground state depletion (left) and the bimolecular model (right). The TR-PIA was measured at a probe wavelength of $\lambda = 950\,\text{nm}$ corresponding to the maximal PIA signal measured by the DC Si detector. Also the residuals are shown to indicate the main deviations between experimental data and model.

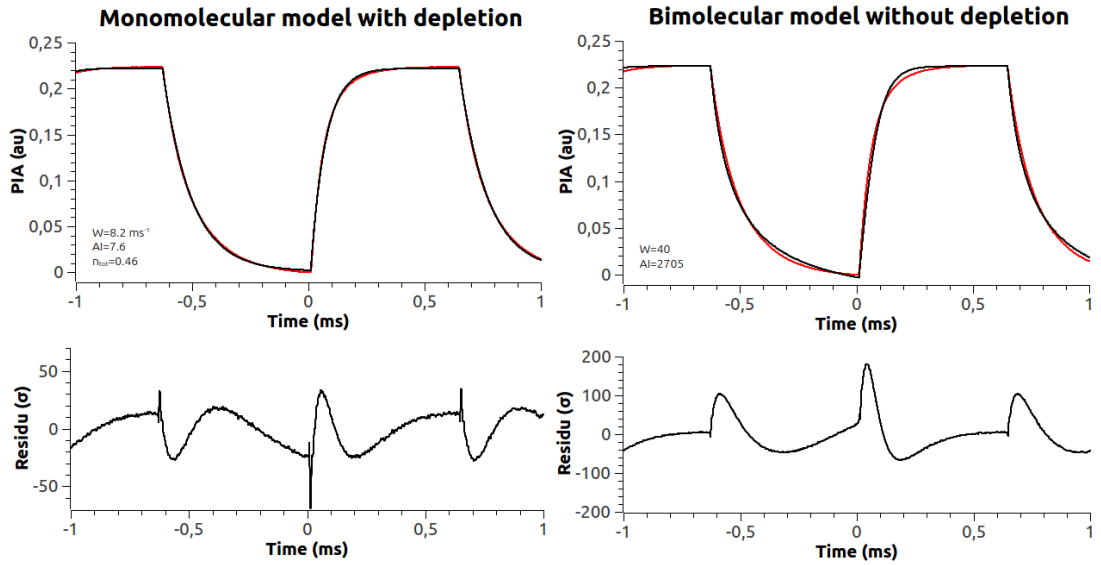

Figure 6.11: Best fits (black) of the experimental TR-PIA data of MDMO-PPV:diCN-DTTzTz-diCN (red) with the monomolecular model including ground state depletion (left) and the bimolecular model (right). The TR-PIA was measured at a probe wavelength of $\lambda = 930\,\text{nm}$ corresponding to the maximal PIA signal measured by the DC Si detector. Also the residuals are shown to indicate the main deviations between experimental data and model.

Note that the values of χ^2 are much larger than in the case of the pure DTTzTz acceptors due to the large signal-to-noise ratios of the PIA in the blends resulting in very small standard deviations. Because χ^2 uses the standard deviation as a weighing factor for the deviations between model and experiment it can underestimate the goodness of fit when the noise level is very low. Indeed, the χ^2 rapidly increases for minor deviations of the model although qualitative evaluation of the best fits yields a reasonable agreement between model and experimental data. This is also clear from the residuals shown in figures 6.10 and 6.11. Hence an alternative figure of merit that weighs deviations between model and experiment on the total intensity of the signal rather than the standard deviation could be more suitable to asses the goodness of fit in measurements with very high signal-to-noise ratios. Nevertheless, the quality of the best fits obtained for the different models can still be compared based on the χ^2 ratios.

Table 6.2: Values of χ^2 obtained for the best fits of the TR-PIA data of the blends with MDMO-PPV.

χ^2	MDMO-PPV: CN-DTTzTz-CN	MDMO-PPV: diCN-DTTzTz-diCN
monomolecular model without depletion	483	6649
monomolecular model with depletion	124	224
bimolecular model without depletion	162	2210

The values of χ^2 listed in table 6.2 indicate that the monomolecular model with ground state depletion succeeds best in reproducing the time-dependence of the PIA signal in both blends. Yet, the TR-PIA data of the blends could not be as closely fit with this model as the PIA data of the pure DTTzTz acceptors and significant deviations between model and experimental data can be observed in figures 6.10 and 6.11. In the MDMO-PPV:CN-DTTzTz-CN blend the best fit with the monomolecular model with depletion clearly exhibits some systematic deviations from the experimental data. The exponential rise and decay predicted by the model are both faster than what is experimentally observed. Moreover the polaron concentration in the off-period seems to reach a constant value in the monomolecular model whereas the experimental PIA-signal continuously decreases until the laser is switched on again. Remark that the deviations from the experimental data during the off-period are complementary for the monomolecular and bimolecular model. Hence the experimental data could probably be more accurately described by a combination of the two models suggesting that the polaron recombination in the blend is in fact governed by a mixture of geminate and non-geminate recombination processes. For the MDMO-PPV:diCN-DTTzTz-diCN blend, a better agreement between the monomolecular model with depletion and the experimental data is found although the same systematic deviations from the TR-PIA data can be observed. From the fitting parameters corresponding to the best fit with the monomolecular model with depletion, an effective polaron lifetime of 65 µs was obtained for the blend with CN-DTTzTz-CN. For MDMO-PPV:diCN-DTTzTz-diCN a significantly larger polaron lifetime of 122 µs was found which correlates well with the larger PIA intensity observed in this blend (figure 6.9). Note also that the polaron lifetimes are larger than the triplet lifetimes obtained for the pure DTTzTz acceptors in agreement with the slower PIA response in the blends.

From the fact that the monomolecular model seems best suited to describe the TR-PIA data in both blends, we could conclude that geminate recombination processes dominate the decay of the positive polarons. A good way to confirm the importance of geminate recombination in these systems would be to measure the TR-PIA data for variable laser power and check whether the monomolecular model reproduces the correct behaviour as function of excitation intensity. In any case, the fact that the polaron recombination is dominated by geminate decay processes points to an inefficient charge separation in the blends and is detrimental for the solar cell performance. This seems to explain the poor power conversion efficiencies of

$< 0.1\%$ reported earlier for devices with a MDMO-PPV:CN-DTTzTz-CN blend as active layer [11]. Very recently also solar cells with an active layer consisting of a MDMO-PPV:diCN-DTTzTz-diCN blend were tested at UHasselt. For these devices a large open circuit voltage of $V_{oc} = 1.10\,\mathrm{V}$ was obtained. Yet the overall photovoltaic performance was rather poor resulting in a maximal PCE of only 0.03%.

6.3.3 Blends of the DTTzTz acceptors with P3HT

Figure 6.12 shows the PIA spectra of the 1:1 blends of CN-DTTzTz-CN and diCN-DTTzTz-diCN with the low-bandgap polymer P3HT. At room temperature, the polaron band of P3HT is known to exhibit two maxima around 680 nm and 990 nm [10]. Hence the PIA bands observed in the blends with the DTTzTz acceptors are clearly distinct from the polaron band of P3HT expected from the literature. Yet, the PIA spectra shown in figure 6.12 were obtained from measurements at liquid nitrogen temperature and it is not unlikely that the polaron band of P3HT at 77 K significantly differs from the one at room temperature. Therefore it cannot be ruled out that the PIA spectra in figure 6.12 are at least partly due to positive polarons in the polymer. Other excited species that could be responsible for the observed PIA signal are negative polarons in the DTTzTz acceptors or long-lived triplet states. The PIA bands of the acceptor triplets were obtained from measurements on pure films of the DTTzTz materials and were presented earlier in figure 6.7. We recall that the PIA spectra of the acceptor triplets exhibit a maximum at 950 nm for CN-DTTzTz-CN and at 1030 nm for diCN-DTTzTz-diCN. This is not very different from the maxima at 1020 nm and 1060 nm observed in the blends with P3HT in figure 6.12. Note also that the intensity of both PIA spectra is comparable to the PIA intensities of the acceptor triplets whereas for the polarons in MDMO-PPV blends ten times larger PIA signals were obtained. Hence it is reasonable to assume that the PIA spectra in figure 6.12 originate partly from acceptor triplet excitations.

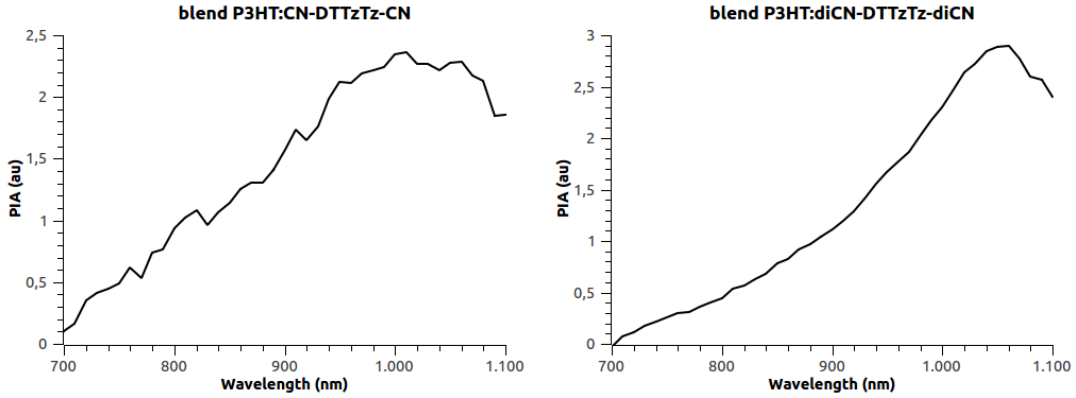

Figure 6.12: PIA spectrum of a 1:1 blend of P3HT with CN-DTTzTz-CN (left) and diCN-DTTzTz-diCN (right) for a modulation frequency of 384 Hz.

An additional confirmation of the contribution of the triplet states to the PIA signal could be derived from the time-dependence of the PIA. Indeed, the TR-PIA of the pristine CN-DTTzTz-CN and diCN-DTTzTz-diCN samples was characterised by a markedly faster rise and decay than what we observed for the polarons in the blends with MDMO-PPV. Hence the recombination constants from the best fits of the TR-PIA data for the blends with P3HT could help to distinguish between triplets and the slower generation and recombination kinetics associated with polarons. To that end, the TR-PIA measurements of the blends were modelled with the monomolecular and bimolecular models. Like before, the χ^2 defined in equation (5.1) was used to quantify the agreement between the experimental data and the best fits with the two monomolecular models and the bimolecular model without depletion. The values of χ^2 obtained for the best fits of the TR-PIA data of the two blends are listed in table 6.3.

Table 6.3: Values of χ^2 obtained for the best fits of the TR-PIA data of the blends with P3HT.

χ^2	P3HT: CN-DTTzTz-CN	P3HT: diCN-DTTzTz-diCN
monomolecular model without depletion	3.3	1.4
monomolecular model with depletion	2.2	1.1
bimolecular model without depletion	7.1	2.5

Again the monomolecular model including ground state depletion yields the best agreement with the experimental data. In figures 6.13 and 6.14 the best fits of the experimental data obtained with the monomolecular model and the bimolecular model are compared for both blends.
The differences between the monomolecular model and the experimental data observed in figures 6.13 and 6.14 are similar to what we found in our analysis of the TR-PIA data of the blends with MDMO-PPV in the previous section. Again the monomolecular and bimolecular model are seen to exhibit complementary deviations from the experimental data in the off-period. Hence it seems plausible that the time-dependence of the PIA signals is more accurately described by a combination of the two models indicating that both geminate and non-geminate recombination processes occur in the blends. Yet, the experimental TR-PIA data in figures 6.13 and 6.14 exhibit much larger noise levels as compared to the measurements on the blends with MDMO-PPV. As such conclusions about the qualitative agreement between the models and the experimental data are not as decisive as in the case of the MDMO-PPV blends. A good approach to confirm the ability of the models to describe the PIA in the blends would be to fit TR-PIA measurements for variable laser power.

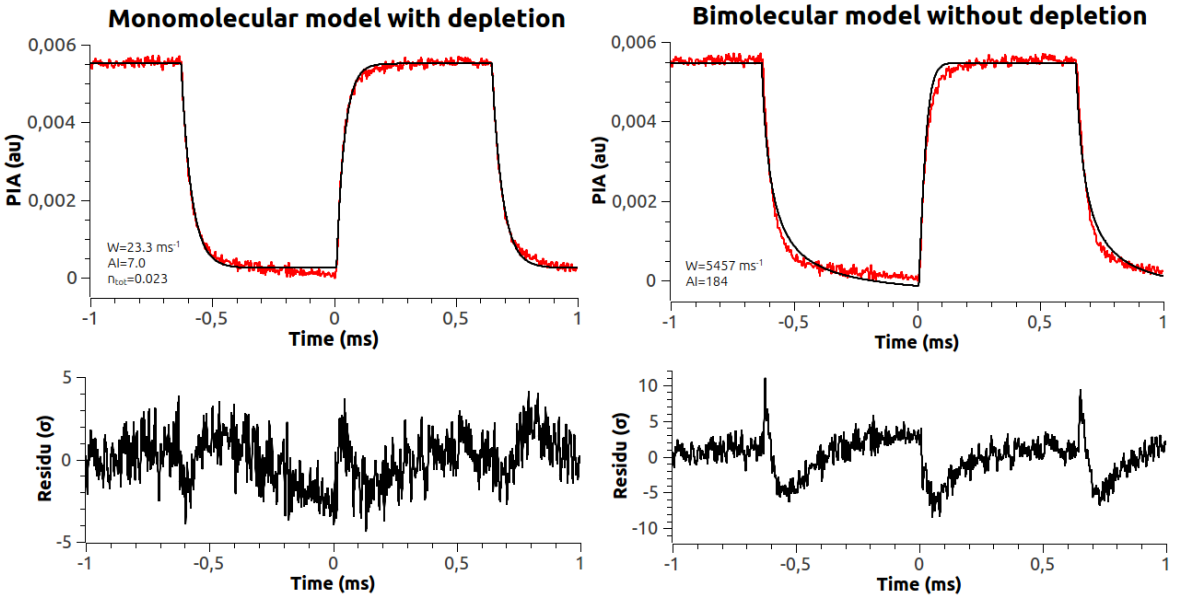

Figure 6.13: Best fits of the experimental TR-PIA data of P3HT:CN-DTTzTz-CN with the monomolecular model including ground state depletion (left) and the bimolecular model (right). The TR-PIA was measured at a probe wavelength of $\lambda = 990\,\text{nm}$ corresponding to the maximal PIA signal measured by the DC Si detector. Also the residuals are shown to indicate the main deviations between experimental data and model.

For P3HT:CN-DTTzTz-CN, the recombination rate obtained from the best fit of the TR-PIA data with the monomolecular model with depletion was given by $W = 23.3\,\text{ms}^{-1}$ corresponding to a lifetime of 43 µs. For P3HT:diCN-DTTzTz-diCN a monomolecular recombination rate of

$W = 35.6\,\mathrm{ms}^{-1}$ corresponding to 28 µs was found. These lifetimes agree well with the triplet lifetimes of 40 µs and 32 µs obtained from the TR-PIA measurements on the pure CN-DTTzTz-CN and diCN-DTTzTz-diCN samples. On the other hand, the polaron lifetimes in the blends with MDMO-PPV were twice as large. Hence, also the TR-PIA data suggest that exciton triplets are to a large extent responsible for the PIA signal observed in the blends with P3HT. The importance of depletion in the model was estimated by comparing the parameters n_{max} and n_{tot}. For the blend with CN-DTTzTz-CN we obtained $n_{tot} \approx 4 \times n_{max}$. The effect of depletion was smaller in the blend with diCN-DTTzTz-diCN for which we found $n_{tot} \approx 6 \times n_{max}$. These ratios of n_{max} and n_{tot} are also comparable to our earlier results for the triplets in the pristine CN-DTTzTz-CN and diCN-DTTzTz-diCN samples.

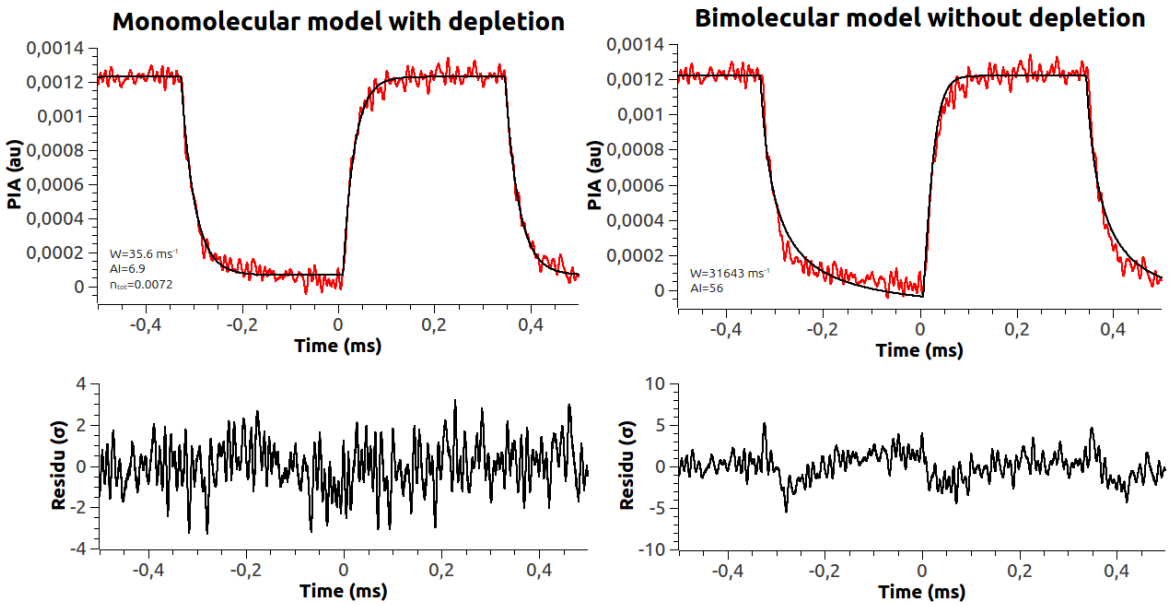

Figure 6.14: Best fits of the experimental TR-PIA data of P3HT:diCN-DTTzTz-diCN with the monomolecular model including ground state depletion (left) and the bimolecular model (right). The TR-PIA was measured at a probe wavelength of $\lambda = 1010\,\mathrm{nm}$ corresponding to the maximal PIA signal measured by the DC Si detector. Also the residuals are shown to indicate the main deviations between experimental data and model.

In contrast to the blends with MDMO-PPV, we could not attribute the entire PIA signal to positive polarons in the polymer. Instead, the comparable PIA intensities and the similar time-dependence of the PIA observed in the pure CN-DTTzTz-CN and diCN-DTTzTz-diCN samples suggest that acceptor triplets contribute to a large extent to the PIA signal in the blends with P3HT. Hence the small driving force for charge transfer at the D/A interface seems to severely limit the generation of polarons in blends of the DTTzTz acceptors with P3HT. This is probably the reason for the low efficiencies obtained for OSCs based on these materials by the group of prof. dr. Wouter Maes at UHasselt. The first tests on solar cell devices with an active layer consisting of P3HT:diCN-DTTzTz-diCN resulted in poor PCE's of only 0.21%. Note that this efficiency is an order of magnitude larger than the PCEs obtained for devices with MDMO-PPV:diCN-DTTzTz-diCN. Yet, this increase in efficiency is mainly caused by the improved hole mobility in P3HT and doesn't necessarily suggest a larger CT efficiency in the blends with P3HT. Despite the large effective bandgap in the P3HT - diCN-DTTzTz-diCN system, a surprisingly small open circuit voltage of $V_{oc} = 0.27\,\mathrm{V}$ was found for these solar cells. It should be kept in mind however that these parameters were obtained for a first set of devices without a preliminary optimization study to determine the ideal donor:acceptor ratio, type of solvent, ... Hence other factors such as a bad BHJ morphology may have given rise to the odd V_{oc} observed in these solar cells. Therefore a further optimization study should be performed

to rule out morphology problems and to confirm the magnitude of the PCEs obtained for these first devices. For solar cells based on P3HT:CN-DTTzTz-CN blends, much lower PCEs of about 0.003% were obtained indicating that the even smaller driving force for charge transfer in this system greatly limits the photovoltaic performance.

6.4 Conclusion

In this chapter we presented the results of our study of the novel acceptor molecules CN-DTTzTz-CN and diCN-DTTzTz-diCN in combination with the conventional donor polymers MDMO-PPV and P3HT. Two trends in the CT efficiency of the blends were investigated: on the one hand the effect of a larger electron-acceptor strength when going from CN-DTTzTz-CN to diCN-DTTzTz-diCN and on the other hand the evolution of the CT efficiency when replacing MDMO-PPV by the low-bandgap polymer P3HT. For either of the donor polymers, stronger PL quenching was observed in blends with diCN-DTTzTz-diCN suggesting a more efficient CT than in combinations with CN-DTTzTz-CN in good agreement with the increased acceptor strength. In the blends with MDMO-PPV, the PL spectra revealed indications of a CT-band whereas the PL spectra of the blends with P3HT were almost exactly reproducible by a combination of the emission spectra of the pure polymer and the DTTzTz acceptor. Hence a more efficient CT is observed for the blends with MDMO-PPV correlating well with the larger driving force for CT at the D/A interface in these systems.
In order to further characterise the CT in the blends and to investigate the charge carriers created after CT both wavelength-dependent PIA and TR-PIA measurements were performed. The results confirmed the trends observed in the PL spectra. The blends with MDMO-PPV exhibited a large PIA signal that could be attributed to positive polymers on the donor. Yet, modelling of the TR-PIA data demonstrated that the recombination kinetics of the polarons in the blends is dominated by geminate recombination which is detrimental for the photovoltaic performance. Hence this could explain the poor power conversion efficiencies obtained for solar cells based on these materials. In the blends with P3HT a much smaller PIA signal was found that could not be entirely attributed to polarons. Instead, the time-dependence and magnitude of the PIA signal were similar to the PIA measured in the pure CN-DTTzTz-CN and diCN-DTTzTz-diCN samples which was ascribed to long-lived triplets. Hence we concluded that the PIA in the blends with P3HT originated to a large extent from triplet excitations. As such the small driving force for charge transfer at the D/A interface was found to greatly limit the generation of polarons in blends of the DTTzTz acceptors with P3HT.

Chapter 7

Conclusions and outlook

The work presented in this thesis contributed to the research on novel OPV materials with a study of recently synthesised DTTzTz materials for use in bulk heterojunction organic solar cells. The goal of this thesis was to characterise the charge transfer efficiency in different donor:acceptor blends by means of UV-VIS absorption, photoluminescence and photo-induced absorption spectroscopy. Furthermore, we aimed at a more fundamental understanding of the photo-induced charge generation and recombination processes in the blends via the modelling of time-dependent PIA signals. Two intrinsically different systems were investigated in this thesis: (1) TPA-DTTzTz-diCN studied as a novel donor material in combination with the standard acceptor PC70BM and (2) CN-DTTzTz-CN and diCN-DTTzTz-diCN studied as acceptors in blends with the conventional donor polymers MDMO-PPV and P3HT. The combination of the DTTzTz donor with PC70BM was shown to be a viable route to obtain blends with efficient CT. In the blends of the DTTzTz acceptors with MDMO-PPV and P3HT, however, the low driving force for CT was found to severely limit the generation of mobile charge carriers resulting in poor photovoltaic performance of devices based on these materials. From the results of this thesis together with the earlier report on blends of CN-DTTzTz-CN and two other DTTzTz acceptors with MDMO-PPV [11] we conclude that the design of new DTTzTz derivatives with increased electron-acceptor strength is essential to improve the CT efficiency in these systems and the PCEs of the corresponding solar cells.

Finally, we end by presenting two possible topics for future research on the DTTzTz materials. In this thesis, we emphasised the importance of understanding loss mechanisms in novel blends for organic solar cells. In that context, the modelling of time-dependent PIA is a useful tool to study the recombination processes of polarons in donor:acceptor blends. Hence further improvement of the theoretical models used to describe time-dependent PIA signals could yield interesting new information on the polaron generation and recombination kinetics. For instance, a straightforward extension to the monomolecular and bimolecular models presented in this thesis could be achieved by including the effect of inhomogeneous generation or recombination of polarons. In any case, the best fits of the TR-PIA of the different blends studied in this thesis all exhibited systematic deviations from the experimental data. Hence there is still room for improvement of the models in order to obtain a better agreement with the experimental data. Another feature of the PIA of blends with DTTzTz compounds that could be explored in future research is the temperature dependence. Nevil et al. [11] reported on temperature dependent PIA measurements on blends of CN-DTTzTz-CN with MDMO-PPV and observed a significant reduction of the polaron lifetime when the temperature was increased from 77 K to room temperature. This was ascribed to thermally activated carrier recombination over a relatively low energy barrier which would be detrimental for the solar cell performance. Hence also in the other blends with DTTzTz molecules studied in this thesis thermally activated carrier recombination could take place. In the models for the TR-PIA signals, thermally activated recombination would only affect the recombination constant. Therefore it would

be interesting to investigate the temperature dependence of the PIA by modelling the time-dependent signals with all parameters fixed except the recombination constant. Hence from the evolution of the recombination constant with temperature we could gain a more thorough understanding of the effect of temperature on the polaron recombination kinetics.

Appendix A

Nederlandstalige samenvatting

De ontdekking van geleidende polymeren in de jaren '70 heeft het begin ingeluid van een nieuwe generatie zonnecellen gebaseerd op organische halfgeleiders. Ondanks de lagere fotovoltaïsche efficiënties worden organische zonnecellen beschouwd als een veelbelovend goedkoop alternatief voor de traditionele zonnecellen gebaseerd op inorganische halfgeleiders zoals silicium. Bovendien kunnen organische zonnecellen geproduceerd worden vanuit oplossingen via lage-temperatuursprocessen zoals spincoaten en printen. Daardoor zijn ze compatibel met flexibele substraten zoals plastics wat volledig nieuwe elektronische toepasingen mogelijk maakt. De snelle toename van de omzettingsefficiënties van organische zonnecellen de voorbije 10 jaar toont het potentiëel aan van deze technologie als een duurzame en goedkope energiebron voor de toekomst. Veel wetenschappelijk onderzoek wordt nog steeds gewijd aan het begrijpen van de fysische processen die plaatsgrijpen in organische fotovoltaïsche (OPV) systemen. Gebaseerd op deze kennis kunnen dan nieuwe organische materialen ontwikkeld worden om de zonnecelefficiënties te verbeteren.

Deze thesis draagt bij aan het onderzoek naar nieuwe OPV materialen met een studie van recent gesynthetiseerde 2,5-dithienylthiazolo[5,4-d]thiazole (DTTzTz) moleculen. De moleculen werden ontwikkeld voor gebruik in bulk-heterojunctie organische zonnecellen wat tot nu toe de meest succesvolle device-architectuur voor OPV systemen is. De actieve laag van zulke devices bestaat uit een interpenetrerend netwerk van twee verschillende organische halfgeleiders, een die fungeert als elektron donor en de andere als elektron acceptor. Een belangrijke stap in het fotovoltaïsche proces van dit type zonnecellen is de ladingsoverdracht tussen donor en acceptor wanneer het device belicht wordt. In deze thesis wordt de fotogeïnduceerde ladingsoverdracht in verschillende donor-acceptor mengsels met de DTTzTz materialen optisch gekarakteriseerd door middel van absorptie-, fluorescentie- en fotogeïnduceerde absorptiespectroscopie (PIA) op gespincoate films. Van bijzonder belang was het modelleren van tijdsafhankelijke PIA metingen om de generatie- en recombinatiekinetiek van ladingsdragers in de mengsels te onderzoeken.

In het eerste hoofdstuk van deze thesis wordt een korte algemene inleiding gegeven die de mogelijkheden van organische zonnecellen als een goedkope en duurzame energiebron bespreekt en de huidige stand van zaken op gebied van omzettingsefficiënties en de device-stabiliteit behandelt. Hoofdstuk 2 biedt een meer gedetailleerde theoretische achtergrond over de fysica achter organische zonnecellen en de werkingsprincipes van de devices. We focussen op bulk-heterojunctie zonnecellen omdat de materialen bestudeerd in deze thesis ontwikkeld zijn voor gebruik in zulke devices. De relevantie van het onderzoek in deze thesis wordt gemotiveerd aan de hand van enkele belangrijke thema's in het hedendaags onderzoek naar OPV systemen. Hoofdstuk 3 behandelt de bereiding van samples en de experimentele technieken die gebruikt werden om de nieuwe zonnecelmaterialen te karakteriseren. De toepassing van elke techniek in de context van onderzoek naar organische zonnecellen en de bijhorende experimentele opstellingen worden daar besproken. Tijdsafhankelijke fotogeïnduceerde absorptiemetingen blijken bijzonder geschikt om de dynamica van ladingsgeneratie en -recombinatie

in donor-acceptor mengsels voor organische zonnecellen te bestuderen. Door de experimentele data te modelleren kan de aard van de recombinatieprocessen bestudeerd worden. Dit levert essentiële informatie op over de mogelijke fotovoltaïsche prestatie van zonnecellen gebaseerd op mengsels van die materialen. In hoofdstuk 4 worden twee verschillende modellen geïntroduceerd om de tijdsafhankelijke PIA data te beschrijven: het monomoleculaire en bimoleculaire model. De wiskundige formulering en de onderliggende fysische mechanismen van beide modellen worden besproken en een uitbreiding van de modellen wordt opgesteld door het effect van depletie mee in rekening te brengen. In hoofdstuk 5 presenteren we de resultaten van onze studie van de nieuwe donor molecule TPA-DTTzTz-diCN in combinatie met het standaard acceptor materiaal PC70BM. Efficiënte ladingsoverdracht in dit systeem werd aangetoond door de afname van donor emissie in het fluorescentiespectrum van de blend en door het duidelijke PIA signaal afkomstig van excitaties van positieve polaronen. Verrassend genoeg werd ook in de pure TPA-DTTzTz-diCN films een groot PIA signaal waargenomen. Dit werd toegeschreven aan triplet excitonen. Van bijzonder belang was het modelleren van tijdsafhankelijke PIA metingen voor verschillende laservermogens om de fysische mechanismen achter de recombinatiekinetiek van polaronen en triplets bloot te leggen. Uit de zeer goede overeenkomst tussen het monomoleculaire model met depletie en de experimentele data voor de pure TPA-DTTzTz-diCN film werd geconcludeerd dat het verval van triplettoestanden via geminate recombinatieprocessen plaatsvindt. Voor de blend vonden we dat het bimoleculaire model zonder depletie het best geschikt was om de tijdsafhankelijke PIA signalen te beschrijven. Dit wijst erop dat non-geminate processen de recombinatiekinetiek domineren. In hoofdstuk 6 worden twee recent gesynthetiseerde acceptor moleculen, CN-DTTzTz-CN en diCN-DTTzTz-diCN, bestudeerd in combinatie met de conventionele donor polymeren MDMO-PPV en P3HT. Succesvolle ladingsoverdracht tussen donor en acceptor werd onderzocht door middel van de onderdrukking van fluorescentie in de blends en PIA metingen om de ladingsdragers gecreëerd door laserexcitatie te bestuderen. De grotere efficiëntie van de ladingsoverdracht in blends met diCN-DTTzTz-diCN kwam goed overeen met het sterkere acceptorkarakter van dit materiaal in vergelijking met CN-DTTzTz-CN. In de blends met MDMO-PPV werd een efficiënte ladingsscheiding vastgesteld maar werd de fotovoltaïsche werking sterk gehinderd door geminate recombinatieprocessen. De blends met P3HT vertoonden een PIA signaal dat voor een groot deel te wijten was aan excitaties van triplettoestanden. Daaruit concludeerden we dat de kleine drijvende kracht voor ladingsscheiding aan de donor-acceptor interface in deze systemen de vorming van mobiele polaronen sterk limiteert. Beste fits van de tijdsafhankelijke PIA metingen binnen de mono- en bimoleculaire modellen gaven aanwijzingen omtrent de dominante recombinatieprocessen in de blends, maar onthulden ook de complexiteit van de bestudeerde systemen omdat geen enkel model erin slaagde de experimentele data voldoende accuraat te beschrijven. Daarom is het belangrijk fysisch relevante uitbreidingen van de modellen te overwegen. Het laatste hoofdstuk vat kort de resultaten en conclusies van deze thesis samen en biedt ook een vooruitblik naar verder onderzoek naar de DTTzTz materialen.

Bibliography

[1] *Organic Photovoltaics: Materials, Device Physics, and Manufacturing Technologies*. Wiley-VCH, 2014.

[2] Dechan Angmo and Frederik C. Krebs. Flexible ITO-free polymer solar cells. *Journal of Applied Polymer Science*, 2012.

[3] Carsten Deibel and Vladimir Dyakonov. Polymer-fullerene bulk heterojunction solar cells. *Reports on Progress in Physics*, 2010.

[4] Liam Emmett, Giles M. Prentice, and G. Dan Pantos. Donor-acceptor interactions in chemistry. *Annual Reports on the Progress in Chemistry - Section B (Organic Chemistry)*, 2013.

[5] Paul Janssen. *Spins in organic semiconductors: Revealing the dominant mechanisms of organic magnetoresistance*. PhD thesis, Technische Universiteit Eindhoven, 2013.

[6] Mikkel Jorgensen, Kion Norrman, and Frederik C. Krebs. Stability/degradation of polymer solar cells. *Solar Energy Materials and Solar Cells*, 2008.

[7] Takashi Kobayashi, Yosuke Terada, Takashi Nagase, and Hiroyoshi Naito. Determination of carrier lifetime in bulk-heterojunction solar cells by continuous-wave photoinduced absorption spectroscopy. *Applied Physics Express*, 2011.

[8] Julija Kudrjasova, Roald Herckens, Huguette Penxten, Peter Adriaensens, Laurence Lutsen, Dirk Vanderzande, and Wouter Maes. Direct arylation as a versatile tool towards thiazolo[5,4-d]thiazole-based semiconducting materials. *Organic and Biomolecular Chemistry*, accepted for publication in 2014.

[9] Yuhang Liu, Jingbo Zhao, Zhengke Li, Cheng Mu, Wei Ma, Huawei Hu, Kui Jiang, Haoran Lin, Harald Ade, and He Yan. Aggregation and morphology control enables multiple cases of high-efficiency polymer solar cells. *Nature Communications*, accepted for publication in 2014.

[10] Nissy Nevil. *Optical spectroscopy investigation of charge transfer and recombination in blends of MDMO-PPV with novel small molecule acceptors*. PhD thesis, Universiteit Antwerpen, 2014.

[11] Nissy Nevil, Yu Ling, Sarah Van Mierloo, Jurgen Kesters, Fortunato Piersimoni, Peter Adriaensens, Laurence Lutsen, Dirk Vanderzande, Jean Manca, Wouter Maes, Sabine Van Doorslaer, and Etienne Goovaerts. Charge transfer in the weak driving force limit in blends of MDMO-PPV and dithienylthiazolo[5,4-d]thiazoles towards organic photovoltaics with high v_{OC}. *Physical Chemistry Chemical Physics*, 2012.

[12] Christopher M. Proctor, Martijn Kuik, and Thuc-Quyen Nguyen. Charge carrier recombination in organic solar cells. *Progress in Polymer Science*, 2013.

[13] REN21. Renewables 2014 - global status raport. 2014.

[14] M.C. Scharber and N.S. Sariciftci. Efficiency of bulk-heterojunction organic solar cells. *Progress in Polymer Science*, 2013.

[15] Wiebe Wagemans. *Plastic Spintronics: Spin transport and intrinsic magnetoresistance in organic semiconductors*. PhD thesis, Technische Universiteit Eindhoven, 2010.

[16] www.sigmaaldrich.com.

[17] Naichia Yeh and Pulin Yeh. Organic solar cells: Their developments and potentials. *Renewable and Sustainable Energy Reviews*, 2013.

[18] Biniam Zerai Tedlla, Feng Zhu, Matthijs Cox, Jeroen Drijkoningen, Jean Manca, Bert Koopmans, and Etienne Goovaerts. Understanding triplet formation pathways in bulk heterojunction polymer:fullerene photovoltaic devices. *Advanced Energy Materials*, 2014.